

Phase-Field Modelling of Welding and of Elasticity-Dependent Phase Transformations

Zur Erlangung des akademischen Grades eines
Doktors der Ingenieurwissenschaften
(Dr.-Ing.)

bei der Fakultät für Maschinenbau
des Karlsruher Instituts für Technologie (KIT)
am Institute of Applied Materials –
Computational Materials Science (IAM-CMS)

genehmigte DISSERTATION

von

Dipl.-Math. Oleg Tschukin

Datum der mündlichen Prüfung: 4. Mai 2017
Referent: Prof. Dr. rer. nat. Britta Nestler
Korreferent: Prof. Dr. Anton Möslang

to Maria Baranowski, née Aman

Credits

I would like to thank my family, and especially my parents and my wife, for their unbiased faith in all my endeavours and for their constant support in all respects. I thank Prof. Dr. rer. nat. Britta Nestler for the motivation to complete a PhD and also for her continuous scientific and personal support during the time. Special thanks goes to Prof. Dr. Anton Möslang who willingly offered to be a second adviser of my thesis. Last but not least, I would like to mention my fellows who helped me here and there and with whom I mostly had lively, but fruitful discussions.

Abstract (English Version)

A phase-field model for the simulation of solidification and grain growth during an electron beam welding process is presented. With the simplifying assumptions, the macroscopic temperature field inside the welding sample is assumed to be quasi-stationary. Moreover, the principle of superposition is applied to derive the macroscopic temperature distribution. To use the temperature field as input in the simulations of the grain evolution, the analytical expression of the macroscopic temperature field, which is given as an indefinite integral, is approximated with a closed-form approach. The extension of the phase-field model, which incorporates the nucleation model, is applied to reconstitute the results of different solidification scenarios. Furthermore, the usage of temperature-dependent grain boundary mobility allows to simulate grain coarsening in the weld as well as in the heat-affected zone. The qualitative adjustment between the numerical, theoretical and real grain structures is presented.

The quantitative incorporation of the elastic effects into the phase-field model is the main focus of this thesis. This is of interest in the applications, in which the elastic fields function as a configurational driving force for phase transformations or as an underlying field to model consequential processes like plasticity and other processes. The theory of the phase-field elasticity model is based on the mechanical jump conditions at a coherent interface of two solid phases, and a short overview of the current approaches and of our recent work [1], in particular, is given to discuss the inconsistency of the models. A novel model is presented, which is based on the similar concept but is written using an alternative formalism. With the homogeneous interfacial variables, the strain energy is interpolated in a thermodynamically consistent manner and is reformulated in terms of the original thermodynamical and mechanical system variables. Consequently, the required quantities, such as the Cauchy stress tensor and the elastic configurational force, both are given in accordance with the variational principle. Furthermore, all elastic fields are explicitly given in the Voigt notation because it is used in the in-situ solver PACE3D for the implementation of the model. By assuming the solid phases to be elastically isotropic, further mathematical simplifications are presented; they are indispensable for an efficient computational performance. Finally, an extension of the model for multiphase systems is demonstrated.

The newly formulated model is verified by using known analytical solutions for two-phase systems in mechanical and thermodynamic equilibrium. Doing so, the phase-field elasticity model is extended by a simple chemical model, and the equilibrium conditions are explicitly formulated. The Eshelby inclusion in an infinite surrounding matrix is an ideal setup to perform validating simulation scenarios with a clear and manageable computational effort. For nine different test cases, simulations with varying model parameters are performed in order to assess the sustainability of the presented models. The simulation results, which are based on the newly presented phase-field model for elastically inhomogeneous systems, coincide with the theoretical predictions, in contrast to the simulation results which are based on our recent model in [1].

- [1] D. Schneider, O. Tschukin, A. Choudhury, M. Selzer, T. Böhlke, B. Nestler. Phase-field elasticity model based on mechanical jump conditions. *Computational Mechanics*, 55(5):887–901, 2015.

Abstract (German Version)

Ein Phasenfeldmodell zur Simulation des Kornwachstums, während eines Elektronenstrahlschweißvorgangs, wird präsentiert. Dazu wird das makroskopische Temperaturfeld in der Schweißprobe mit den vereinfachenden Annahmen als quasi-stationär vorausgesetzt und unter der Anwendung des Superpositionsprinzips analytisch bestimmt. Der analytische Ausdruck wird mit einer Funktion in geschlossener Form approximiert, um in der Simulation des Kornwachstums als Eingabe zu fungieren. Bei der Benutzung einer temperaturabhängigen Korngrenzenmobilität in der Simulation sind die Vergrößerungsprozesse in der Schweißnaht sowie in der Wärmeeinflusszone wiedergegeben. Bei der Erweiterung des Phasenfeldmodells um eine Nukleationsmethode werden unterschiedliche Muster der Kornmorphologie qualitativ abgebildet.

Der Hauptfokus dieser Arbeit liegt jedoch auf der quantitativen Modellierung der Phasenübergänge, bei denen elastische Verformung eine führende oder eine grundsätzliche Rolle spielt, zum Beispiel zur weiteren Beschreibung des elastoplastischen Verhaltens. Die Theorie zur Herleitung der relevanten elastischen Felder basiert auf den mechanischen Sprungbedingungen, die an einer kohärenten Korngrenze im Gleichgewicht gelten. Es wird kurz auf die existierenden Modelle und besonders auf unsere Methode aus [1] eingegangen und die Schwächen der Modelle diskutiert. Zur Herleitung eines quantitativen Phasenfeldmodells, das die verbleibenden Defekte beseitigt, wird ein neuer Formalismus vorgestellt. Mit den homogenen Variablen innerhalb des diffusen Übergangsbereichs werden die elastischen Energien zweier benachbarter Phasen thermodynamisch konsistent interpoliert. Die resultierende Verformungsenergie wird in Abhängigkeit von den Systemgrößen hergeleitet, sodass die Cauchy'sche Spannung sowie die Konfigurationskraft unter der Anwendung des Variationsprinzips formuliert werden. Für die numerische Implementierung des Modells wird die Voigt'sche Notation der Dehnung und der Cauchy'schen Spannung benutzt. Folglich werden alle relevanten Felder explizit für diese Schreibweise angegeben. Für elastisch isotrope Phasen ergeben sich weitere signifikante rechnerische Vereinfachungen, die für eine effiziente numerische Umsetzung unabdingbar sind. Schließlich wird eine Erweiterung des Zwei-Phasen-Modells für Multi-Phasen präsentiert.

Das formulierte Modell wird detailliert im Abgleich mit der analytischen Lösung

für das mechanische und thermodynamische Gleichgewicht verifiziert. Hierzu wird das Phasenfeldmodell um das chemische System erweitert und die Bedingungen für einen Gleichgewichtszustand explizit angegeben. Der elastische Eshelby-Einschluss in einer umgebenden elastischen Matrix ist ein ideales Referenzsystem, für welches unterschiedliche Simulationsszenarien mit einem überschaubaren rechnerischen Aufwand umgesetzt werden können. Für neun unterschiedliche Testfälle werden Simulationen mit variierenden Modellparametern durchgeführt und anhand der Simulationsergebnisse werden die Modelle beurteilt. Im Unterschied zu den Ergebnissen für das vorhergehende Modell aus [1] koinzidieren die Simulationsergebnisse für das in dieser Arbeit präsentierte Phasenfeldmodell mit den theoretischen Vorgaben.

- [1] D. Schneider, O. Tschukin, A. Choudhury, M. Selzer, T. Böhlke, B. Nestler. Phase-field elasticity model based on mechanical jump conditions. *Computational Mechanics*, 55(5):887–901, 2015.

Contents

1. Motivation and Synopsis	1
2. Introduction	7
2.1. Phase-Field Modelling	7
2.1.1. Simple phase-field models for phase transition	11
2.1.2. Isothermal pure component solidification	12
2.1.3. Binary alloy in thermodynamic equilibrium	13
2.2. Numerical implementation	16
2.2.1. Computational optimisation tools	19
3. Grain Structure Evolution during Electron Beam Welding	21
3.1. Problem statement	23
3.2. Macroscopic temperature field	25
3.2.1. Heat conduction evolution equation	25
3.2.2. Model for the heat source	26
3.2.3. Analytical and closed-form solutions	28
3.3. Phase-field model for grain evolution	31
3.3.1. Evolution equations	32
3.3.2. Dimensioning of the simulation domain	33
3.3.3. Initial filling	34
3.3.4. Parameters for interfacial energy	34
3.3.5. Bulk energies	34
3.3.6. Kinetic coefficients	35
3.3.7. Model for nucleation	41
3.3.8. Simulation results	44
3.4. Conclusion	48
4. Phase-Field Models with Elasticity	51
4.1. Introduction	51
4.2. Mechanical jump conditions at a coherent interface	54
4.3. Short overview over the model by Schneider et al.	55
4.3.1. The concept of the model	55
4.3.2. Coordinate transformation	55
4.3.3. Inhomogeneous variables	57
4.3.4. Elastic energy in the diffuse interface	57

Contents

4.3.5.	Cauchy stress in the diffuse interface	58
4.3.6.	Elastic driving force for solid-solid phase transformation .	59
4.3.7.	Some drawbacks of the model by Schneider et al.	60
4.4.	A new formulation of the elastic energy and the consequential fields	61
4.4.1.	Decomposition of the stress and strain tensors into the homogeneous and inhomogeneous constituents	61
4.4.2.	Phase-dependent elastic energy	64
4.4.3.	Elastic energy in the diffuse interface	66
4.4.4.	Calculation of the stress tensor	70
4.4.5.	Elastic driving force	71
4.4.6.	A short summary of the main equations	75
4.5.	Explicit formulation of the elastic fields in the Voigt notation . .	76
4.5.1.	Simplifications for the elastic isotropic materials	84
4.6.	Extension of the model to multiphases	88
5.	Validation of the presented phase-field elasticity models	93
5.1.	Introduction	93
5.2.	Extension of the model by the chemical part	94
5.2.1.	Evolution equations	96
5.2.2.	Thermodynamical and mechanical equilibrium	97
5.3.	Eshelby inclusion	98
5.3.1.	Elastic constants versus geometrical form	100
5.3.2.	Elliptical inhomogeneity and the equivalent inclusion method	101
5.4.	Preparation of the simulations	102
5.4.1.	Parameter and conditions for the elastic model	102
5.4.2.	Functions for the chemical model	104
5.4.3.	Matching between capillary, elastic and chemical systems	105
5.4.4.	Definition of tested scenarios	107
5.5.	Simulation results and discussion	109
5.6.	Conclusion	120
6.	Conclusion of the thesis	123
7.	Outlook	125
7.1.	Phase-field model of welding	125
7.2.	Phase-field model of elasticity-dependent phase transformations .	126
	Appendix	129
A.	Quantitative interpolation functions	131
B.	Required tensors for the Eshelby inclusion	133

C. Computational efficiency of the presented models	135
--	------------

List of Figures

2.1. Schematic representation of the sharp and diffuse interfaces between the different phases.	9
2.2. Qualitative representation of the influence of the relevant terms in the phase-field evolution equation.	12
2.3. Schematic presentation of the concentration profiles for sharp and diffuse interface between the solid and liquid phases.	14
2.4. Illustration of the excess energy as a consequence of inconsistent free energy interpolation through the diffuse interface.	15
2.5. Two-dimensional discrete stencil for the schematic description of the discrete evaluation of the scalar and vectorial fields.	17
3.1. Electron beam welding – the main working principles. [1]	22
3.2. EBSD image for a view from above on the horizontal plane of the welded seam of two ferritic steel samples. The welding direction is from bottom to top. The weld was done at KIT, IAM-AMP by V. Widak, M. Rieth.	23
3.3. Global and moving coordinate systems for welding heat conduction [2].	25
3.4. Contour lines of normalised power density distribution $\frac{p(\chi, \xi, \zeta)}{2\eta P A^2 / h\pi R^2}$ on different depths: $\zeta' = 0$, $\zeta' = 0.25h$, $\zeta' = 0.5h$, $\zeta' = 0.75h$	27
3.5. Isotherms at different depths, $z = 0$ mm on the top, $z = 1$ mm in the middle and $z = 4$ mm on the bottom. Solid and dashed lines correspond to the numerical evaluation of the analytical solution $T^{ana}(w, y, z = const)$ in eq. (3.4) and to the approximation $T^{app}(w, y)$ in eq. (3.5), respectively.	30
3.6. Simulation results of a temporal sequence with a time step of 0.5 s for the solid-solid kinetic coefficient, $\tau_{\alpha\beta}^{test1}$. The changing mesh corresponds to the grain boundary motion, and the coloured field is the temperature field which moves through the simulation domain.	36

List of Figures

3.7. Simulation results of a temporal sequence with a time step of 0.5 s for the solid-solid kinetic coefficient, $\tau_{\alpha\beta}^{test2}$. The changing mesh corresponds to the grain boundary motion, and the coloured field is the temperature field which moves through the simulation domain.	37
3.8. Arrhenius plot for the chosen mobility in eq. (3.15)	38
3.9. A sequence of the grain structure evolution for the temperature-dependent solid-solid kinetic coefficient. The figures correspond to the time steps 0, 0.5 and 1 s, respectively.	39
3.10. A zoomed area in the heat-affected zone for different time steps.	40
3.11. Schematic diagram of the described nucleation algorithm.	43
3.12. The coloured field corresponds to the liquid distribution. The mesh signs the grain boundaries. The nucleation model parameters are: $\xi = 0.4$, $\bar{A} = 0.7$	45
3.13. The coloured field corresponds to the liquid distribution. The mesh signs the grain boundaries. The nucleation model parameters are: $\xi = 0.4$, $\bar{A} = 0.3$	45
3.14. Coloured domains represent different grains. The nucleation model parameters are: $P=8\%$, $\bar{A} = 0.3$	46
3.15. The nucleation model parameters are: $P=9\%$, $\xi = 0.4$, $\bar{A} = 0.3$. The isotherms of the moving temperature field are represented by the coloured areas. The mesh signs the grain structure.	47
3.16. Visualisation of the recrystallisation process in the post solidified weld seam in a temporal sequence of a simulation with the nucleation model parameters: $P=20\%$, $\xi = 0.35$, $\bar{A} = 0.3$	47
3.17. Comparison between theoretical imagination from the existing text book theories [3, 4] on the left and simulation results on the right.	48
5.1. Elliptical inclusion in the matrix and the simulation setup	99
5.2. Analytical and approximated distribution of stress components along the vertical domain boundaries.	103
5.3. Analytical and approximated distribution of stress components along the vertical domain boundaries.	103
5.4. The distribution of the capillary, the elastic and the chemical driving forces along the elliptical interface for the inclusion at the thermodynamic equilibrium eq. (5.11).	105
5.5. Grand chemical potentials for the inlay ω^I and for the matrix ω^M , in dependence on the chemical potential μ	106
5.6. Resulting shapes for the 1. scenario: $\nu^{Inh} = 0.1$ $E^{Inh} = 1050$	110
5.7. Resulting shapes for the 2. scenario: $\nu^{Inh} = 0.1$ $E^{Inh} = 2100$	111
5.8. Resulting shapes for the 3. scenario: $\nu^{Inh} = 0.1$ $E^{Inh} = 3150$	111
5.9. Resulting shapes for the 4. scenario: $\nu^{Inh} = 0.25$ $E^{Inh} = 1050$	112

5.10. Resulting shapes for the 5. scenario: $\nu^{Inh} = 0.25$ $E^{Inh} = 2100$. . 113

5.11. Resulting shapes for the 6. scenario: $\nu^{Inh} = 0.25$ $E^{Inh} = 3150$. . 113

5.12. Resulting shapes for the 7. scenario: $\nu^{Inh} = 0.3$ $E^{Inh} = 1050$. . 114

5.13. Resulting shapes for the 8. scenario: $\nu^{Inh} = 0.3$ $E^{Inh} = 2100$. . 115

5.14. Resulting shapes for the 9. scenario: $\nu^{Inh} = 0.3$ $E^{Inh} = 3150$. . 115

5.15. Orthogonal normal stresses, along the x -axes on the left and y -axes on the right, for the third test scenario, Table 5.1, σ_{xx} at the top, σ_{yy} in the middle and σ_{zz} at the bottom. Black, green and red lines correspond to the analytical and to numerical solutions with the characteristic lengths of $W\kappa = 0.5$ and $W\kappa = 0.75$, respectively. Grey areas sign the corresponding diffuse interface. 118

5.16. Orthogonal normal stresses, along the x -axes on the left and y -axes on the right, for the seventh test scenario, Table 5.1, σ_{xx} at the top, σ_{yy} in the middle and σ_{zz} at the bottom. Black, green and red lines correspond to the analytical and to numerical solutions with the characteristic lengths of $W\kappa = 0.5$ and $W\kappa = 0.75$, respectively. Grey areas sign the corresponding diffuse interface. 119

5.17. Relative deviation from the analytical value of the orthogonal normal stresses and the shear stress in the inhomogeneity for the seventh scenario and for the characteristic length $W\kappa = 0.75$. . 120

7.1. Shape evolution of the unstable precipitate with the Young modulus ten times smaller than the Young modulus in the matrix. Solid lines correspond to the phase-field isolines $\phi = 0.01, 0.5, 0.99$. The density plots on the left side and on the right side of every image represent the chemical potential and the von Mises stress distribution, respectively. 127

7.2. A rod perturbed with harmonic disturbance. 127

C.1. Simulation setup for the comparison of the calculation times for both presented models, model by Schneider et al. and a newly presented approach. The screenshot shows the visualisation of the tool `xsimview` in `PACE3D`. 135

List of Tables

3.1. Parameters for the numerical evaluation of the temperature distribution due to the analytical solution eq. (3.4).	28
3.2. Parameters for the approximated temperature distribution. The approximation procedure was done by using WolframMathematica8.	29
5.1. Parameters for the investigated simulation setups.	108
5.2. Final constant chemical potential for the chosen simulation scenarios and in dependence on the diffuse interface width.	117
C.1. Different simulation scenarios with activated and deactivated optimisation options and with same or different elastic constants in the appropriate phases.	137
C.2. Simulation time in seconds of the numerical integration of the wave equation, eq. (C.1) on one processor, with 10000 iterations and 12 frames.	138

1. Motivation and Synopsis

G. P. Thomson¹² said, "We have labelled civilizations by the main materials which they have used: The Stone Age, the Bronze Age and the Iron Age ... a civilization is both developed and limited by the materials at its disposal ..." [5]. In the last century, man has encountered the limits of the materials that occur in nature and are producible with standard manufacturing processes [6]. With specific and cooperative requirements of the modern technologies, newly used materials should be more durable, more resilient, with better resistance to external influences, etc. than their predecessors, but most crucially "with properties that can be predicted, varied, and controlled" [5]. But on the other hand, there are also economical and environmental requirements, which limit the production processes. Thus, the attention of all relevant aspects during the design of new materials is the main challenge for the material scientists of today.

A targeted production of a workpiece with desired properties not only requires years of experience in the manufacturing practice, but also the knowledge about and the real understanding of the relevant natural processes taking place within the workpiece during the technological mode. Since the former mostly results in the empirical observations of the relations between the productive engineering practices and the workpiece properties, the latter tries to explain those correlations by formulating the hypotheses, empirical laws and theories, finally joining the science [7]. Referring again to Sir G. P. Thomson, he says in [8]: "science without technology is incomplete and inconclusive, and accentuates two aspects of science as "already valued for what it can do to increase man's control over nature, and feared for what some of its consequences may be", but "there is a second aspect. It is this: Science aims at understanding the nature of things. ... Its two aspects must be held in equal honour."

However, what was still impossible sixty years ago, nowadays is made possible by the exploitation of high-performance computers, which offer many new capabilities to unite both mentioned aspects in a novel quality. For instance, the

¹In this thesis, the famous scientists are honoured with a footnote, containing some interesting information about them, which can be found on the World Wide Web (www.wikipedia.org) in most cases.

²Sir George Paget Thomson, 03.05.1892 – 10.09.1975. English physicist, Nobel laureate in physics, 1937.

1. Motivation and Synopsis

real manufacturing processes can be reproduced in the simulations, according to the scope of interest. And presently, the usage of computer-aided programmes is indispensable in material sciences and engineering, see for example [9] and citations therein. Therefore, the gained understanding of real physical processes in the materials serves as the basis for virtual experiments, which simulate the natural sequences. But note that since the real processes are subject to natural laws, the simulated processes are based on the human understanding of these natural laws.

Though, the theoretical model alone is sometimes so complex and impractical for the virtual experiments, that one is basically forced to reinterpret the original theory in context of its computational applicability [9]. A fine example of such a procedure is a *phase-field model*, which is also known under the name of *diffuse interface approach*, and which basically roots in statistical physics [10]. This method currently finds a broad spectrum of applications, stretching from original microstructure evolution [11, 12, 13, 14, 15] across geological vein growth [16] and topology optimisation problems [17] to the medical [18] and biological topics [19].

But by focusing on the original subject area of the phase-field model, the microstructure evolution, this method can resolve the processes at different length scales, whereby it bases on the principles of equilibrium thermodynamics for irreversible processes [20]. However, the morphology changes in the workpiece, for the most manufacturing steps, run under non-equilibrated conditions with a lot of differently coupled material processes, such as heat and mass diffusion, phase transformations, elastic and plastic deformations and others. Therefore, there is a significant mismatch between the fundamental assumptions of the theoretical and computational approach, on the one hand, and the real natural processes, on other hand. But, nevertheless, the mathematical and computer-based tools, in form of temporo-spatial differential equations, and the corresponding computational model, respectively, can also be applied on the resembling processes in equilibrated and non-equilibrated systems.

For the physical systems, in which the basic assumptions for the corresponding computational model are supposed to be fulfilled, the computer simulation should quantitatively resolve the theoretical or experimental prediction, unless the model is inconsistent, and should be rethought. Therefore, with a quantitative computational model, and with the consequential virtual experiments, precise statements about the real processes inside the workpiece, during the manufacturing process, are beneficial, in order to predict, to vary and to control the required material properties. But also the applicability of the phase-field model, other than intended, but also for non-equilibrated manufacturing steps, allows to determine the essential and/or negligible phenomena, and to estimate

the tendencies of the material feedback for varying process parameters. Furthermore, a qualitative mathematical and computational model forms a base for the quantification, and an agreement between both the real and simulated results confirms the understanding of the relevant and dominant processes and the correspondence of the former.

In this thesis, I present both mentioned approaches. Thus, a qualitative phase-field model of grain structure evolution, during an electron beam welding process, as well as the quantitative phase-field model coupled to elastic phenomena are presented in this work.

Electron (laser) beam welding is an example of such a manufacturing process [3], which takes place under extreme conditions [21] and with a lot of differently coupled material processes, and can only be reproduced with considerable physical, mathematical, programming and computational efforts. Therefore, it is computationally very difficult to reproduce all running processes as a whole. This is why the simplifying assumptions are indispensable to facilitate the mathematical and computational model. Because the main focus in this topic is the simulation of the grain structure evolution in the weld and in the heat-affected zone, which is mainly driven by the temperature-dependent driving force, other physical phenomena, such as the melt flow [22] or keyhole instabilities [23], are neglected in this work. Furthermore, the thermal diffusion in the weld sample is decoupled from the melting and solidification processes, by the assumption of equal thermal constants in the solid and melt and by neglecting the latent heat contribution. In order to use the moving temperature field inside the welding sample as simulation input, it is assumed to be quasi-stationary, and for a well-established qualitative model for the power source term [24], it is derived in an analytical form, which is approximated to a closed-form solution.

From a mathematical point of view, the solidification and also the growth of each individual grain in the solid phase both are time-dependent free boundary problems. Since the former is driven by the temperature-dependent driving force, the latter roots in the surface energy minimisation. In order to resolve both kinetic processes with a diffuse interface approach, the mobilities of the corresponding interfaces are used in the magnitude that the kinetic undercooling of the solid-liquid interface consists of approximately ten Kelvin³ and the temperature-dependent mobility of the grain boundary recapitulates the grain coarsening. Finally, a multiphase-field model, extended with a nucleation model, is used for the grain growth and grain genesis in the weld and also to describe coarsening in the heat-affected zone. Note that the used phase-field equations are postulated ad hoc, but in similarity to the equilibrium thermodynamics.

³William Thomson, 1st Baron Kelvin, 26.06.1824 – 17.12.1907. Scots-Irish mathematical physicist and engineer. He formulated the first and second laws of thermodynamics. His title died with him.

1. Motivation and Synopsis

The qualitative simulation results of the grain structure in and around the weld warrant the applicability of the presented approach and form a solid base for a further extension and quantification of the model.

As mentioned, the main part of this work is the formulation of a quantitative phase-field model for solid-solid phase transformation, which is driven by the elastic forces. This coupled process is also of interest, in which the elasticity is an underlying topic for consequential phenomena like plasticity and others. There are several existing works about the incorporation of the elastic force into the phase-field equation [25, 26, 27, 28, 29] as a transitional driving force, and in our recent work [30], we analysed current models and presented an alternative auspicious model. The sketchy overview of the relevant models is given in this thesis in order to highlight the remaining drawbacks. Based on the mechanical jump conditions at the coherent interface of two neighbouring solid phases, a novel approach is presented. A derived formulation of the elastic driving force and of the stress is thermodynamically consistent as well as in total correspondence with the variational principle. While the derivations are mathematically sophisticated, the derived final results are given in a mathematically elegant and short form, which also bears in efficient implementation. By the assumption of the elastically isotropic materials, further simplifications in the mathematical expressions and in consequential programming can be done. Moreover, an extension of the original two-phase model for a multiphase system is presented.

In order to verify the presented model, a two-dimensional setup with all known quantities is applied. Eshelby's elliptical inclusion, which is embedded in an elastic matrix, is ideal to test several scenarios and to validate a model in more detail. For a strict validation, the elasticity phase-field model is extended by a simple chemical model, and the conditions for the thermodynamical and mechanical equilibrium are explicitly given. The parameters for the simulations and the boundary conditions at the finite simulation domains are prepared accurately, with respect to the analytical prediction, in order to minimise undesired effects. For nine different testing scenarios, the simulation results for our recent model [30] and for a newly derived model are presented in dependence on model parameters in order to appraise the verifiability of the presented models.

This work consists of the following parts. In chapter 2, a rudimentary introduction of phase-field modelling is presented together with a short overview over the used discretization scheme. In chapter 3, a multiphase-field model, extended with a nucleation approach, is formulated to simulate the grain structure evolution in the welded joint and in the heat-affected zone, during electron beam welding. The corresponding simulation results are presented, and the potential extensions of the model are discussed. Chapter 4 deals with the phase-field models, which also contain elastic effects. Our recent model from [30] is presented to highlight its defects, and a necessity of the novel formalism. Thus a renewed

derivation of the model, its reformulation in the Voigt⁴ notation and its derived simplifications are the main content of this chapter. In chapter 5, the accurate and strict verification of the newly presented model is demonstrated. The conclusion of the main results of this work is found in chapter 6, and an outlook of this work is presented in chapter 7.

⁴Woldemar Voigt, 02.09.1850 - 13.12.1919, German physicist. The term "tensor" was first used by him.

2. Introduction

For a better understanding, and to get an idea about the concept of the phase-field modelling, a short overview is given in this chapter. The applied numerical scheme for the discrete evaluation of the evolution equations is given. The interested reader is referred to the theoretical books, which deal with phase-field modelling [25, 31, 32], dynamical systems [33], optimisation problems [34] and computational solving of ordinary and partial differential equations [35], whereby the recommended literature list in this chapter, and in this thesis as a whole, is only a drop in the ocean of the noteworthy works.

2.1. Phase-Field Modelling

The presence, the location and the temporal evolution of the interfaces in the morphology of metallic, ceramic or plastic materials significantly influence their mechanical, thermal and other engineering properties. Herein, the term "interface" implies a border between two (or multiple) subdomains, which differ in at least one feature (property), hereafter referred to as phases. Thus, there are a lot of different physical problems, e.g. pure component or alloy solidifications, sintering, solid-solid phase transformation, coarsening, crack propagation, etc., in which the interfaces play a crucial role. Based on the mentioned processes, the interface can be the boundary between a crystal and its melt, the common border between two identical, but misoriented grains, the interface of two immiscible liquids, the common surface between the parental austenite and martensite, the fracture surface, etc. Note that the crack is not a phase in the classical sense, but with respect to the previous definition.

Since the nature of the neighbouring phases is ambiguous, the border in between also has various types. Typically, the location and motion of such interfaces is coupled to the material processes taking place in the working sample and also to processing conditions.

In spite of the different physical problems, but because of the interface motion in the mentioned system, the considered physical system is a *dynamic system* and also follows the main principles of the *stability theory of the dynamical*

2. Introduction

systems, also known as theory of Lyapunov¹. Moreover, the temporo-spatial evolution of the interface is based on the optimisation principle, whereby the general objective quantity is known as Lyapunov function/functional.

Thus, the basic idea behind the derivation of the phase-field method is the formulation of an optimised Lyapunov functional, which is either constant over time (bundle of the first integrals, such as total energy, total momentum and total angular momentum) or converges monotonically into its extremum (increasing entropy or decreasing free energy in an isolated system).

Basically, the considered optimised quantity in a multiphase system is given in an integral form by a sum of all (here N) bulk and all interfacial contributions

$$\mathcal{E}(\mathbf{s}) = \sum_{\alpha=1}^N \int_{V_{\alpha}} e(\mathbf{s}) dV + \sum_{\alpha < \beta}^N \int_{\Gamma_{\alpha\beta}} \tilde{\sigma}_{\alpha\beta}(\mathbf{s}, \mathbf{n}_{\alpha\beta}) d\mathbf{n},$$

whereby all external and production terms are neglected. Herein, e is the volumetric density and $\tilde{\sigma}_{\alpha\beta}$ is the surface density of total \mathcal{E} . Both depend on the state variables \mathbf{s} , which are intensive or extensive thermodynamic quantities, such as temperature T , composition $\mathbf{c} = (c_1, \dots, c_K)$, chemical potential $\boldsymbol{\mu} = (\mu_1, \dots, \mu_K)$, deformation $\nabla \mathbf{u}$, etc. Different V_{α} 's mark different subvolumes of the corresponding phases, each of them with homogeneous material properties. $\Gamma_{\alpha\beta}$ is the common interface between V_{α} and V_{β} , see the left figure in Figure 2.1. The orientation of the interface $\Gamma_{\alpha\beta}$ is given by its normal $\mathbf{n}_{\alpha\beta}$. Additionally, the interfacial density $\tilde{\sigma}_{\alpha\beta}$ can also be anisotropic, $\tilde{\sigma}_{\alpha\beta}(\mathbf{s}, \mathbf{n}_{\alpha\beta})$.

In the time-dependent free boundary problems, the interface between the neighbouring phases evolves in time, in dependence on the surrounding conditions. Since the real physical width of the interface is some nanometres, there is a challenge to overcome the discrepancy in the length scales in the simultaneously coupled computational calculations of the macroscopic processes in the bulk phases and of the interface motion, also known as a sharp interface description. One of the solutions of this question is the usage of a diffuse interface method, which follows from an alternative formulation of the objective functional, which

¹Aleksandr Mikhailovich Lyapunov, 25.05.1857 - 03.11.1918, Russian mathematician, mechanician and physicist. In his revolutionary work [36], he developed the general *stability theory of a dynamical systems*. There are no natural sciences, which deal with time-dependent processes in the form of differential equations of system variables, where the stability theory does not play a crucial role.

is of *Ginzburg²-Landau³-type* [10],

$$\mathcal{E}(\phi, \nabla\phi, \mathbf{s}) = \int_V \epsilon a(\phi, \nabla\phi) + \frac{1}{\epsilon} w(\phi) + e(\phi, \mathbf{s}) dV. \quad (2.1)$$

The *Lyapunov functional of Ginzburg-Landau-type*, eq. (2.1), consists of three relevant parts. $\epsilon a(\phi, \nabla\phi)$ is the *gradient energy*, $\frac{1}{\epsilon} w(\phi)$ is the *potential* and the term $e(\phi, \nabla\phi, \mathbf{s})$ corresponds to the original volumetric densities. The specific terms $a(\phi, \nabla\phi)$ and $w(\phi)$ depend on the phase-field vector $\phi = (\phi_1, \phi_2, \dots, \phi_N)$ and its gradient, which is defined as $\nabla\phi = (\nabla\phi_1, \nabla\phi_2, \dots, \nabla\phi_N)$, with N constituents due to the number of total phases. Note that the phase-field functions sign the bulk phases and the interfaces, and that they are formulated with respect to the application and the corresponding physical setup, whereby they can be the composition, the phase volume fraction, the crystal orientation, the polarisation, etc. Thus, there is no "the" phase-field model, but an approach, according to a problem statement.

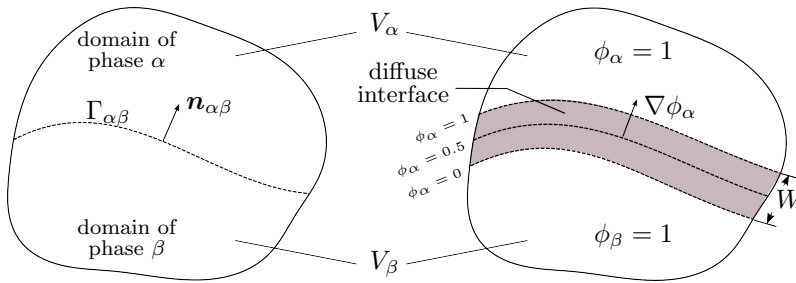


Figure 2.1.: Schematic representation of the sharp and diffuse interfaces between the different phases.

Nowadays, there are different formulations of the objective functional, eq. (2.1). Historically, the total free energy of the system [10, 37, 38, 39] was chosen as a minimised Helmholtz⁴ free energy. Since the second law of thermodynamics must be satisfied, some authors prefer to deal with the entropy functional [20, 40], whereby it is sometimes more convenient to operate with the Landau

²Vitaly Lazarevich Ginzburg, 21.09.1916 – 08.11.2009, Soviet and Russian physicist, Nobel laureate in Physics, 2003. Author of over 400 publications and about 10 monographs in theoretical physics, radioastronomy and cosmic ray physics.

³Lev Davidovich Landau, 09.01.1908 – 01.04.1968, Soviet physicist, Nobel laureate in Physics, 1962. He made fundamental contributions to many areas of theoretical physics and is one of the authors of the classical *Course of Theoretical Physics*.

⁴Hermann Ludwig Ferdinand von Helmholtz, 31.08.1821 – 08.09.1894). German physician and physicist. The Helmholtz Association, which is named after him, is the largest German association of research institutions.

2. Introduction

potential [41, 42]. Independent of the choice of the objective function \mathcal{E} , the terms $\epsilon a(\phi, \nabla\phi)$ and $\frac{1}{\epsilon}w(\phi)$ model the energetic/entropic level in the phase boundaries of the system. The gradient energy and the potential are defined in such a manner that the surface energy/entropy is resolved [40],

$$\int_{\Gamma_{\alpha\beta}} \tilde{\sigma}_{\alpha\beta}(\mathbf{s}, \mathbf{n}) d\mathbf{n} \approx \int_V \epsilon a(\phi, \nabla\phi, \mathbf{s}) + \frac{1}{\epsilon} w(\phi, \nabla\phi, \mathbf{s}) dV.$$

Thus, in order to overcome the mentioned conflict in the length scales of the interfacial and bulk physics, the original *sharp* interface is "stretched" to a *diffuse* interface of finite width, W , which is related to the model parameter ϵ and can be much higher than the real width of some angstroms, see Figure 2.1.

Moreover, the original bulk densities $e^\alpha(\mathbf{s})$, $\alpha = 1, \dots, N$ are interpolated throughout the diffuse interface with the interpolation functions $h_\alpha(\phi)$ to

$$e(\phi, \mathbf{s}) = \sum_{\alpha=1}^N e^\alpha(\mathbf{s}) h_\alpha(\phi),$$

with the monotonic smooth interpolation functions having the following properties:

$$h_\alpha(\phi_\alpha = 0) = 0 \quad \text{and} \quad h_\alpha(\phi_\alpha = 1) = 1,$$

and $\sum_\alpha h_\alpha(\phi) = 1$. Moreover, the choice of the correct interpolation quantities is indispensable for quantitative modelling, as was exemplarily shown in [43, 41, 42, 30] and is also presented in this work.

Assuming the linearity between the thermodynamical driving forces and the corresponding fluxes, the evolution equations of the system variables are based on the variational principle [20], whereby the variation, with respect to the variable a , is written as

$$\frac{\delta}{\delta a} = \frac{\partial}{\partial a} - \nabla \cdot \frac{\partial}{\partial(\nabla a)}. \quad (2.2)$$

Since the state variables can follow the conservation laws, such as the composition or internal energy, the corresponding evolution equation is known as Cahn⁵-Hilliard equation

$$\partial_t \phi_\alpha = \nabla \cdot \left(\mathbf{M}(\phi, \nabla\phi, \mathbf{s}) \nabla \frac{\delta \mathcal{E}(\phi, \nabla\phi, \mathbf{s})}{\delta \phi_\alpha} \right). \quad (2.3)$$

⁵John Werner Cahn, 09.01.1928 – 14.03.2016. American material scientist and chemophysicist.

In the case when the phase-field variable, such as the crystal orientation or the local volume fraction, is not conserved, the equation becomes an Allen-Cahn-type and is a reaction-diffusion equation

$$\epsilon \partial_t \phi_\alpha = \pm M(\phi, \nabla \phi, \mathbf{s}) \frac{\delta \mathcal{E}}{\delta \phi_\alpha} \quad (2.4)$$

with sign, due to the maximisation or minimisation process of the objective \mathcal{E} . In the presence of a constraint on the phase-field variables, in form of an equation $g(\phi, \nabla \phi) = 0$, for example a summation of all local volume fractions to one, the evolution equations modifies to

$$\epsilon \partial_t \phi_\alpha = \pm M \left(\frac{\partial \mathcal{E}}{\partial \phi_\alpha} - \nabla \cdot \frac{\partial \mathcal{E}}{\partial \nabla \phi_\alpha} - \Lambda \left(\frac{\partial g}{\partial \phi_\alpha} - \nabla \cdot \frac{\partial g}{\partial \nabla \phi_\alpha} \right) \right), \quad (2.5)$$

with Lagrange⁶ multiplier Λ .

The mobilities \mathbf{M} in eq. (2.3), and M in eq. (2.5), could depend on the system variables as well as on the phase-field and its gradient and represent the diffusion and a reaction rate. The interpolation type of the mobilities is also relevant for the quantitative modelling, as was exemplarily shown in [44, 45, 15].

2.1.1. Simple phase-field models for phase transition

The schematic representation, as to how the phase-field model modifies the physical system is shown in Figure 2.1. To avoid misunderstandings, I demonstrate simple phase-field models in the following, consisting of two transitional phases: phase α and phase β (or also solid and liquid phases). The permissible choice of the objective functional for isothermal systems is done by the minimising Helmholtz free energy [39]. The phases occupy the subvolumes V_α and V_β , respectively, see Figure 2.1. Two phase-field functions, $\phi_\alpha(\mathbf{x})$ and $\phi_\beta(\mathbf{x})$, are introduced locally to differentiate the volume fractions of the appropriate phases. With the following satisfying conditions $\phi_\alpha, \phi_\beta \in [0, 1]$, with $\phi_\alpha + \phi_\beta = 1$, only one phase-field parameter $\phi_\alpha = \phi$, ($\phi_\beta = 1 - \phi$) can be used for the formulations of the gradient energy and the potential with the constant model parameter $\gamma_{\alpha\beta}$, representing the interfacial energy exemplarily as

$$a(\phi, \nabla \phi) = \gamma_{\alpha\beta} |\nabla \phi|^2 \quad (2.6)$$

$$w(\phi) = \gamma_{\alpha\beta} \frac{16}{\pi^2} \phi(1 - \phi). \quad (2.7)$$

⁶Joseph-Louis Lagrange (Italian: Giuseppe Ludovico De la Grange Tournier), 25.01.1736 – 10.04.1813. He was an Italian mathematician and astronomer of the Enlightenment Era. He is a founder of analytical mechanics, and his name is one of the 72 names inscribed on the Eiffel Tower. The lunar crater Lagrange also bears his name.

2. Introduction

2.1.2. Isothermal pure component solidification

Considering the isothermal pure components solidification, the driving force is the difference of both interfacial Helmholtz free energies, ΔF . In the diffuse interface, the interpolation of constant, but different bulk free energy densities writes as

$$f(\phi) = f^\alpha h(\phi) + f^\beta (1 - h(\phi)). \quad (2.8)$$

By reducing the analysis to a one-dimensional case, the incorporation of eqs. (2.6)-(2.8) in eq. (2.4) results in

$$\partial_t \phi = M \left(\gamma_{\alpha\beta} 2 \partial_x^2 \phi - \gamma_{\alpha\beta} \frac{16}{\epsilon^2 \pi^2} (1 - 2\phi) - \frac{1}{\epsilon} (f^\alpha - f^\beta) h'(\phi) \right)$$

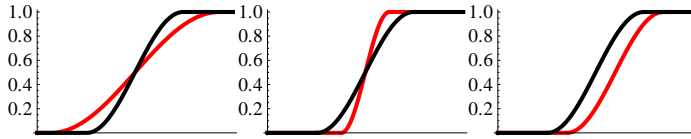


Figure 2.2.: Qualitative representation of the influence of the relevant terms in the phase-field evolution equation.

In Figure 2.2, every term in the phase-field evolution equation is explained by its effect on the original phase-field profile (all black lines). The first term corresponds to the variational derivative of the gradient energy, represents the diffusional behaviour of the evolution equation and "tends to stretch" the diffuse interface (red line, left). The second term is the derivative of the potential, and it antagonises the effect of the gradient energy by "sharpening" (red line, middle) the phase-field profile. In the right image in Figure 2.2, the effect of the third term is shown; the original phase-field profile (black line, right) moves with respect to the driving force (red line, right). Note that the integration of the driving force term in the phase-field equation and along the diffuse interface results in the original free energy jump ΔF .

Thermodynamic equilibrium

Since the system is in thermodynamic equilibrium, the driving force for the phase transformation vanishes, $f^\alpha - f^\beta = 0$, and the interface is stationary, $\partial_t \phi = 0$. Consequently, the phase-field equation reduces to

$$\gamma_{\alpha\beta} \partial_x^2 \phi = \gamma_{\alpha\beta} \frac{16}{2\pi^2 \epsilon^2} (1 - 2\phi).$$

Multiplying both sides with the phase-field gradient $\partial_x \phi$ and integrating results in

$$\epsilon \gamma_{\alpha\beta} (\partial_x \phi)^2 = \gamma_{\alpha\beta} \frac{16}{\pi^2 \epsilon} \phi(1 - \phi),$$

and it is nothing but the gradient energy eq. (2.6) and the potential eq. (2.7), the former scaled with the model parameter ϵ on left and the latter with its reciprocal on the right sides, respectively. The local balance of both energy terms is also known as *equipartition of energy* [46].

Furthermore, with standard techniques of finding the solution of the ordinary differential equations, the phase-field profile can be derived with the conditions $\phi(0) = 0.5$ and $\partial_x \phi > 0$ [47] to be

$$\phi(x) = \begin{cases} 0, & x < -0.125\pi^2\epsilon, \\ 0.5(1 + \sin(\frac{4}{\pi\epsilon}x)), & x \in [-0.125\pi^2\epsilon, 0.125\pi^2\epsilon], \\ 1, & x > 0.125\pi^2\epsilon \end{cases} \quad (2.9)$$

with the finite interface width being related to the modelling parameter ϵ by

$$W = \frac{\pi^2}{4}\epsilon \approx 2.5\epsilon. \quad (2.10)$$

The incorporation of the phase-field profile in the one-dimensional free energy integral, for an equilibrium, results in the equality

$$\tilde{\sigma}_{\alpha\beta} = \gamma_{\alpha\beta}, \quad (2.11)$$

between the real physical surface tension on the left-hand side and the corresponding model parameters for the interfacial energy on the right.

2.1.3. Binary alloy in thermodynamic equilibrium

The extension of the phase-field model for pure component solidification to the isothermal and non-isothermal alloy solidifications is a well studied and understood topic [38, 43, 41, 15], but there were also models with inaccurate formulations.

An obvious example of a thermodynamically inconsistent model can be demonstrated by considering the stationary interface between the solid and liquid phases of an alloy consisting of two components, A and B . By the assumption of constant molar volume, and due to the constraint $c^A + c^B = 1$, there is one independent concentration $c = c^A$. Since both phases are in thermodynamic equilibrium, the concentrations in the solid and liquid phases correspond to the

2. Introduction

values on the solidus and liquidus lines and are denoted with c_s and c_l , see Figure 2.3. Therefore, there is a jump in the concentrations at the sharp interface.

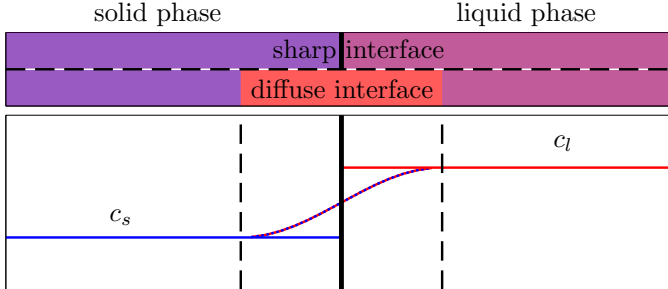


Figure 2.3.: Schematic presentation of the concentration profiles for sharp and diffuse interface between the solid and liquid phases.

In the phase-field approach, all quantities are straightened through the diffuse interface, and the concentration varies smoothly from solid to liquid concentration, see Figure 2.3. The question of the interpolation type of the corresponding free energies through the diffuse interface arises and the non-trivial answer has a widespread impact. The first approach was inspired by the interpolation of the Helmholtz free energies for pure components, eq. (2.8), and the extension to the binary systems straightforwardly became

$$f^{WBM}(c, \phi) = f_s(c)h(\phi_s) + f_l(c)h(\phi_l) \quad (2.12)$$

and is also known as a *WBM*-model [38]. Therefore, in the diffuse interface, the concentration is the homogeneous variable [38, 20, 48] and, moreover, the interface is understood as a mixture of both phases with the same composition.

Another interpolation type is derived using the conditions at thermodynamic equilibrium and assumes the homogeneity of the chemical potential, which is constant throughout the system, irrespective of sharp and diffuse interfaces, $\mu_s^{eq} = \mu_l^{eq}$. Furthermore, it corresponds to the slope of the common tangent of both free energies [43], see Figure 2.4. Consequently, the concentration in the diffuse interface is interpolated in accordance with its extensive thermodynamic nature as

$$c(\mu) = c_s(\mu)h(\phi_s) + c_l(\mu)h(\phi_l),$$

in dependence of the homogeneous chemical potential, and the free energy writes [43]

$$f^{KKS}(c, \phi) = f_s(c_s)h(\phi_s) + f_l(c_l)h(\phi_l) \quad (2.13)$$

Note that the concentrations in both interpolated free energies are different, $c_s \neq c_l$ in eq. (2.13), contrary to the same argument of the free energies in eq. (2.12). Moreover, in this approach, the diffuse area is understood as a mixture of both coexisting phases, each of them with its own extensive concentration due to the same intensive chemical potential.

The corresponding profiles of both interpolation types, eq. (2.12) and eq. (2.13), are shown in the free energy vs. concentration diagram in Figure 2.4, with black solid and green solid lines, respectively.

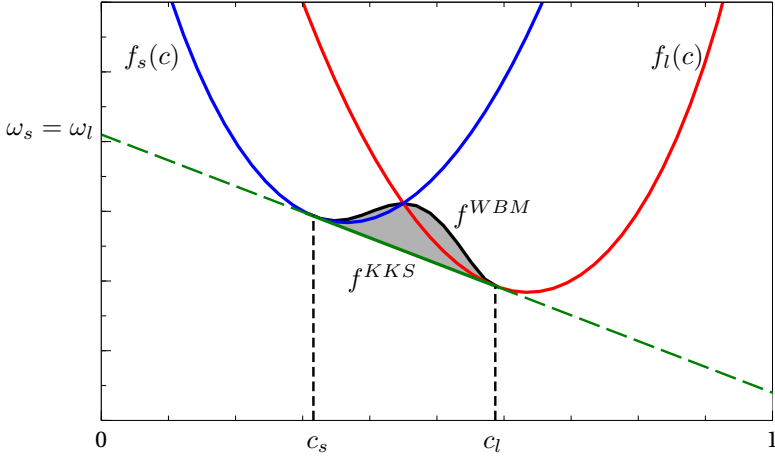


Figure 2.4.: Illustration of the excess energy as a consequence of inconsistent free energy interpolation through the diffuse interface.

Since the free energy f^{KKS} follows the common tangent profile, the free energy f^{WBM} connects both bulk values $f_s(c_s)$ and $f_l(c_l)$ through the common intersection point of $f_s(c)$ and $f_l(c)$. The grey area in Figure 2.4, between the interpolated free energy f^{WBM} and the common tangent, is an artificial energy contribution in the diffuse interface to the interfacial energy [47], which now writes as

$$\tilde{\sigma}_{\alpha\beta} = 2\gamma_{\alpha\beta} \int_0^1 \sqrt{\frac{16}{\pi^2} \phi(1-\phi) + \frac{\epsilon}{\gamma_{\alpha\beta}} \Delta\Psi(c, \phi)} d\phi, \quad (2.14)$$

2. Introduction

with $\Delta\Psi(c, \phi) = f^{WBM}(c, \phi) - f^{KKS}(c, \phi)$ as a difference between the inconsistent and consistent profiles. Hence, the equipartition of the energy in eq. (2.14) is not satisfied any more and is disturbed by the excess energy term $\frac{\epsilon}{\gamma_{\alpha\beta}} \Delta\Psi(c, \phi)$. Moreover, the diffuse interface width also depends on the excess energy contribution, and both modelling parameters ϵ and $\gamma_{\alpha\beta}$ could not be used independently from each other, but interlinked through the diffuse interface width W and the physical surface tension parameter $\tilde{\sigma}_{\alpha\beta}$ [42, 49]. Thus, while the excess energy is scaled by the model parameter ϵ , the desired interfacial energy $\tilde{\sigma}_{\alpha\beta}$ cannot be fixed by a straightforward manner as in eq. (2.11). Moreover, this is also the reason why the interface width is mostly chosen very thin, in order to decrease the contribution of the excess energy to the interfacial energy.

A similar approach of the reduction of the interface width is considered in models operating with elastic strains in the elastic inhomogeneous systems. However, the erroneous modelling roots in the usage of the homogeneous variables, which are thermodynamically inconsistent. This fundamental statement is also the starting point in chapter 4, in which the phase-field model is extended by the elastic effects in a thermodynamically consistent manner, i.e. by strictly following the differentiation between homogeneous and inhomogeneous variables.

2.2. Numerical implementation

The numerical implementation in the in-situ solver PACE3D (Parallel Algorithm for Crystal Evolution in 3D) consists of over 560000 lines of C code and is multifunctional. Within the solver, not only the phase-field equation can be solved, but, among other physical processes, it can be coupled to mass and heat diffusion, fluid flow, elastic and plastic effects, etc. The solver PACE3D is constantly being further developed and optimised in its implementation and performance.

As the name suggests, the simulations can be performed in three dimensions, but also in two and in one dimension. Regardless of the dimensions of the simulation domain, each present axis is divided into the equidistant intervals, with the physical widths of Δx , Δy , Δz , respectively. Consequently, if the simulation domain consists of the N_x , N_y , N_z intervals in the corresponding directions, the real measurement of the simulation domain is $N_x \Delta x \times N_y \Delta y \times N_z \Delta z$.

Every scalar field in the simulation domain is placed cell-centred and is signed by its indexes. Thus, for example, $\phi^{i,j,k}$ is the value at the position (X, Y, Z) , with $X = i\Delta x$, $Y = j\Delta y$ and $Z = k\Delta z$. In the following, I will use both notations for the phase field on the discrete grid $\phi(t, X, Y, Z)$ and $\phi^{i,j,k}$.

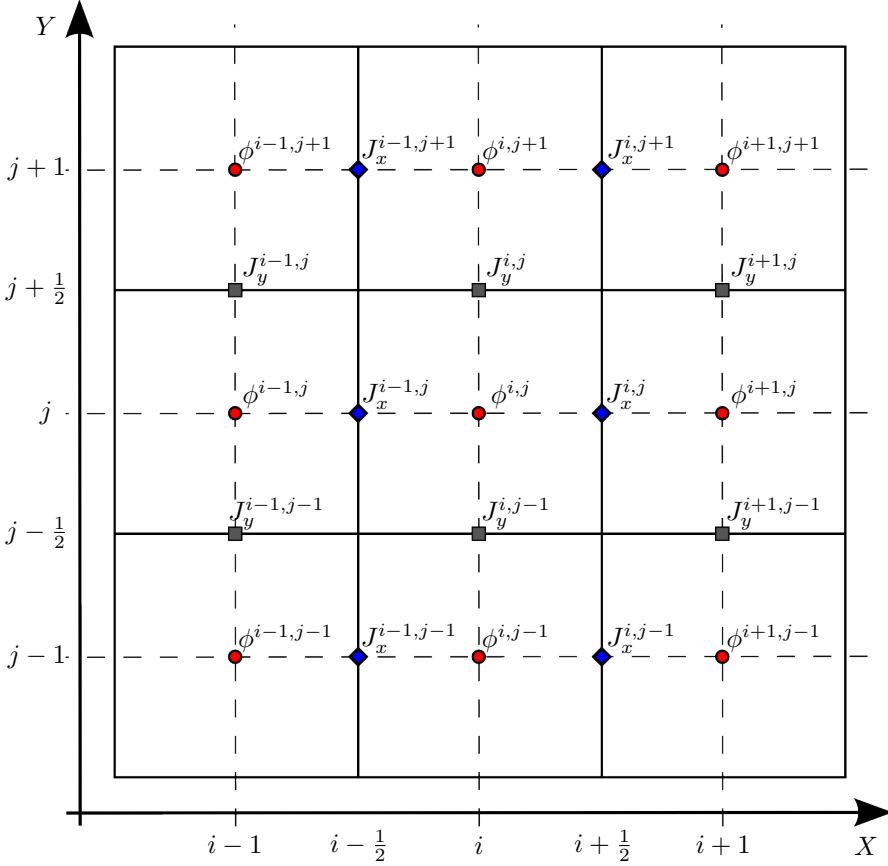


Figure 2.5.: Two-dimensional discrete stencil for the schematic description of the discrete evaluation of the scalar and vectorial fields.

The phase-field evolution equation, eq. (2.5), is a temporo-spatial partial differential equation and is discretized with an explicit forward Euler⁷ scheme for the temporal derivative

$$\partial_t \phi(t, x, y, z) \approx \frac{\phi(t + \Delta t, x, y, z) - \phi(t, x, y, z)}{\Delta t},$$

with Δt as a time step.

⁷Leonhard Euler, 15.04.1707 - 07.09.1783, Swiss mathematician, physicist, astronomer, logician and engineer. He is widely considered to be the most prolific mathematician of all time. Lunar crater Euler and asteroid 2002 Euler are named after him.

2. Introduction

In Figure 2.5, the spatial discretization scheme for the numerical evaluation of the right-hand side of equation (2.5) is shown. The discrete calculation uses a second-order accurate scheme, wherein the divergence of the vector field uses the backward finite differences and writes in two dimensions as

$$\nabla \cdot \mathbf{J}^{i,j} \approx \frac{J_x^{i,j} - J_x^{i-1,j}}{\Delta x} + \frac{J_y^{i,j} - J_y^{i,j-1}}{\Delta y}.$$

The evaluation of the flux components uses the forward finite difference scheme. Exemplary for the case in sec. 2.1.1, with constant parameter $\gamma_{\alpha\beta}$, the flux components write as

$$J_x^{i,j} \approx \gamma_{\alpha\beta} \frac{\phi^{i+1,j} - \phi^{i,j}}{\Delta x} \quad \text{and} \quad J_y^{i,j} \approx \gamma_{\alpha\beta} \frac{\phi^{i,j+1} - \phi^{i,j}}{\Delta y},$$

respectively, see Figure 2.5. The method is also known as *central difference scheme on staggered positions*.

Note that the flux components are placed on different positions of the cell. Since the flux can be written as

$$\mathbf{J}^{i,j} = J_x^{i,j} \mathbf{e}_x + J_y^{i,j} \mathbf{e}_y,$$

the coordinates correspond to the magnitudes of the flux in the directions due to the standard basis. Therefore, on the left and right edges of the cell, the fluxes through the edges are $J_x^{i-1,j} \mathbf{e}_x$ and $J_x^{i,j} \mathbf{e}_x$, respectively. Similarly, the fluxes in other directions, throughout the corresponding edges, are formulated.

Generally, the required flux vector components in eq. (2.5) are more complex in their determination and are written in the form of arithmetical operations of the spatial derivatives and phase-fields and their gradient-dependent functions. Therefore, the suitable quantities are averaged using the neighbouring values. Exemplarily, the phase-field value of the staggered position $(i + \frac{1}{2}, j)$ is given as

$$\phi^{i+\frac{1}{2},j} \approx \frac{1}{2} (\phi^{i,j} + \phi^{i+1,j})$$

or its gradient as

$$\nabla \phi^{i+\frac{1}{2},j} \approx \left(\begin{array}{c} \frac{\phi^{i+1,j} - \phi^{i,j}}{\Delta x} \\ \frac{(\phi^{i,j+1} + \phi^{i+1,j+1}) - (\phi^{i,j-1} + \phi^{i+1,j-1})}{4\Delta y} \end{array} \right),$$

etc. For more details, see, for example [17] and citations there.

2.2.1. Computational optimisation tools

For the systems with a large number ($N \gg 2$) of phase-field variables, there are different optimisation tools that are integrated in PACE3D. One of the applied tools is the *LROP* - *locally reduced order parameter* [50, 51], which controls the number of locally present phases, and thus facilitates a reduction in computation time and in memory consumption. Another tool is the *active phases* and was formulated intuitively and ad hoc [17]. The aim of the next section is to fill this gap.

Active phases

As the name indicates, the optimisation tool *active phases* only takes the locally present phases into account. But this procedure stands in contradiction to the original formulation of the Lagrange multiplier, which corresponds to the constraint

$$g(\phi) = \sum_{\alpha=1}^N \phi_{\alpha} - 1 = 0 \quad \Rightarrow \quad \partial_t g(\phi) = \sum_{\alpha=1}^N \partial_t \phi_{\alpha} = 0. \quad (2.15)$$

The incorporation of the previous constraint in the N phase-field equations of the form eq. (2.5) results in the system of equations

$$\tau \epsilon \partial_t \phi_{\alpha} = -\frac{\delta \mathcal{E}}{\delta \phi_{\alpha}} - \Lambda, \quad \forall \alpha \in \{1, \dots, N\}.$$

By the summation of all equations, the left side vanishes and the Lagrange multiplier results in

$$\Lambda_{old} = \frac{1}{N} \sum_{\alpha} \frac{\delta \mathcal{E}}{\delta \phi_{\alpha}} \neq 0, \quad (2.16)$$

and thus the resulting phase-field equations write as

$$\tau \epsilon \partial_t \phi_{\alpha} = -\frac{\delta \mathcal{E}}{\delta \phi_{\alpha}} - \frac{1}{N} \sum_{\alpha=1}^N \frac{\delta \mathcal{E}}{\delta \phi_{\alpha}}, \quad \forall \alpha \in \{1, \dots, N\}.$$

Therefore, for a phase which is not present in the simulation domain, the variation of the functional, with respect to this field variable, is assumed to be zero. But with a non-vanishing Lagrange multiplier, the temporal derivative does not vanish, and the corresponding phase-field evolves. This conflict was also analysed and discussed by the authors in [52], and a new multiphase-field model was suggested.

2. Introduction

In his dissertation [17], Selzer presented the modified summation, which is written solely with active phases, whereby the local active phases should be known a-priori. Inspired by this procedure, an alternative solution of the conflict with the Lagrange multiplier follows, so that the summation over all phases remains, but the Lagrange multiplier takes solely active phases into account. Thus, by introducing the indicator function for every phase-field variable as

$$\chi_\alpha = \begin{cases} 1, & \phi_\alpha \neq 0 \\ 0, & \phi_\alpha = 0, \end{cases}$$

the summation constraint rewrites to

$$g(\boldsymbol{\phi}) = \sum_{\alpha=1}^N \chi_\alpha \phi_\alpha - 1 = 0.$$

This formulation implies information about the volume fraction constraint and about the local presence of the phase. Consequently, the derivative of the constraint is

$$\frac{\partial g(\boldsymbol{\phi})}{\partial \phi_\alpha} = \chi_\alpha,$$

and the corresponding Lagrange multiplier becomes

$$\Lambda_{new} = \frac{1}{N_A} \sum_{\alpha=1}^N \frac{\delta \mathcal{E}}{\delta \phi_\alpha}, \quad (2.17)$$

with the number of active phases as $N_A = \sum_{\alpha=1}^N \chi_\alpha$.

Therefore, the phase-field evolution equation takes a new form as

$$\tau \epsilon \partial_t \phi_\alpha = -\frac{\delta \mathcal{E}}{\delta \phi_\alpha} - \chi_\alpha \Lambda_{new}, \quad \forall \alpha \in \{1, \dots, N\}, \quad (2.18)$$

and if also the phase is not present locally, its indicator function and the corresponding variational derivative vanish by the definition and by the assumption, respectively. And although the Lagrange multiplier is non-vanishing, the right-hand side of the phase-field equation is zero for a non-present phase.

The evaluation of the Lagrange multiplier, with respect to eq. (2.17), in the resulting phase-field equations, eq. (2.18), was applied in the PACE3D solver long ago and is the essence of the optimisation tool *active phases*.

3. Grain Structure Evolution during Electron Beam Welding

Already in the chalcolithic and in the earlier bronze age, since the people tried to produce metallic objects, they were faced with the challenge to join different metallic samples. Over thousand years, the joining methods rather made little progress, but in the 19th century, the development was rapid. Since the fifties of the last century, electron beam welding (EBW) has developed into a process with a stable material-locking connection.

Presently, this joining method belongs to one of the most important merging procedures. The speed and the power flux density of the electron beam are decisive for the heat input and also for the resulting weld seam quality [53, 54]. Because of the possibilities to deflect the electron beam, the aimed positioning of the welded joint and the specific formations of heating can be achieved. Therefore, EBW techniques can be used particularly well for thermal joining, surface hardening, separation and remelting of metallic materials [53, 54]. Moreover, EBW is gaining popularity as a result of enormous beam powers, low energy consumption, good energy efficiency and the limited heat-affected zone. Using the citation from [55], *"advantages of EBW welding include high depth-of-penetration, minimum joint preparation, a narrow weld heat-affected zone, low distortion, and excellent weld cleanliness as welding is performed in a high vacuum. Disadvantages of the EBW process include high capital equipment cost and high weld cooling rates, the latter of which promote formation of undesirable martensite in the weld zone."*

Furthermore, it should be mentioned that an added advantage is the rapid distractibility of the electron beam, which makes it possible to create two different parallel welds without solidifying a molten bath in the meantime. For these reasons, it will remain a high-quality welding process, now and in the future, that will be used in many fields of application, such as space, aviation and the automotive, electrical and nuclear industry.

Since this method is usually associated with human-hazardous radiation, the work environment and the beam must be adequately secured. The schematic explanation of the working principle of the electron beam welding machine is given in Figure 3.1.

3. Grain Structure Evolution during Electron Beam Welding

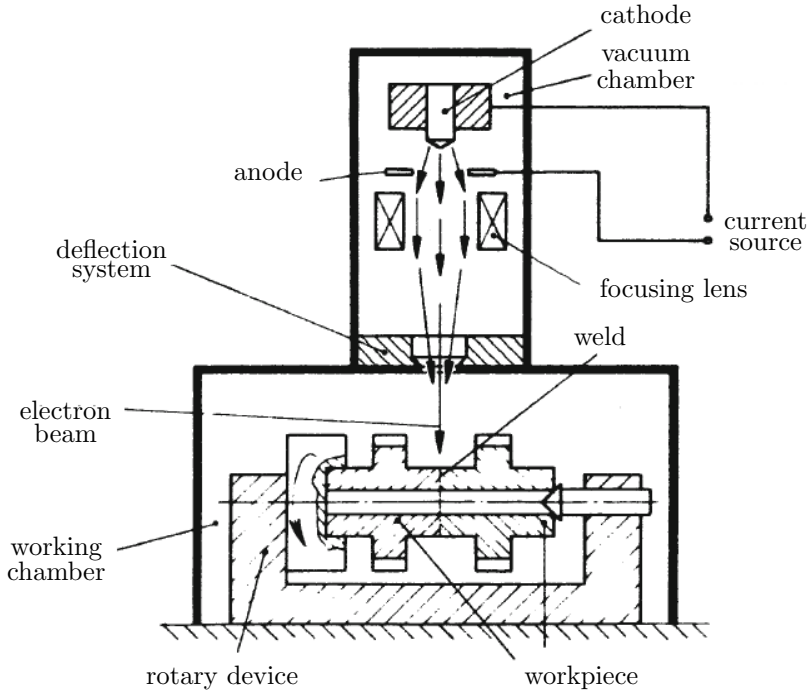


Figure 3.1.: Electron beam welding – the main working principles. [1]

Within the beam generator system, the electrons are emitted. By applying a high-voltage field, the electrons are accelerated from the cathode towards the anode. After reaching the end of the anode, the electrons have their final velocity and are bundled inside the focusing lens. When arriving at the deflection system, the electron beam is distracted due to the requirements of the heat source at the workpiece [56]. The required thermal energy is produced by the conversion of the kinetic energy when the electrons strike the material. To prevent the undesired deflection of the electrons from colliding with air molecules, a vacuum should prevail in the working chamber. During the irradiation process, the welding sample can be rotated within the rotated device [1, 54]. For more information, the interested reader, among other things, is referred to [22].

3.1. Problem statement

The objective of the further approach is the modelling of the microstructure evolution during EBW of two joint ferrite samples, see Figure 3.2. To resolve the morphology change, three different phenomena are considered in this work: (1.) grain growth, (2.) coarsening in the heat-affected zone and (3.) nucleation of new grains inside the weld bath zone.

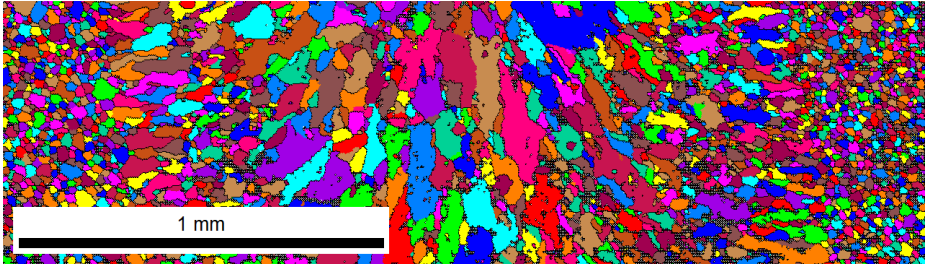


Figure 3.2.: EBSD image for a view from above on the horizontal plane of the welded seam of two ferritic steel samples. The welding direction is from bottom to top. The weld was done at KIT, IAM-AMP by V. Widak, M. Rieth.

In order for both the real and virtual experiments to correspond to each other, the process parameter of the welding and the thermodynamical material parameters should be used in the simulations. The immediate problem that has arisen at the beginning of this project is the multiplicity of the simultaneous processes, which occur at different positions of the weld bath.

First, the power of the electron beam is chosen so high that most metals evaporate. The keyhole of the penetrated electron beam is unstable in this formation [23]. The induced vapour pressure inside the keyhole [23] and the surface tension of the melt, which is dependent on the temperature, drive the melt flow [23, 22], and consequently, the heat and mass convection. During the solidification process, the counterplay of the solidification velocity and the cooling rate produce different morphological structures at different places at the fusion surface [22, 3]. The theoretical determination of a different microstructure is explained by the stability of the solidification front, due to the balancing thermal, interfacial, kinetic and constitutional undercoolings.

By the comparison of the characteristic length scales of the processes, there is a high distinction between the magnitudes. The weld seam width in the experiment is of around 1-2 mm. Because of a narrow heat-affected zone, an additional

3. Grain Structure Evolution during Electron Beam Welding

width of around 1 mm should be taken into account. When the modelling of the processes inside the keyhole is ignored, and solely a simple model of the heat source is used, the heat distribution inside the sample can be modelled with the convectonal heat conduction equation [2, 22]. The characteristic lengths of the heat and mass diffusion processes are determined by the diffusivity constants and are of around 10^{-2} mm and 10^{-5} mm, respectively.

The length scale of the considered process determines the resolution of the simulation domain. Therefore, in order to simultaneously resolve the dimension of the weld seam and heat-affected zone and the diffusion driven processes during the solidification, the size of the simulation domain is of some millimetres in size, and the grid cell width shall be of some hundred nanometres. Hence, with the numerical scheme in sec. 2.2 (finite differences on equidistant grid), the simulation domain increases to several ten thousand cells in every direction. Furthermore, the stable discrete time step for the explicit Euler scheme diminishes to nanoseconds. Both the gigantic number of grid cells and the nanoscopic time scale make it impractical to perform this kind of simulation, even when applying parallel computing on a super cluster. Hence, it remains a vision for future works because of the complexities in the quantitative modelling of coupled processes, in the efficient numerical performance and in the visualisation of the simulation results.

The alternative procedure to overcome the conflict of the length scales is to change the viewing angle. There is a step to resolve the problem, beginning from the smallest length scale. In the chosen region of the fusion zone, the authors exemplarily analysed the dendrite growth into the weld bath in [57, 58] by using a phase-field model. Doing so, the temperature field is assumed to be quasi-equilibrated and prescribed as external field for the morphological formation. In this thesis, an alternative perspective is presented. Orienting on the maximal length scale due to the weld seam dimension, and refining the simulation domain resolution, the other physical processes are incorporated in the calculation by achieving the corresponding length scale, whereby processes for a smaller length scale are neglected. In this way, the macroscopic temperature field can be resolved with a permissible number of grid cells. But the problem of the feasible temperature boundary condition occurs at the simulation domain borders.

Though, to make the first steps in the proposed direction, the following working steps are presented in the next section. The temperature field in the welded samples is assumed to be quasi-stationary and to be decoupled from transitional and convective processes. After the determination of the macroscopic temperature field distribution, this is applied as an externally moving field. The base material consists of globular grains with an average diameter of around $50 \mu\text{m}$, which are melted at the weld bath front, and the solidification occurs from the weld bath

periphery towards the seam symmetry axes, with respect to the moving temperature gradient. The phase-field model is extended with a nucleation model to represent heterogeneous nucleation of new grains inside the weld bath.

3.2. Macroscopic temperature field

In this section, I use a model for the heat source, inspired by the works of [24, 59, 60, 61, 62]. As mentioned, the keyhole instabilities are neglected. Thus, the power distribution is time-independent, but moves with constant welding velocity. Because of the depth penetration of the electron beam, and consequently of the power density into the materials, the heat source term in the heat conduction equation is not only defined on the sample surface, but also within the sample. The heat conduction can be described in different reference systems. Since the Eulerian coordinates are (x, y, z) , the Lagrangian coordinates are given as (w, y, z) , whereby v is the uniform welding velocity in x -direction and $w = x - vt$ [2], see Figure 3.3.

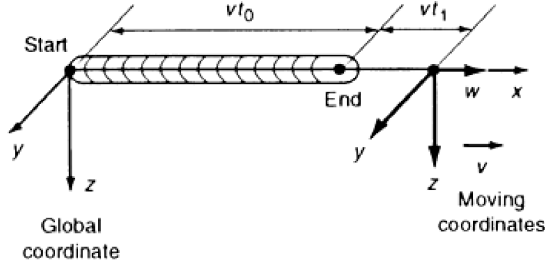


Figure 3.3.: Global and moving coordinate systems for welding heat conduction [2].

3.2.1. Heat conduction evolution equation

The heat conduction equation for heat flow in the moving frame writes as [2]

$$\nabla \cdot (\lambda \nabla T) + \rho c_p v \frac{\partial T}{\partial w} + P = \rho c_p v \frac{\partial T}{\partial t}. \quad (3.1)$$

In the previous equation, the thermal diffusivity λ , the specific heat c_p and the density ρ of the material are assumed to be constant and temperature-independent. This assumption makes it possible to determine the analytical solutions for a point power source on the top as well as for multifocus heat

3. Grain Structure Evolution during Electron Beam Welding

sources, by the usage of the superposition principle [63]. P corresponds to both the external power source and the heat of fusion. If the phase transition takes place, the last is neglected in the temperature determination.

The initial condition $T(x, y, z) = T_0$ is at the initial time $t = 0$. In addition to the initial conditions, the geometry of the welding samples, and also the heat loss at the workpiece boundary should be known in order to calculate the (analytical and/or numerical) solution of heat conduction, eq. (3.1). In this work, the heat boundary conditions at the top surface are assumed to be adiabatic $\partial_z T(z = 0) = 0$, and furthermore, the sample is assumed to be very large (infinitely large), so that $T(x \rightarrow \pm\infty, y \rightarrow \pm\infty, z \rightarrow \infty) \rightarrow T_0$.

The engineering solution is given with the specific point (x, y, z) in the material, whose distance to the moving heat source

$$r = \sqrt{(x - vt)^2 + y^2 + z^2}$$

is time-dependent. Since the quasi-stationary temperature distribution for a point power source p writes as [2]

$$T(w, y, z) = T_0 + \frac{p}{2\pi\lambda r} e^{-\frac{v(r+w)}{2a}}, \quad (3.2)$$

for multiple foci, it results in the superposition of the partial solutions [63],

$$T(w, y, z) = T_0 + \sum_{i=1}^n \frac{p_i}{2\pi\lambda r_i} e^{-\frac{v(r_i+w_i)}{2a}}, \quad (3.3)$$

with thermal diffusivity $a = \frac{\lambda}{\rho c_p}$ and with specific distance r_i to the location of the partial heat source p_i .

3.2.2. Model for the heat source

Inspired by the temperature estimations in the welded samples during electron/laser beam welding [61, 62], and by the modelling of the volumetric power density, not only at the top surface, but also inside the welded materials [59], the used volumetric heat source writes as

$$p(\chi, \xi, \zeta) = \begin{cases} \left(1 - \frac{\zeta}{h}\right) \frac{2\eta P A^2}{h\pi R^2} e^{-\frac{A^2(\chi^2 + \xi^2)}{R^2}}, & \text{for } \begin{matrix} (\chi^2 + \xi^2) \leq R \\ 0 \leq \zeta \leq h \end{matrix} \\ 0, & \text{else.} \end{cases}$$

Here, R and h are the effective radius and the effective depth of the electron beam, respectively. The term $\frac{2PA^2}{h\pi R^2}$ also consists of the total electron beam

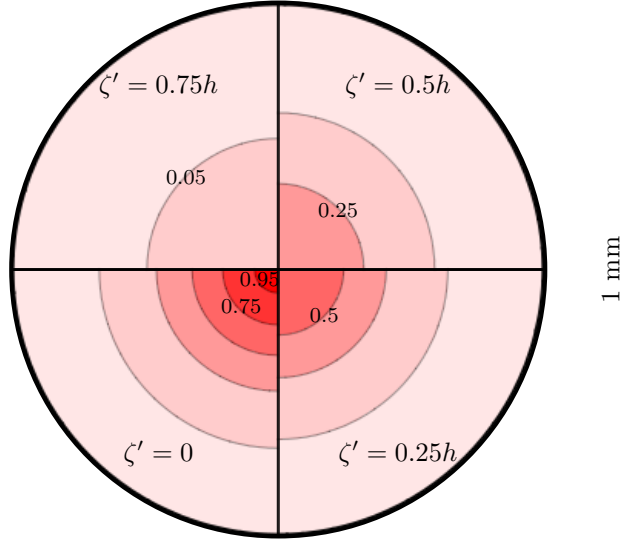


Figure 3.4.: Contour lines of normalised power density distribution $\frac{p(\chi, \xi, \zeta)}{2\eta PA^2/h\pi R^2}$ on different depths: $\zeta' = 0$, $\zeta' = 0.25h$, $\zeta' = 0.5h$, $\zeta' = 0.75h$.

power P and of the efficiency coefficient η . The parameter $A = 2.57$ stands for the variance by the distribution and arranges the width of the Gaussian¹.

Here, the volumetric power density is formulated inside a cylinder V_c , and I introduce its volume element $dV_c = d\chi d\xi d\zeta$ for the shorthand notation. In Figure 3.4, the normalised volumetric power density is shown for the following depths, on the top $\zeta = 0$ and in the quarter steps of the effective beam depth h .

Note that the integration of the volumetric power density results in the induced effective electron beam power

$$\eta P \approx \int_{V_c} p(\chi, \xi, \zeta) dV_c.$$

There are also different approaches to model the volumetric heat sources. In their works [60, 24], Goldak et al. presented *Gaussian surface flux distribution* and *hemispherical power density distribution* on the welded surface, and *ellipsoidal*

¹Johann Carl Friedrich Gauß, 30.04.1777 - 23.02.1855. German mathematician, physicist, mechanician, astronomer and geodesist. Referred to as *the foremost of mathematicians*. Lunar crater Gauss and asteroid 1001 Gaussia are named after him.

3. Grain Structure Evolution during Electron Beam Welding

power density distribution and double ellipsoidal power density distribution, not only on the surface, but also within the welded domain. Thus, the geometrical definition area, in which the power density is formulated, could be of arbitrary type and could be adopted by means of experimental measurements.

3.2.3. Analytical and closed-form solutions

Analytical temperature field

By applying the principle of superposition, eq. (3.3) for the continuous power density distribution, the analytical solution for the quasi-equilibrium temperature distribution writes as

$$T(w, y, z) = T_0 + \frac{1}{2\pi\lambda} \int_{V_c} \frac{p(\chi, \xi, \zeta) e^{-\frac{v}{2a} (\sqrt{(w-\chi)^2 + \xi^2 + \zeta^2} + (w-\chi))}}{\sqrt{(w-\chi)^2 + \xi^2 + \zeta^2}} dV_c. \quad (3.4)$$

Unfortunately, the previous equation is given in an analytical form and not as a closed-form solution. The mentioned approach to simulate the morphology change inside the welded seam and in the heat-affected zone requires the macroscopic temperature field in a closed form. The numerical integration of the required temperature value at the discrete position (x', y', z') in the simulation domain is computationally very expensive and inefficient. Therefore, an alternative method is suggested.

Approximated temperature field

The temperature field, eq. (3.4), will be evaluated numerically at the horizontal sample cuts with constant depths and with the parameters given in Table 3.1.

parameter	P	η	v	R	h	λ	a	T_0
unit	W	-	cm/s	mm	mm	W/mK	mm ² /s	K
value	1800	0.95	1	0.5	7	10.9	3.163	293

Table 3.1.: Parameters for the numerical evaluation of the temperature distribution due to the analytical solution eq. (3.4).

The analytical temperature distribution will be approximated with an approach

$$T^{app}(w, y) = T_0 + \frac{n}{z+d} (c_w w^3 + q_w w^2 + l_w w + q_y y^2 + a) e^{kw} \quad (3.5)$$

3.2. Macroscopic temperature field

on the horizontal planes parallel to the welding direction, and for some depths.

Since the analytical solution near the heat source is not precise, nevertheless, it is well established for the determination of the cooling rate for the phase transition [2], and consequently for the determination of the microstructure [3]. Therefore, for the solidification, the temperature distribution around the melting temperature

$$T_M = 1780 \text{ K} \quad (3.6)$$

is relevant for the morphology formation. In this study, the isotherms

$$T_{iso} = \{1500, 1700, 1800, 1900, 2100\}$$

are used for the approximation and the accurate fitting. The approximation function can be expanded with additional terms and the temperature range can be enlarged.

During the search of the appropriate approximation function, it has become possible to find such a formulation (3.5) that the coefficients n , d and a could be chosen as constant with the magnitudes $n=7000 \text{ mm K}$, $d=40 \text{ mm}$ and $a = 14$. Thus, in eq. (3.5), the expression in the parentheses as well as the exponent are dimensionless. The values for other parameters are listed in the next table, Table 3.2, for several depths z , so that w , y and z are given in millimetres.

z	c_w	q_w	l_w	q_y	k
0.0	0.481837	-1.68117	10.3509	-10.2257	-0.485826
0.5	0.219156	-1.54258	9.52342	-7.23715	-0.348015
1.0	0.151333	-1.36236	9.18821	-6.3951	-0.299643
1.5	0.136274	-1.27143	9.27252	-6.25273	-0.290046
\vdots	\vdots	\vdots	\vdots	\vdots	\vdots

Table 3.2.: Parameters for the approximated temperature distribution. The approximation procedure was done by using WolframMathematica8.

In order to avoid confusion, the coefficients l_w and k are given in $1/\text{mm}$; q_w and q_y are the coefficients for the quadratic terms, and consequently have the unit of $1/\text{mm}^2$. Finally, the coefficient for the cubic term is written in $1/\text{mm}^3$. Afterwards, the coefficients could be interpolated or fitted to the functions $c_w(z)$, $q_w(z)$, $l_w(z)$, $q_y(z)$, $k(z)$, with an appropriate approach.

The numerical evaluation of the analytical solution eq. (3.4) as well as the approximative temperature field eq. 3.5 with process and material parameters in Table 3.1 and with the fitting parameters in Table 3.2 both are shown in form of isotherms at different depths: on the top, for $z = 1 \text{ mm}$ and for $z = 4 \text{ mm}$;

3. Grain Structure Evolution during Electron Beam Welding

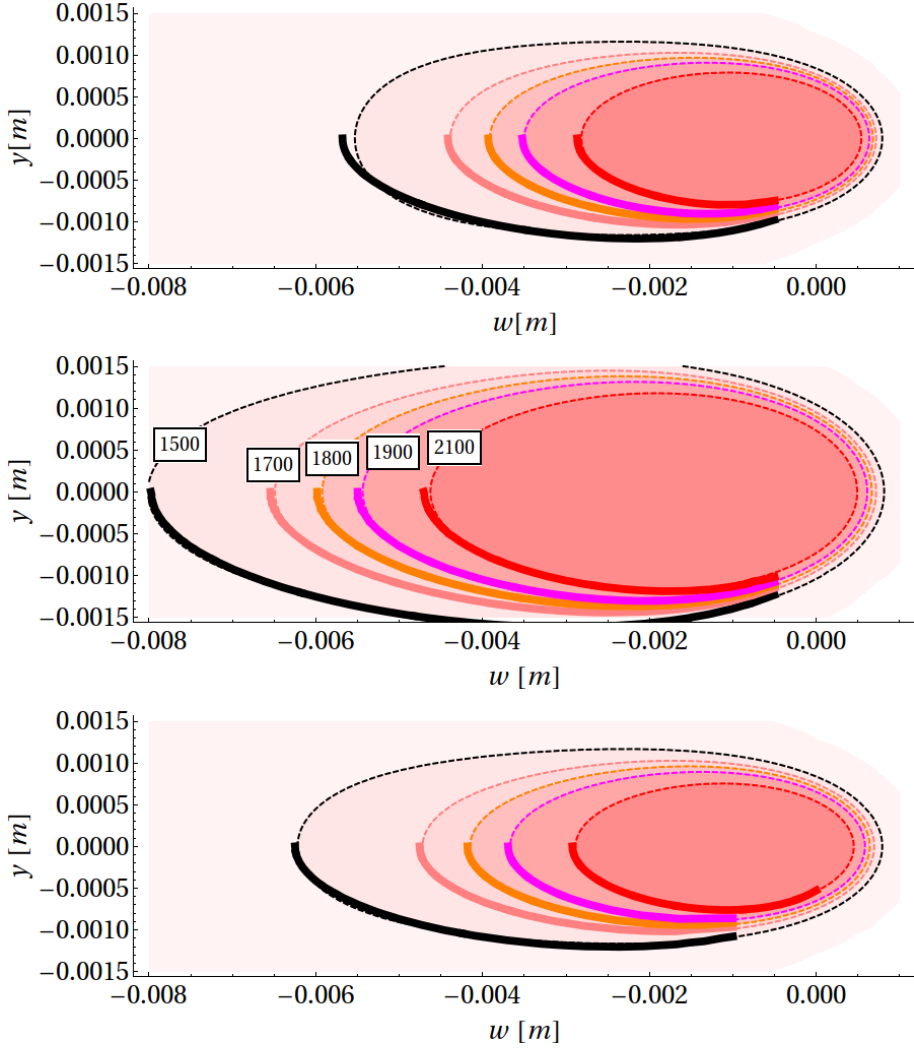


Figure 3.5.: Isotherms at different depths, $z = 0$ mm on the top, $z = 1$ mm in the middle and $z = 4$ mm on the bottom. Solid and dashed lines correspond to the numerical evaluation of the analytical solution $T^{ana}(w, y, z = const)$ in eq. (3.4) and to the approximation $T^{app}(w, y)$ in eq. (3.5), respectively.

hence, for horizontal planes parallel to the welding direction and perpendicular

to the electron beam, see Figure 3.5. There is an excellent agreement between the analytical solution and the approximated solution. The decisive advantage of the approximated solution, eq. (3.5), in comparison to the analytical solution, eq. (3.4), is its closed form. Now it is possible to use the temperature field distribution in the simulation with manageable computational effort.

In the student project [64], which was also supervised by the author of this thesis, an alternative approximation approach was suggested. In contrast to the current procedure, the original temperature field was not given by the analytical expression, but as a discrete field from the welding process simulation. Disadvantageously, the used approximation function was done solely for a special isotherm, and the approximated temperature field was given in the implicit form. Therefore, in order to use the approximation in the grain structure simulations, the Newton² iteration should be evaluated in every domain cell and in every time step. In view of the computational efficiency, the method in [64] loses against the presented approach, eq. (3.5). From the other point of view, it realises the alternative possibility to determine the required temperature field.

3.3. Phase-field model for grain evolution

In Figure 3.2, the microstructure of the welded sample can be separated into three different regions. On the left and on the right boundary of the figure, the morphology corresponds to the base material. The average grain size is around 50 μm in diameter. Moving to the centre, the region with longitudinal grains, which are perpendicular to the welding direction, sign the boundary between the heat-affected zone and the weld. In the welded seam, different grain structures are present.

Initially, two processes will be qualitatively reproduced with the phase-field model: the phase transition between liquid and solid and the grain coarsening. Since the transitional solid and liquid phases are driven by the difference in their temperature-dependent Helmholtz free energies the solid-solid state transformation is inter alia driven by the interfacial energy during grain coarsening in the heat-affected zone.

²Sir Isaac Newton, 25.12.1642 – 20.03.1726, English mathematician, astronomer and physicist. He is a key figure in the scientific revolution and is recognised as one of the most influential scientists of all time. Lunar and Martian craters Newton are named after him.

3. Grain Structure Evolution during Electron Beam Welding

3.3.1. Evolution equations

In the explicit form, the phase-field evolution equation for phase transformation, eq. (2.5), writes as

$$\tau(T)\partial_t\phi_\alpha = \nabla \cdot \underbrace{\frac{\partial a(\phi, \nabla\phi)}{\partial \nabla\phi_\alpha} - \frac{\partial a(\phi, \nabla\phi)}{\partial \phi_\alpha} - \frac{1}{\epsilon^2} \frac{\partial w(\phi)}{\partial \phi_\alpha} - \frac{1}{\epsilon} \frac{\partial f(T, \phi)}{\partial \phi_\alpha}}_{rhs_\alpha} - \chi_\alpha \Lambda, \quad (3.7)$$

with the gradient energy [20, 40, 46]

$$a(\phi, \nabla\phi) = \sum_{\alpha\beta} \gamma_{\alpha\beta} |\mathbf{q}_{\alpha\beta}|^2, \quad (\mathbf{q}_{\alpha\beta} = \phi_\alpha \nabla\phi_\beta - \phi_\beta \nabla\phi_\alpha), \quad (3.8)$$

the multi obstacle potential

$$w(\phi) = \begin{cases} \frac{16}{\pi^2} \sum_{\alpha,\beta} \gamma_{\alpha\beta} \phi_\alpha \phi_\beta + \sum_{\alpha,\beta,\delta} \gamma_{\alpha\beta\delta} \phi_\alpha \phi_\beta \phi_\delta, & \phi \in \mathcal{G} \\ \infty, & \phi \in \partial\mathcal{G} \end{cases} \quad (3.9)$$

and with the free energy

$$f(T, \phi) = \sum_{\alpha=1}^N f^\alpha(T) h_\alpha(\phi_\alpha). \quad (3.10)$$

In (3.9), \mathcal{G} represents the Gibbs³ simplex $\mathcal{G} = \{\phi = (\phi_1, \dots, \phi_N) \mid \sum_{\alpha=1}^N \phi_\alpha = 1, \phi_\alpha \geq 0\}$. The Lagrange multiplier Λ in the phase-field equation (3.7) corresponds to the case of *active phases* in eq. (2.17) and χ_α is the characteristic function as in eq. (2.18).

In the following, simulations with a high number of phases in large simulation domains are preformed. On the one hand, the storage of every phase-field is very costly and otherwise unnecessary. In order to distinguish different grains, the scalar field of the phase-field index is saved. Therefore, in every cell in the simulation domain, the phase index with the highest phase-field value is allocated, also in the multiphase junction. Furthermore, the moving temperature field, and if required the liquid phase distribution, are also saved for the visualisation of the simulation in order to interpret the results.

³Josiah Willard Gibbs, 11.02.1839 – 28.04.1903, American physicist, chemo-physicist, mathematician and mechanic. He is one of the founders of vector analysis, statistical physics and mathematical theory of thermodynamics.

3.3. Phase-field model for grain evolution

By a total number of phases N , the last index corresponds to the liquid phase. Thus, $\phi_l = \phi_{N-1}$. Other $N - 1$ phase indices

$$\alpha \in \{0, \dots, N - 2\}$$

represent different grains.

3.3.2. Dimensioning of the simulation domain

As mentioned, the average grain size is $50 \mu\text{m}$ in diameter. Using the phase-field method, the sharp boundary between the neighbouring phases will be stretched to an artificial diffuse interface width, Figure 2.1. The benchmark of the permitted dimensioning is the usage of the maximal resolution, which can resolve both the bulk and the interface. By using a constant spatial step of

$$\Delta x = \Delta y = \Delta z = 4 \mu\text{m},$$

every grain consists of approximately 12 grid cells in diameter. Together with the model parameter

$$\epsilon = 14 \mu\text{m},$$

which corresponds to the diffuse interface width W of around 8-9 grid cells, there are sufficient cells to resolve the diffuse interface as well as the bulk volume. Furthermore, the gradient energy, eq. (3.8), is numerically resolved with acceptable accuracy, and the computational interfacial energy will correspond to its physical counterpart, eq. (2.11).

The temporal time step is chosen in accordance with the criterion

$$\Delta t = 10^{-5} \text{ s} \leq \frac{\tau \Delta x^2}{6\gamma}, \quad (3.11)$$

for the phase-field equation, eq. (3.7), discretized with a presented numerical scheme in sec. 2.2 in three dimensions and with respect to the simulation parameters, which are subsequently defined. The previous criterion for the temporal and spatial steps is derived using the von Neumann⁴ stability analysis.

⁴John von Neumann (Hungarian: Neumann János Lajos), 28.12.1903 – 8.02.1957. Hungarian-American mathematician, physicist, inventor, computer scientist and polymath. He made major contributions to numerical analysis, set theory, quantum physics, functional analysis, informatics, economy and other topics. The crater *von Neumann* on the Moon is named after him.

3. Grain Structure Evolution during Electron Beam Welding

3.3.3. Initial filling

The initial filling of the grains in the simulation domain is performed in the following manner. In the first step, the initial filling procedure only sets the grain with the first index in the whole simulation domain. For the filling liquid phase within the weld bath, the temperature field is used. When the local temperature is higher than the melting temperature, the liquid phase replaces the solid phase. Next, the volume V_0 of the remained solid phase will be calculated and divided by the volume of the average grain with $50 \mu\text{m}$ in diameter. The rounded result determines the total number of grains, N^{tot} . Then, using $N - 1$ different grains, the Voronoy⁵ tessellation is used to fill N^{tot} points in the present grain. In this work, I used the maximal 500 different solid phases, but the number of grains in the simulations domain can be of several ten thousand. See top image in Figure 3.9 for an example of an initial setup. For more details about the implementation of the Voronoy filling algorithm in PACE3D, an interested reader is referred to [65].

3.3.4. Parameters for interfacial energy

By applying the phase-field model to the grain evolution, the crystalline structure of every grain could also be taken into account by using anisotropic surface energy and anisotropic kinetics. In spite of the fact that every grain is anisotropic in the sense of its crystallographic nature, the macroscopic entirety of all grains seems to be isotropic in thermal, mechanical and other properties. Hence, for simplification, the surface energy parameter in the gradient energy as well as in the potential is assumed to be isotropic and equal for both solid-liquid and solid-solid interfaces. The used value is

$$\gamma_{\alpha\beta} = 0.2 \text{ Jm}^{-2} \quad \text{for all } \alpha \text{ and } \beta.$$

The higher-order term, $\gamma_{\alpha\beta\delta} = 2\text{Jm}^{-2}$ for all $\alpha, \beta, \delta \in [1, N - 1]$, in the multi obstacle potential, eq. (3.9), is introduced to suppress the third phases in the diffuse interface [66]. In [67], we derived a method to measure the angles in the multiphase junctions and showed a calibration procedure for the higher-order term.

3.3.5. Bulk energies

The interpolated Helmholtz free energy, eq. (3.10), can be written with absolute values of the potentials; but it is more convenient to relate all Helmholtz energies

⁵Georgy Feodosevich Voronoy, 28.04.1868 – 20.11.1908. Russian mathematician; among other things, he defined the Voronoy diagram.

3.3. Phase-field model for grain evolution

to a special one, because not the absolute magnitude, but the potential differences are relevant. Taking the Helmholtz free energy of a solid as the reference potential, the Helmholtz free energy density vanishes for every solid grain and writes as

$$f_l(T) = -L \frac{T - T_M}{T_M},$$

for the liquid phase. $L = 3 \cdot 10^9 \frac{\text{J}}{\text{m}^3}$ is the latent heat of fusion, and T_M is the predefined melting temperature, eq. (3.6). Thus, the interpolated Helmholtz free energy density respectively writes as

$$f(\phi, T) = f_l(T)\phi_l. \quad (3.12)$$

3.3.6. Kinetic coefficients

The kinetic coefficient τ in eq. (3.7) represents the dynamic behaviours of both the interface motion due to the grain growth in the weld bath and grain boundary movement due to the coarsening in the heat-affected zone. For simplification, isotropic kinetic coefficients are assumed in both situations. Furthermore, the kinetic coefficient for the solid-liquid interface is assumed to be constant,

$$\tau_{sl}(T) = 8 \times 10^5 \text{ Jsm}^{-4}, \quad (3.13)$$

and was determined in the preliminary one-dimensional simulation study, so that the kinetic undercooling at the welding symmetry axes consists of approximately 10 K.

Since it is difficult to get the kinetic coefficient for coarsening from an experiment, two simulations were performed in order to get an idea in which range the kinetic coefficient should be placed. In the first simulation, the kinetic coefficient is chosen in the order similar to the solid-liquid coefficient, eq. (3.13). In the second simulation, the kinetic coefficient becomes different in three orders, similar to the mass diffusion coefficients in solid and liquid phases, which also differ in three orders. Thus, the following values are used:

$$\tau_{\alpha\beta}^{test1} = 9 \times 10^6 \text{ Jsm}^{-4} \quad \text{and} \quad \tau_{\alpha\beta}^{test2} = 9 \times 10^8 \text{ Jsm}^{-4}.$$

In the multiphase junctions, the kinetic coefficient is given as

$$\tau = \frac{\sum_{\alpha,\beta} \tau_{\alpha\beta} \phi_\alpha \phi_\beta}{\sum_{\alpha,\beta} \phi_\alpha \phi_\beta}. \quad (3.14)$$

In Figure 3.6, the first simulation results for the phase-field model are presented. For the chosen solid-solid kinetic coefficient $\tau_{\alpha\beta}^{test1}$, the grain coarsening also

3. Grain Structure Evolution during Electron Beam Welding

appears in the base material, before the weld front arrives. This is not the case in the real process. Therefore, this kinetic coefficient is impractical.

Simulation results for the second solid-solid kinetic coefficient $\tau_{\alpha\beta}^{test2}$ are shown in Figure 3.7. Remarkably, the morphology remains unchanged until the weld front arrives. But the advancing liquid interface is hindered by the slow solid-solid

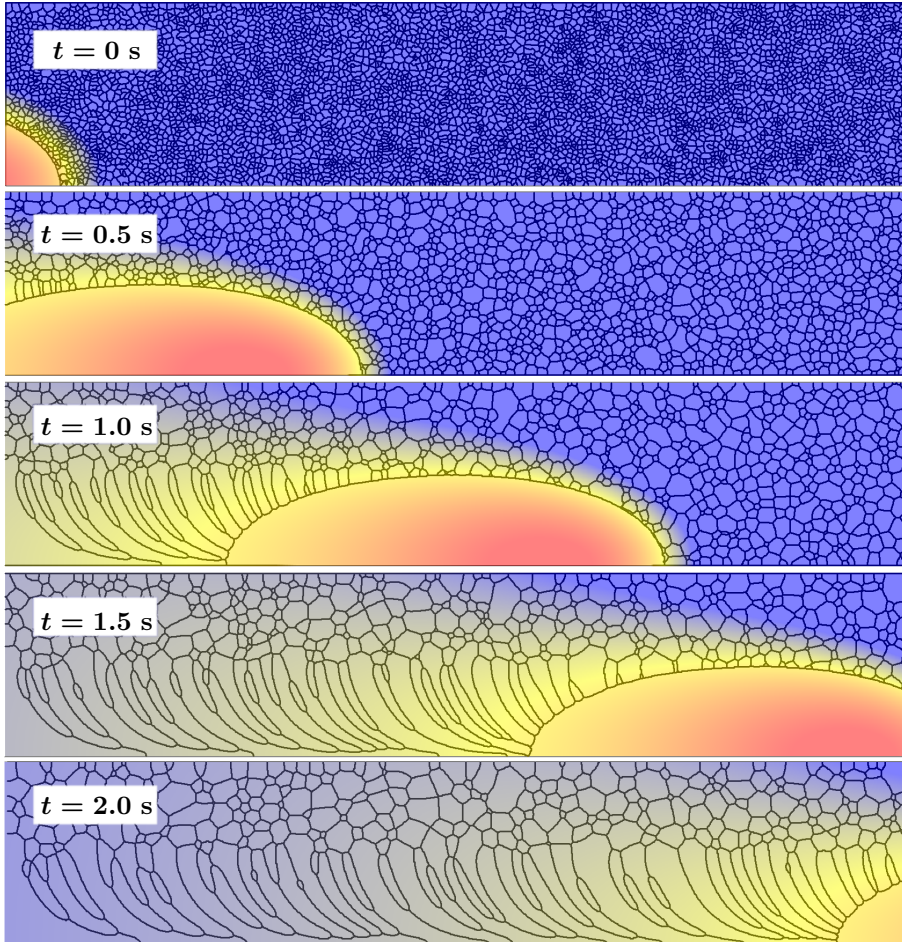


Figure 3.6.: Simulation results of a temporal sequence with a time step of 0.5 s for the solid-solid kinetic coefficient, $\tau_{\alpha\beta}^{test1}$. The changing mesh corresponds to the grain boundary motion, and the coloured field is the temperature field which moves through the simulation domain.

3.3. Phase-field model for grain evolution

interaction. Since the bulk grain transforms rapidly to the liquid, the diffuse grain-grain interfaces melt more slowly because of the interpolated kinetic coefficient, eq. (3.14). Therefore, the total fusion of grains occurs slowed, and by the arrival of the temperature values much higher than the melting temperature.

The columnar grain structure in the welded seam in the second simulation series,

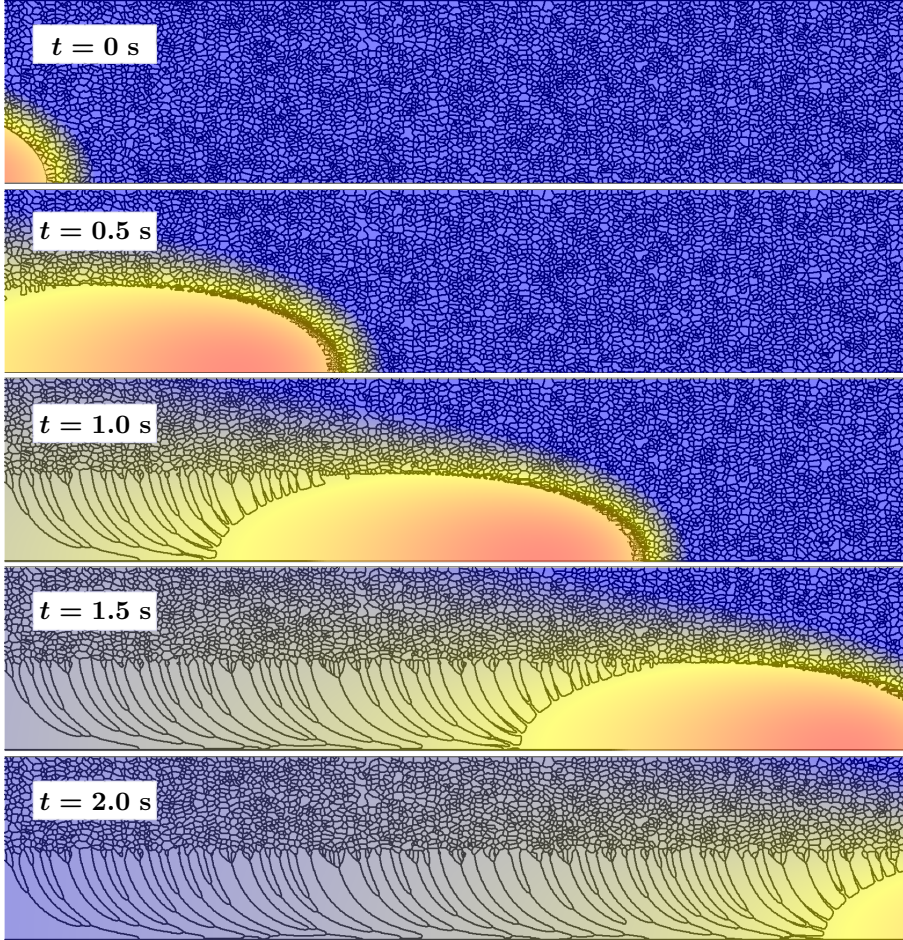


Figure 3.7.: Simulation results of a temporal sequence with a time step of 0.5 s for the solid-solid kinetic coefficient, $\tau_{\alpha\beta}^{test2}$. The changing mesh corresponds to the grain boundary motion, and the coloured field is the temperature field which moves through the simulation domain.

3. Grain Structure Evolution during Electron Beam Welding

Figure 3.7, differs from the first test case, Figure 3.6. While the grains in the weld follow the moving temperature gradient in both scenarios, the increasing width of the columnar grains in the first scenario results from the enlarged parental grains at the directly welded seam periphery.

Inspired by the previous findings, and in order to resolve coarsening in the heat-affected zone, the kinetic coefficient for grain-grain interfaces is modelled isotropically, but temperature-dependent [68]. The used function for the grain-grain interface mobility writes as

$$M_{\alpha\beta}(T) = \begin{cases} 10^{-6} e^{-7 \times 10^3 T^{-1}} \text{ m}^4 \text{ J}^{-1} \text{ s}^{-1}, & T < T_M \\ 1.96 \times 10^{-8} \text{ m}^4 \text{ J}^{-1} \text{ s}^{-1}, & T \geq T_M \end{cases} \quad (3.15)$$

and is based on the fundamental Arrhenius approach [69], whereby the mobility is the reciprocal kinetic coefficient $\tau(T)M(T) = 1$. For the reason of numerical stability in eq. (3.11), the kinetic coefficient for metastable solid phases is constant for temperatures higher than the melting temperature. The corresponding Arrhenius plot is shown in Figure 3.8.

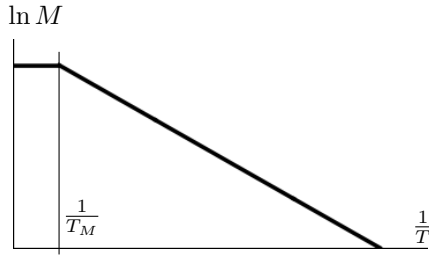


Figure 3.8.: Arrhenius plot for the chosen mobility in eq. (3.15)

Since the previous simulation results, Figures 3.6 and 3.7, were performed with an average grain size of around $100 \mu\text{m}$, the spatial and the temporal step were enlarged, and it was possible to simulate a longer time interval in a bigger physical setup.

In Figure 3.9, the initial grains are of the desired size of 50 microns in diameter, and the spatial and temporal steps are given in sec. 3.3.2. The total simulation domain consists of 1200×2000 cells, and consequently resolves the sample in the area of $5 \times 8 \text{ mm}^2$. In the top image of Figure 3.9, the reader can see a cut of a total simulation domain with physical measurements of 2 mm in height and 4 mm in width. The intensively coloured rectangle in the top image in this figure will be shown later in the next figure 3.10 in order to highlight the grain coarsening in the heat-affected zone.

3.3. Phase-field model for grain evolution

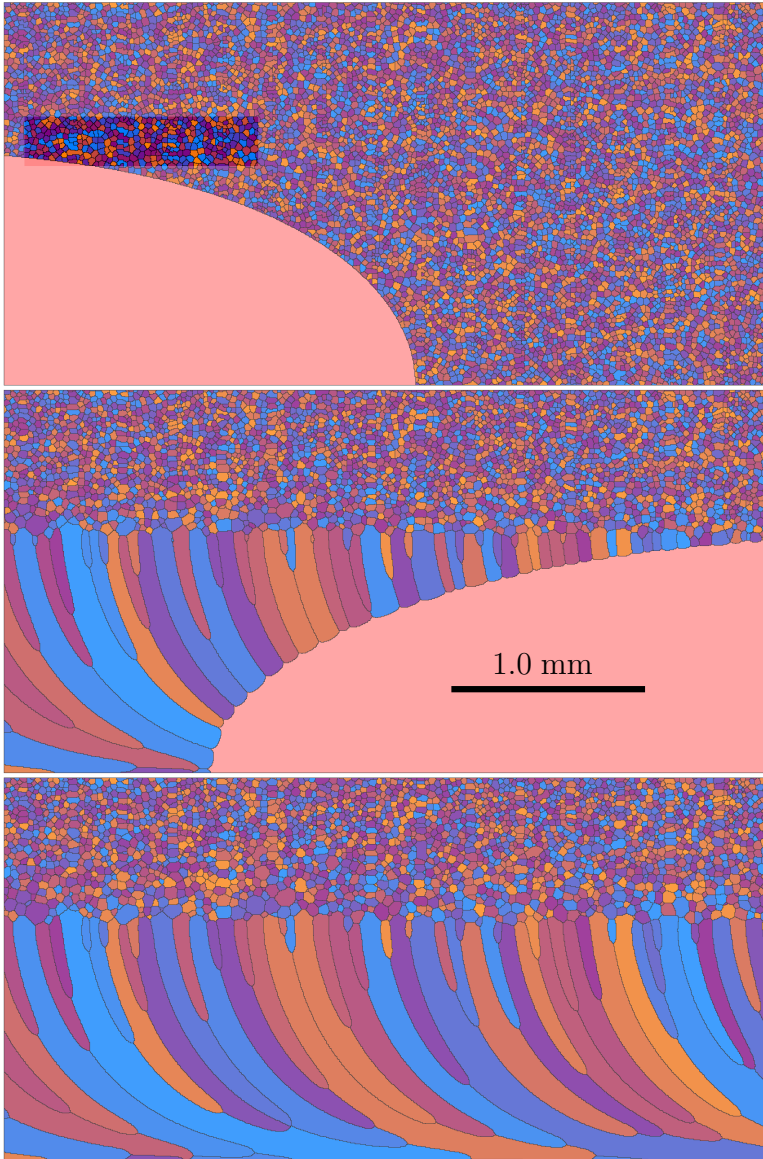


Figure 3.9.: A sequence of the grain structure evolution for the temperature-dependent solid-solid kinetic coefficient. The figures correspond to the time steps 0, 0.5 and 1 s, respectively.

3. Grain Structure Evolution during Electron Beam Welding

In the middle image, the grain growth in the weld appears in similarity to the previous results in Figures. 3.6 and 3.7. But in contrast to the previous result in Figure 3.7, the grain coarsening occurs in the heat-affected zone, see also Figure 3.10. Moreover, on closer inspection of the middle and the bottom pictures in Figure 3.9, the reader can recognise that the long columnar grains in the welded seam in the middle image shrink back in the bottom image after the overgrowth by other grains.

To highlight the grain evolution in the heat-affected zone, while the grain coarsening in Figure 3.9 is difficult to identify, an area of $0.25 \times 1 \text{ mm}^2$, which is marked in Figure 3.9, is shown scaled up in Figure 3.10.

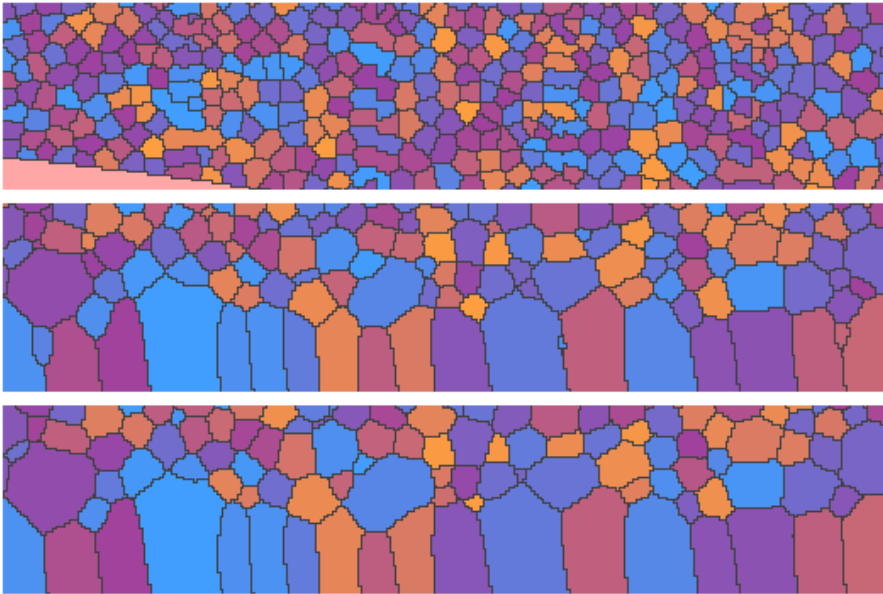


Figure 3.10.: A zoomed area in the heat-affected zone for different time steps.

In the first half second (from top to middle picture), the considered area undergoes high temperatures and the dominant grains grow at the expense of the other grains. Due to the high mobility, the enlarged size of the increased grains is the multiple of the original size. In the last half second (from middle to right picture), the change is there, but not so significant. The recessive small grains vanish and the globular grains are several times bigger than the ones at the beginning.

In summary, the grain growth into the moving weld bath, Figures 3.6, 3.7 and 3.9, and the grain coarsening in the heat-affected zone in Figure 3.10 and in the

solidified weld in Figure 3.9 are qualitatively resolved with the current model. The Arrhenius approach for temperature-dependent mobility, eq. (3.15), is well established to describe the reaction-diffusion processes. The original phase-field evolution equation (3.7) is a reaction-diffusion type equation and the used approach of the temperature-dependent grain boundary kinetics seems to be obvious.

But, disadvantageously, in the presented simulation results, there are missing new grains in the weld bath, which occur in the real welding process, [22, 3]. In the next section, a nucleation model is formulated, which closes this gap.

3.3.7. Model for nucleation

There are text book theories to explain the nucleation processes [22]. The homogeneous nucleation of a new spherical nucleus needs an activation energy, which should be higher than the resulting surface energy. With the decreasing temperature, smaller than the melting temperature, the activation energy increases; therefore, the critical shape curvature of the nucleus increases as well, and a nucleus with smaller critical radius is thermodynamically stable, survives and can grow.

During heterogeneous nucleation, the contamination in form of external solid particles inside the melt accommodates the formation of new grains, which stick to the pollution elements. The activation barrier in the heterogeneous nucleation process is smaller than the magnitude for the homogeneous nucleation, where some energy is released by the partial destruction of the previous spherical interface in the homogeneous nucleation theory. Moreover, the present nuclei can also survive by temperature regimes higher than the melting temperature.

In the welding process, matter convection in the weld bath can also be responsible for the presence and the ensuring growth of new grains inside the weld bath. Thus, the melt flow transports grains detached from the freezing front into the direction of the solidification front, where the latter adhere.

Another procedure to design new grains can be performed with the incorporation of numerical noise into the computational integration of the phase-field equation [70]. A thermodynamically consistent incorporation of thermal noise into the phase-field model was also presented in [71]. With their model, the authors simulated a dendrite growth with side branches. This model has found wide approval in the phase-field community [72, 73] to name just two of over 90 other papers. The main idea of the model is to incorporate thermal noise in the diffuse interface, such that new side branches occur in anisotropic dendrite growth.

3. Grain Structure Evolution during Electron Beam Welding

Independent from the reason of the nucleation in the weld bath, new grains factually arise inside the weld bath and not solely at the solid-liquid interface. Nevertheless, Daubermann tested different noise functions in their bachelor thesis [74], which are defined in the diffuse interface and are implemented in PACE3D. For the purpose of new grain formation, none of the applied noise functions provided satisfactory results. One of the reasons is that the disturbance and grains growth occur on different time scales.

Therefore, an alternative nucleation model was formulated in the bachelor thesis of M. Daubermann. She completed her thesis at the Institute of Applied Materials - Reliability of Materials and Processes under the leadership of Prof. Dr. rer. nat. B. Nestler. By the supervision of the author of the current manuscript, and of the employee of the institute, M.Sc. M. Jainta, the student implemented the ideas to the new nucleation model and performed simulation studies to examine the model. A short overview of the main results of the bachelor thesis, among other things, is published in [75]. Generally, the presented model [74, 75] can be reduced to the consideration of two relevant properties, which can/should depend on temperature. Both variables cover both the probability of the nucleation event $P(T)$ and the set radius of the nucleus $R_n(T)$.

The interested reader is recommended to read the bachelor thesis, but the main principles are explained in this work for completeness. As mentioned in sec. 3.3.1, the integer of the phase-field index $\alpha \in [0, N - 1]$ is saved in every cell to represent the phase-field distribution $\phi(X, Y, Z)$ in the simulation domain. In the spirit of [74], we introduced an additional scalar field, noted in this work as $s(X, Y, Z) \in \mathbb{R}$, with real random values in the defined index interval $[0, N - 1]$. By means of this new scalar field $s(X, Y, Z)$, which is determined in every cell in the simulation domain, we performed the nucleation process algorithmically. Doing so we used two modelling parameters, ξ and P , the temperature field distribution $T(X, Y, Z)$ and the temperature-dependent nucleation amplitude $A(T)$. A schematic diagram of the following algorithm is shown in Figure 3.11.

In the first step, the corresponding phase-field parameter for the liquid phase ϕ_l at the cell with discrete coordinates (X', Y', Z') was referred to as the predefined lower threshold, signed with

$$\xi = \phi_l^{crit}.$$

Because the genesis of new grains can only arise in the melt and only if the local phase-field value of the liquid phase is also higher than the threshold,

$$\phi_l(X', Y', Z') \geq \xi,$$

then this cell is a candidate for the nucleation. Note that the usage of the threshold allows to control the nucleation process, not solely in the bulk liquid

3.3. Phase-field model for grain evolution

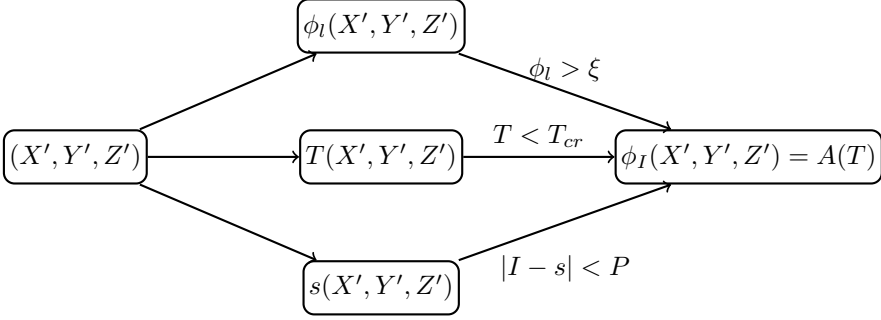


Figure 3.11.: Schematic diagram of the described nucleation algorithm.

phase $\xi = 1$, but also in the diffuse interface on the solidification front for $0 < \xi < 1$.

In the next step, at the permitted location (X', Y', Z') , the next integer I to $s(X', Y', Z')$ is determined and the difference of both is calculated. In the case of

$$|s(X', Y', Z') - I| \leq \frac{P}{2},$$

with the predefined parameter P , the corresponding grain with the phase-field I can nucleate. Thus, the magnitude of the parameter P determines the probability of the nucleation event. With increasing P , the probability of the grain genesis increases, too.

In the last step, the local temperature is proofed to be admissible for the nucleations $T(X, Y, Z) < T^{crit}$, and the corresponding phase-field value is set to the temperature-dependent nucleation amplitude value $\phi_I(X', Y', Z') = A(T)$.

Obviously, the formulated model interlinks with the main principles of the classical nucleation theory. The amplitude or the phase-field value of a new nucleus $\phi_I = A(T)$ in our model directly correlates with the critical radius $R_n(T)$ in the classical nucleation theory in 2-D, in the sense of the same volume fraction

$$R_n(T) = \sqrt{\frac{A(T)}{\pi}} \Delta x.$$

Since we only used constant values for the nucleation event probability P , it can also be a function of the temperature, temperature gradient and/or cooling rate. In addition, the nucleation rate in the classical text book nucleation theories can be related straightforwardly to the temporal periodicity of the described algorithm, see Figure 3.11.

3.3.8. Simulation results

In this section, some selected simulation results are shown, with the objective to highlight the potential of the presented phase-field model. In the computational performance, the nucleation model appears as a post condition, see Figure 3.11. In every time step, the phase-field equation (3.7) for all phase-field variables is solved with the discretization scheme in sec. 2.2. Subsequently, in the cells, in which the nucleation algorithm occurs, the phase-field variable for the liquid phase is corrected by the magnitude of the set, nucleated grain. Therefore, new grains emerge solely in the parental liquid phase. Note, that in case the liquid phase becomes smaller zero, by the application of the Gibbs simplex projection [76], all phase-field values have admissible magnitudes at the end of each temporal iteration.

By performing numerical experiments, different parameters are tested in the simulations. Because the constant nucleation amplitude is not natural, the temperature dependence is used. Several approaches exist to model this effect. In the following, the simple linear temperature dependence of the amplitude is defined in the temperature interval of [1760, 1820] to mimic both the nucleation for the temperature regime for $T \in [1760, 1780]$ and also the presented non-melted grains, which are presumably transported by the melt convection, but with smaller amplitude.

$$A(T) = \begin{cases} \bar{A}, & T \leq 1760 \\ \bar{A}\left(1 - \frac{T - 1760}{60}\right), & T \in [1760, 1820] \\ 0, & T \geq 1820 \end{cases} \quad (3.16)$$

In the simulation results shown in figure 3.12, the threshold is assumed to be $\xi = 0.4$, whereby the maximal amplitude value is $\bar{A} = 0.7$. In the considered three scenarios, the corresponding probability of the nucleation event is constant, but different.

Since in the scenario with the nucleation chance of 1%, left picture in Figure 3.12, no new nucleus does survive, the formation of new grains occurs by increasing the probability to 2.5%. A further increase of the probability to 5% results in the augmentation of the nucleated grains, in the enlargement of the nucleation band, but in the decreasing nucleated grain size.

As mentioned, the nucleation amplitude directly links to the critical radius; hence, it also correlates to the activation energy of the nucleation. Increasing the dependence of the activation energy on the temperature results in the flat amplitude. In Figure 3.13, three simulation results for a maximum amplitude of $\bar{A} = 0.3$ are shown. The threshold of the liquid phase remains the same, $\xi = 0.4$,

3.3. Phase-field model for grain evolution

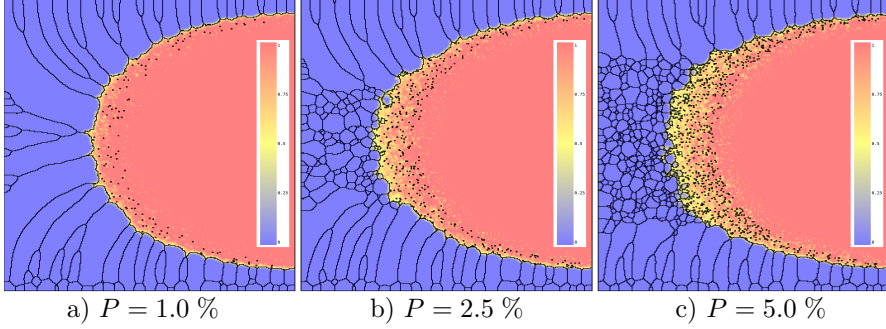


Figure 3.12.: The coloured field corresponds to the liquid distribution. The mesh signs the grain boundaries. The nucleation model parameters are: $\xi = 0.4$, $\bar{A} = 0.7$.

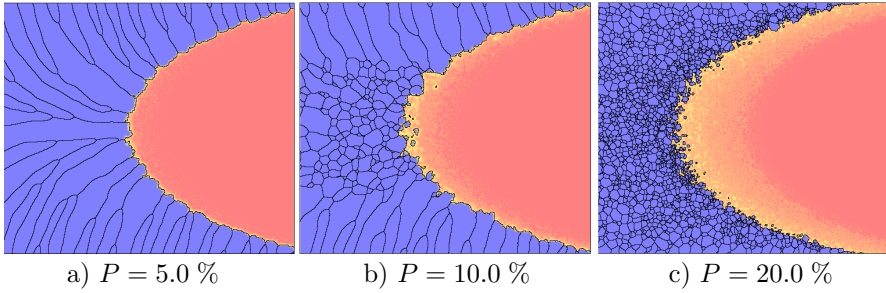


Figure 3.13.: The coloured field corresponds to the liquid distribution. The mesh signs the grain boundaries. The nucleation model parameters are: $\xi = 0.4$, $\bar{A} = 0.3$.

as in the previous case, Figure 3.12. The nucleation probabilities are 5%, 10% and 20%, respectively.

Remarkable is the dependency of the nucleation process on the temperature dependence of the nucleation amplitude. Since for the scenario with a sharp amplitude increase (lower activation energy) a new grain formation occurs for the probability of 5 %, Figure 3.12 on the right, no grain survives for a flatter amplitude increase (higher activation energy), Figure 3.13 on the left. In this simulation series, the observed correlations between the enlargement of the probability, the nucleation band width and the average nucleus size is confirmed.

Please note the mushy zone in the considered scenarios, marked by different casts

3. Grain Structure Evolution during Electron Beam Welding

of yellow. It spreads with growing probability and with growing amplitude. The width of the mushy zone is connected to the nucleation rate and also to the nucleated grain size.

In the next simulation scenarios, the influence of the threshold on the new grain formation is investigated. The amplitude changes with temperature, as in the scenario of Figure 3.13, also for higher activation energy with $\bar{A} = 0.3$. The probability of the nucleation event is 8%. Thus, simulations with two different threshold parameters are performed. Corresponding simulation results are shown in Figure 3.14.

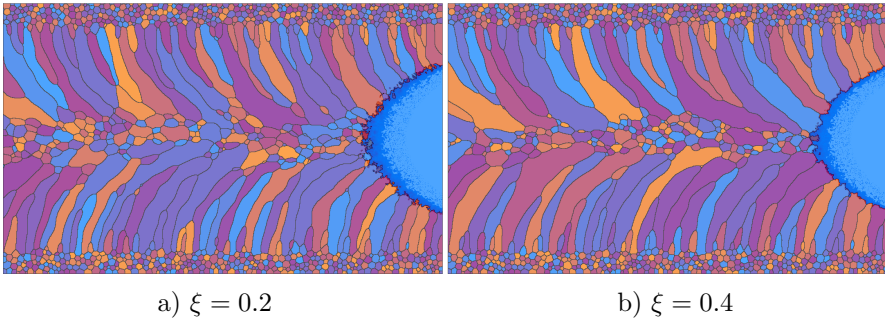


Figure 3.14.: Coloured domains represent different grains. The nucleation model parameters are: $P=8\%$, $\bar{A} = 0.3$.

Since all the simulations have the same grain contribution as the initial state, with differently applied simulation parameters in the nucleation model, various grains are dominating during the columnar growth, and every simulation ends with a unique morphology setup. The dark blue zone in the melt in Figure 3.14 signs the mushy zone, wherein the formation of new nuclei occurs. In both pictures, the mushy zones are comparable to each other in their shape. Nevertheless, with the same nucleation rate and with the same nucleation amplitude, the generation of new grains in the weld bath decreases with an increasing threshold.

The grain growth, Figures 3.12 a), 3.13 a) and 3.14, which follows the moving temperature gradient, coincides with the textbook theory [3], and also the globular nucleation at the vertex of the elliptical weld bath is explained by a maximal growth velocity and a lower temperature gradient [3, 4].

Analysing the solidification for the nucleation process, the generation of new grains in the mushy zone, marked as a red area in Figure 3.15 b), delays the solidification front propagation. Since the solid-liquid kinetic coefficient was

3.3. Phase-field model for grain evolution

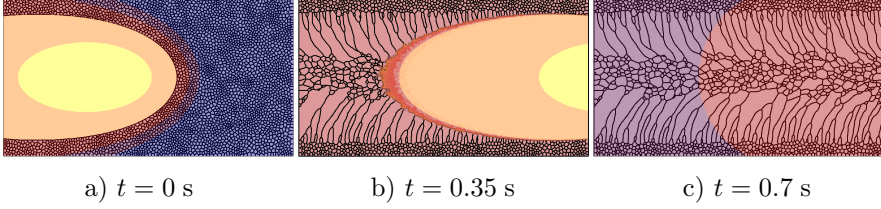


Figure 3.15.: The nucleation model parameters are: $P=9\%$, $\xi = 0.4$, $\bar{A} = 0.3$. The isotherms of the moving temperature field are represented by the coloured areas. The mesh signs the grain structure.

determined in such a manner that the maximum interfacial undercooling is of approximately 10 K, eq. (3.13), the growing grain front, represented by the black solid mesh between the grains and the mushy zone in Figure 3.15 b), undergoes the undercooling of approximately 50 K.

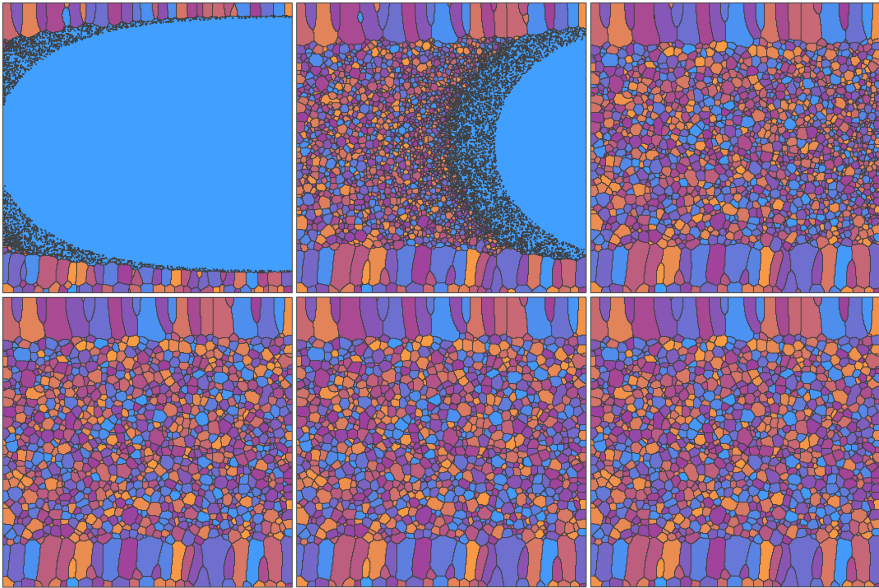


Figure 3.16.: Visualisation of the recrystallisation process in the post solidified weld seam in a temporal sequence of a simulation with the nucleation model parameters: $P=20\%$, $\xi = 0.35$, $\bar{A} = 0.3$.

For the visualisation of the grain coarsening, not only in the heat-affected zone, Figure 3.10, but also in the weld, a temporal sequence of a simulation is presented

3. Grain Structure Evolution during Electron Beam Welding

with the following parameters: $\xi = 0.35$, $P = 20\%$, $\bar{A} = 0.7$ in Figure 3.16. As the reader can see in Figure 3.16, the nucleation occurs with a high spatial rate, and the columnar grains from the direct weld periphery are hindered in their growth by the generated grains. The width of the nucleation band is almost the same as the weld width, and the short columnar grains are perpendicular to the weld direction. The nucleation algorithm with the chosen parameters produces a grain structure with many fine grains in the weld. But due to the temperature-dependent grain boundary mobility, the coarsening also takes places in the weld bath.

3.4. Conclusion

In summary, a simple, but efficient phase-field model for grain structure evolution during electron beam welding was presented. The highly complex manufacturing process of high-power welding was separated into the decoupled physical processes, whereby many physical processes were neglected. Based on the previous findings, the heat source was modelled using a well-established approach. By ignoring the melt flow in the weld bath and by using the same thermal constants in the transitional phases, an analytical temperature field distribution was derived. Unfortunately, the analytical solution is given as an indefinite integral and is impractical for the simulation of grain evolution during the welding process. This difficulty was removed by the usage of an approximative closed-form solution. An appropriate approach for a quantitative approximation was demonstrated.

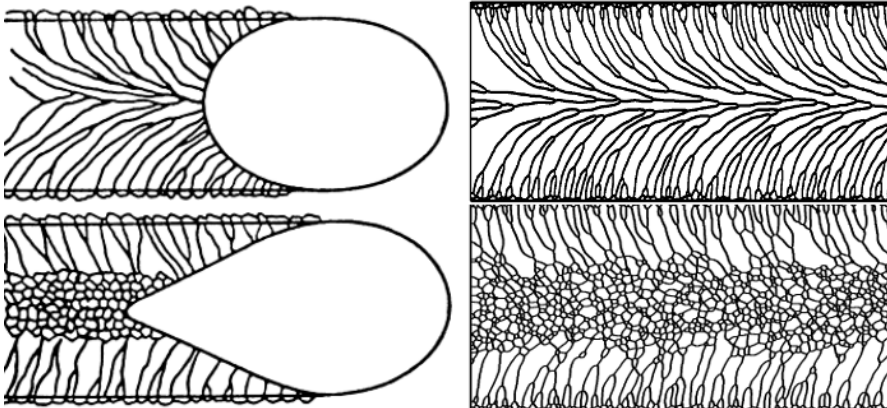


Figure 3.17.: Comparison between theoretical imagination from the existing text book theories [3, 4] on the left and simulation results on the right.

3.4. Conclusion

With a defined physical parameter, the kinetic coefficients were calibrated for both solid-melt boundary movement as well as for the temperature-dependent mobility during grain coarsening. With this approach, both the grain evolution in the heat-affected zone as well the grain growth in the post solidified weld have been successfully achieved. The recrystallisation process is controlled by the moving temperature field and slows down for decreasing temperatures.

A new model for the nucleation was formulated and implemented in PACE3D as post condition, which operates with the information about the local temperature and the presence of a parental melt. The demonstrated nucleation model links to the classical theory and offers a broad wealth of expansions and applications. Finally, the simulation results were presented for various variations of nucleation parameters. The grain morphologies in the virtual experiments correspond to the existing textbook theories, Figure 3.17. The important thing, though, is that the simulation results sign a qualitative match with the real experiments Figure 3.2 and Figures 3.12 c), 3.13 b) and c), as well as 3.14.

4. Phase-Field Models with Elasticity

4.1. Introduction

During the welding processes, and after the solidification, the phase transformation and thermal expansion generate residual stresses in the welded samples. I refer to [77], where the author states: ”*Postweld heat treatment is often a recommended practice for high-strength thick-section welded steels, where reduction of residual stresses developed as a result of welding is desired.*” Thus, these residual stresses cause the sample deformation, and it often leads to cracking in the heat-affected zone. In order to bridge this problem, the postweld heat treatment is required. Therefore, in the post solidified weld as well as in the heat-affected zone, the grain coarsening and/or the solid-solid state transformation in general are both driven not solely by the grain boundary energies, like in the previous chapter, but also by the diffusional and mechanical forces [78].

Different procedures are proposed for the incorporation of the elastic effects, as a basic deformation mode, into the phase-field model, and regardless of the real material process, as mentioned in sec. 2, one is endeavored to homogenise the bulk properties throughout the diffuse interface. Following the Voigt/Taylor (VT) homogenisation scheme [79], the strain ε is assumed to be a homogeneous state variable, and consequently the phase-dependent Cauchy¹ stresses σ^α are interpolated through the diffuse interface

$$\sigma = \sum_{\alpha=1}^N \sigma^\alpha h_\alpha.$$

Therefore, the interpolation of the strain energies, and the direct interpolation of stiffness [27, 28]

$$\mathcal{C}^{VT}(\phi) = \sum_{\alpha=1}^N \mathcal{C}^\alpha h_\alpha(\phi) \tag{4.1}$$

¹Baron Augustin-Louis Cauchy, 21.08.1789 – 23.05.1857, French mathematician, the founder of the complex analysis. He is the author of approximately eight hundred research articles. The lunar crater *Cauchy* is named after him.

4. Phase-Field Models with Elasticity

and eigenstresses $\sum_{\alpha=1}^N \mathcal{C}^\alpha \tilde{\varepsilon}^\alpha h_\alpha(\phi)$ is concluded. Alternatively, the Reuss/Sachs (RS) homogenisation approach [80] can be used [26]. The base assumption in the RS approach is the homogeneity of the stress in the diffuse interface. As a consequence, the calculation of the effective stiffness tensor follows the harmonic type

$$\mathcal{C}^{RS}(\phi) = \left(\sum_{\alpha=1}^N (\mathcal{C}^\alpha)^{-1} h_\alpha(\phi) \right)^{-1}.$$

Contrary to the interpolated eigenstresses in the VT approach, the phase-dependent eigenstrains in the Reuss/Sachs method are directly interpolated inside the diffuse interface

$$\tilde{\varepsilon}(\phi) = \sum_{\alpha=1}^N \tilde{\varepsilon}^\alpha h_\alpha(\phi). \quad (4.2)$$

The method, which was proposed by Khachaturyan in [81], is a mixture of both mentioned approaches and is widely used in the phase-field community, e.g. [25]. The interpolated stiffness is calculated due to the VT homogenisation scheme, eq. (4.1), but the eigenstrains are calculated due to the RS approach, eq. (4.2). Another combination of the VT and RS interpolation schemes is proposed in [29] in order to calculate the elastic driving forces and the stress tensor.

By the usage of the homogeneous variables, which are inconsistent to the thermodynamic and mechanical equilibrium conditions, none of the mentioned methods would resolve the elastic fields quantitatively. The relevant mismatch between the analytical and numerical results reveals the incompleteness of the models [29, 30]. Hence, the frivolous modeling and the consequential interpolation of the inconsistent quantities in the diffuse interface produces spurious interfacial energetics in the diffuse interface, which scales with a widened interface layer, as shown in [29, 30]; for comparison see also eq. (2.14) for the inconsistent chemical model in sec. 2.1.1.

Inter alia, this is also the reason why the diffuse interface width W is usually selected much smaller than the local curvature κ , so that $\kappa W \ll 1$. Such a severe restriction on the diffuse interface limits the numerical simulations of the real manufacturing processes, which contradicts the main objective of the usage of the phase-field model. In principle, one should be able to artificially widen the diffuse interface width, while still capturing the real physics. Thus, for the quantitative numerical results, but in the presence of the distorted interfacial physics, the use of the simulation parameters for a special physical setup is cumbersome; see also the exemplary description for the chemical system in [49].

In our recent work [30], we also investigate the reasons for the interfacial excess energies in the mentioned models by the underlying different homogenisation

assumption and the resulting interpolation schemes of the material constants in the diffuse interface. Furthermore, we show that assuming either the total strain or the whole stress to be the homogeneous variables in the corresponding elastic models, the mechanical jump conditions at the interface are only partially satisfied, whereby the homogeneous normal stress and tangential strain are consistent with the vanishing traction force and with the Hadamard jump condition, respectively. In contrast to the homogeneous variables, the tangential stress and the normal strain are inhomogeneous variables with a discontinuity at the common interface. The previous consideration with homogeneous and inhomogeneous strains and stresses is similar to the condition of the same chemical potential and different concentrations in the solid and liquid phases in alloys. Since at the common interface the compositions of two neighbouring phases differ from each other in the quantitative phase-field modeling, the free energy will be given as an interpolation of phase-corresponding free energies, each evaluated with self-contained concentration [43].

Therefore, inspired by the philosophy of the chemical model in [43], see sec. 2.1.1, we propose an alternative homogenisation approach for the elastic constants and for the eigenstrain/eigenstress in [30], purely based on the mechanical jump conditions acting on the coherent interface. Since the strain energies are functions of the strain tensor, the interpolation of elastic energy throughout the diffuse interface should be done with phase-corresponding strain energies, evaluated with phase-corresponding strains. Consequently, the homogenised strain energy in the diffuse interface should be consistent with the homogeneous variables and with jumps in the inhomogeneous variables. The model is also presented in the next section. The validation of the derived model is performed for 1-D test cases as well as for a circular inclusion [30]. In the investigated scenarios, we get an excellent agreement between the theoretical sharp interface predictions and the simulation results.

Nevertheless, the detailed verification of the elliptical Eshelby inclusion reveals the incompleteness of the presented model, see chapter 5. Since both the usage of the interfacial homogeneous variables and the stress calculation in the diffuse interface correspond to the mechanical jump conditions at the coherent interface, the derivation of the elastic driving force for the solid-solid phase transformation is not consistent with the variational approach. In the next paragraph, the main principles of our recent model [30] are presented in this thesis to highlight the remaining drawbacks of the model.

In order to eliminate the mentioned defects, an alternative formalism is used and is presented in sec. 4.4. The new formulation of the stress tensor and of the elastic driving force is thermodynamically consistent and is verified in the two-dimensional scenarios, for which the theoretical solutions are known in a closed form. Furthermore, the new formulation of the interfacial elastic fields

4. Phase-Field Models with Elasticity

allows to reduce the computational time significantly, in comparison with the formulation in [30]. Moreover, a further computational benefit is achieved in the simulations, in which elastic isotropic materials are used, see appendix C .

4.2. Mechanical jump conditions at a coherent interface

The reader should be familiar with the main definitions in continuum mechanics and in linear elasticity theory. In the following, the capital letters sign the tensorial notation of the strain tensor \mathbf{E} and the Cauchy stress tensor $\mathbf{\Sigma}$. The small letters $\boldsymbol{\varepsilon}$ and $\boldsymbol{\sigma}$ are their respective representations in the Voigt notation.

The jump of the elastic potential at the common coherent interface, between two neighbouring phases, drives the solid-solid phase transformation [82]. Following the main principles of continuum mechanics, the strain tensor \mathbf{E} is given by the symmetrised displacement gradient $\nabla \mathbf{u}$

$$\mathbf{E} = \frac{1}{2}(\nabla \mathbf{u} + \nabla \mathbf{u}^T). \quad (4.3)$$

Since the displacement vector is spatially continuous, the strain tensor evinces a jump through an interface between two solid phases. Under the assumption of the coherent interface, the Hadamard jump condition reduces the strain jump to the jump in the normal strain vector $(\mathbf{E}^\alpha - \mathbf{E}^\beta)\mathbf{n} \neq \mathbf{0}$, so that the tangential strain vectors match

$$\mathbf{E}^\alpha \mathbf{t} = \mathbf{E}^\beta \mathbf{t}, \quad (4.4)$$

with \mathbf{n} as the normal vector of the interface and \mathbf{t} as any vector perpendicular to \mathbf{n} . The continuity in the tangential strain also implies no slip boundary conditions between the neighbouring phases.

A homogeneity of the traction vector

$$\mathbf{\Sigma}^\alpha \mathbf{n} = \mathbf{\Sigma}^\beta \mathbf{n} \quad (4.5)$$

at the interface yields the continuous normal stress vectors.

In the following, a short overview over our recent model in [30] is presented. For completeness, the relevant details of the model are listed in the next paragraphs, but an interested reader is referred to the original manuscript. Since the aim of this part of the thesis is to highlight the defects of the model, the detailed overview can be skipped, and the reader can directly jump to sec. 4.3.7.

4.3. Short overview over the model by Schneider et al.

4.3.1. The concept of the model

In our recent work [30], we try to derive a thermodynamically and mechanically consistent formulation of the interfacial Cauchy stress and the elastic driving force. Since we are using the principle of small deformations, the strain as well as the stress tensors are symmetric matrices, and, for simplicity, we use the Voigt notation of the strain and stress. The following derivation steps are applied in our analysis.

Based on the mechanical jump conditions, eq. (4.4) and eq. (4.5), the homogeneous variables are the tangential strain and the normal stress vectors. Doing so, we use the coordinate transformation to rewrite the Voigt strain and stress vectors in the local coordinate system, sec. 4.3.2. By using Hooke's law, we express inhomogeneous variables, normal strain and tangential stress vectors in sec. 4.3.3, in dependence on the homogeneous variables and rewrite the elastic energies in terms of homogeneous variables in sec. 4.3.4. Then, applying the interpolation of the inhomogeneous variables in the interface, we derive the expression for the normal stress in dependence on the total strain in sec. 4.3.5. Substituting the expression for the normal stress into the interpolated elastic energy in the diffuse interface, we get the elastic driving force by taking the derivative with respect to the phase-field variable in sec. 4.3.6.

4.3.2. Coordinate transformation

By rewriting both tensors with respect to the coordinate transformation from a reference coordinate system (in the following Cartesian², which is given with the standard base $E = \{\mathbf{e}_1, \mathbf{e}_2, \mathbf{e}_3\}$) to a local coordinate system, which is given by the interface orientation and the perpendicular tangential vectors $B = \{\mathbf{n}, \mathbf{t}, \mathbf{s}\}$, we get

$$\mathbf{E}_B = \mathbf{Q}\mathbf{E}_E\mathbf{Q}^T \quad \text{and} \quad \boldsymbol{\Sigma}_B = \mathbf{Q}\boldsymbol{\Sigma}_E\mathbf{Q}^T, \quad (4.6)$$

with

$$\mathbf{Q} = \begin{pmatrix} n_1 & n_2 & n_3 \\ t_1 & t_2 & t_3 \\ s_1 & s_2 & s_3 \end{pmatrix}.$$

²René Descartes, 31.03.1596 – 11.02.1650. French philosopher, mathematician and scientist. Until now, we have used his convention in equations with a , b and c for the knowns and x , y and z for the unknowns.

4. Phase-Field Models with Elasticity

With the symmetry in the strain tensors $\mathbf{E}_{ij} = \mathbf{E}_{ji}$ and stress tensors $\Sigma_{ij} = \Sigma_{ij}$, we use the usual Voigt notation to write the Voigt strain and stress vectors in a Cartesian coordinate system

$$\begin{aligned}\boldsymbol{\varepsilon}_E^T &= (\boldsymbol{\varepsilon}_1, \boldsymbol{\varepsilon}_2, \boldsymbol{\varepsilon}_3, \boldsymbol{\varepsilon}_4, \boldsymbol{\varepsilon}_5, \boldsymbol{\varepsilon}_6) = (\mathbf{E}_{11}, \mathbf{E}_{22}, \mathbf{E}_{33}, 2\mathbf{E}_{23}, 2\mathbf{E}_{13}, 2\mathbf{E}_{12}) \\ \boldsymbol{\sigma}_E^T &= (\sigma_1, \sigma_2, \sigma_3, \sigma_4, \sigma_5, \sigma_6) = (\Sigma_{11}, \Sigma_{22}, \Sigma_{33}, \Sigma_{23}, \Sigma_{13}, \Sigma_{12}).\end{aligned}$$

The modified Voigt notation for the Voigt vectors in the local coordinate system, due to the base B , are reordered with respect to the normal and tangential parts

$$\begin{aligned}\boldsymbol{\varepsilon}_B &= \underbrace{(\mathbf{E}_{nn}, 2\mathbf{E}_{nt}, 2\mathbf{E}_{ns})}_{\boldsymbol{\varepsilon}_n}, \underbrace{(\mathbf{E}_{tt}, \mathbf{E}_{ss}, 2\mathbf{E}_{ts})}_{\boldsymbol{\varepsilon}_t}^T, \\ \boldsymbol{\sigma}_B &= \underbrace{(\Sigma_{nn}, \Sigma_{nt}, \Sigma_{ns})}_{\boldsymbol{\sigma}_n}, \underbrace{(\Sigma_{tt}, \Sigma_{ss}, \Sigma_{ts})}_{\boldsymbol{\sigma}_t}^T.\end{aligned}$$

The coordinate transformation in eq. (4.6) is therefore given by the matrix vector products

$$\boldsymbol{\varepsilon}_B = \mathbf{M}_\boldsymbol{\varepsilon} \boldsymbol{\varepsilon}_E \quad \text{and} \quad \boldsymbol{\sigma}_B = \mathbf{M}_\boldsymbol{\sigma} \boldsymbol{\sigma}_E,$$

with the matrices

$$\mathbf{M}_\boldsymbol{\varepsilon} = \begin{pmatrix} n_1^2 & n_2^2 & n_3^2 & n_2n_3 & n_1n_3 & n_1n_2 \\ 2n_1t_1 & 2n_2t_2 & 2n_3t_3 & n_2t_3 + n_3t_2 & n_1t_3 + n_3t_1 & n_1t_2 + n_2t_1 \\ 2n_1s_1 & 2n_2s_2 & 2n_3s_3 & n_2s_3 + n_3s_2 & n_1s_3 + n_3s_1 & n_1s_2 + n_2s_1 \\ t_1^2 & t_2^2 & t_3^2 & t_2t_3 & t_1t_3 & t_1t_2 \\ s_1^2 & s_2^2 & s_3^2 & s_2s_3 & s_1s_3 & s_1s_2 \\ 2t_1s_1 & 2t_2s_2 & 2t_3s_3 & t_2s_3 + t_3s_2 & t_1s_3 + t_3s_1 & t_1s_2 + t_2s_1 \end{pmatrix}$$

and

$$\mathbf{M}_\boldsymbol{\sigma} = \begin{pmatrix} n_1^2 & n_2^2 & n_3^2 & 2n_2n_3 & 2n_1n_3 & 2n_1n_2 \\ n_1t_1 & n_2t_2 & n_3t_3 & n_2t_3 + n_3t_2 & n_1t_3 + n_3t_1 & n_1t_2 + n_2t_1 \\ n_1s_1 & n_2s_2 & n_3s_3 & n_2s_3 + n_3s_2 & n_1s_3 + n_3s_1 & n_1s_2 + n_2s_1 \\ t_1^2 & t_2^2 & t_3^2 & 2t_2t_3 & 2t_1t_3 & 2t_1t_2 \\ s_1^2 & s_2^2 & s_3^2 & 2s_2s_3 & 2s_1s_3 & 2s_1s_2 \\ t_1s_1 & t_2s_2 & t_3s_3 & t_2s_3 + t_3s_2 & t_1s_3 + t_3s_1 & t_1s_2 + t_2s_1 \end{pmatrix}, \quad (4.7)$$

respectively. Note that the different transformation matrices $\mathbf{M}_\boldsymbol{\sigma} \neq \mathbf{M}_\boldsymbol{\varepsilon}$ result from different treatments of the shear vector components in the Voigt notation, but they are related by $\mathbf{M}_\boldsymbol{\sigma}^T = \mathbf{M}_\boldsymbol{\varepsilon}^{-1}$ as an immediate consequence of the invariance of the elastic energy under the coordinate transformation.

Moreover, the previous mechanical jump conditions, eq. (4.4) and eq. (4.5), are equivalent to

$$\boldsymbol{\varepsilon}_t^\alpha = \boldsymbol{\varepsilon}_t^\beta \quad \text{and} \quad \boldsymbol{\sigma}_n^\alpha = \boldsymbol{\sigma}_n^\beta.$$

4.3.3. Inhomogeneous variables

The normal strain vectors ε_n^α and ε_n^β as well as the tangential stress vectors σ_t^α and σ_t^β are basically not the same and are the interfacial inhomogeneous variables.

Using the assumption of the linear elastic materials, the stress and strain vectors in the bulk phase are related by Hooke's law

$$\boldsymbol{\sigma} = \mathbf{C}(\boldsymbol{\varepsilon} - \tilde{\boldsymbol{\varepsilon}}), \quad (4.8)$$

whereby $\mathbf{C} \in \mathbb{R}^{6 \times 6}$ is the symmetric stiffness matrix, and $\tilde{\boldsymbol{\varepsilon}}$ is the total non-elastic strain. $\tilde{\boldsymbol{\varepsilon}}$ can either be a constant eigenstrain, an eigenstrain, dependent on the temperature, due to the thermal expansion, a plastic strain, or even the sum of different non-elastic strain contributions.

Thus, by using the Voigt strain and stress vectors in the local coordinate system, we get the Voigt stress vector, written as

$$\boldsymbol{\sigma}_B = \underbrace{\mathbf{M}_\sigma \mathbf{C}_E \mathbf{M}_\sigma^T}_{\mathbf{C}_B} (\boldsymbol{\varepsilon}_B - \tilde{\boldsymbol{\varepsilon}}_B)$$

or, rewritten with respect to the normal and tangential parts, as

$$\begin{pmatrix} \boldsymbol{\sigma}_n \\ \boldsymbol{\sigma}_t \end{pmatrix} = \begin{pmatrix} \mathbf{C}_{nn} & \mathbf{C}_{nt} \\ \mathbf{C}_{tn} & \mathbf{C}_{tt} \end{pmatrix} \left(\begin{pmatrix} \boldsymbol{\varepsilon}_n \\ \boldsymbol{\varepsilon}_t \end{pmatrix} - \begin{pmatrix} \tilde{\boldsymbol{\varepsilon}}_n \\ \tilde{\boldsymbol{\varepsilon}}_t \end{pmatrix} \right). \quad (4.9)$$

Here, the difference between the stiffness tensors \mathbf{C}_E and \mathbf{C}_B is self-explanatory. In the previous equation (4.9), we separated the stiffness tensor into four 3×3 blocks and, correspondingly, signed them with the indices to the appropriate strain and stress parts. Doing so, we are now allowed to derive the inhomogeneous quantities in dependence of the homogeneous normal stress and tangential strain vectors. After some elementary reformulations, we can write the following for the interfacial inhomogeneous variables

$$\begin{aligned} \boldsymbol{\varepsilon}_n^i &= (\mathbf{C}_{nn}^i)^{-1} \left(\boldsymbol{\sigma}_n - \mathbf{C}_{nt}^i (\boldsymbol{\varepsilon}_t - \tilde{\boldsymbol{\varepsilon}}_t^i) \right) + \tilde{\boldsymbol{\varepsilon}}_n^i \\ \boldsymbol{\sigma}_t^i &= \mathbf{C}_{tn}^i (\mathbf{C}_{nn}^i)^{-1} \boldsymbol{\sigma}_n + \left(\mathbf{C}_{tt}^i - \mathbf{C}_{tn}^i (\mathbf{C}_{nn}^i)^{-1} \mathbf{C}_{nt}^i \right) (\boldsymbol{\varepsilon}_t - \tilde{\boldsymbol{\varepsilon}}_t^i), \end{aligned} \quad (4.10)$$

with $i = \alpha, \beta$.

4.3.4. Elastic energy in the diffuse interface

Since the previous derivation is taken for two phases in the sharp interface description, we use the same homogeneous and inhomogeneous variables in the

4. Phase-Field Models with Elasticity

diffuse interface approach. Therefore, the elastic energy in the diffuse interface

$$f_{el}(\boldsymbol{\varepsilon}, \phi, \nabla\phi) = f_{el}^\alpha(\boldsymbol{\varepsilon}_n^\alpha, \boldsymbol{\varepsilon}_t)h_\alpha + f_{el}^\beta(\boldsymbol{\varepsilon}_n^\beta, \boldsymbol{\varepsilon}_t)h_\beta \quad (4.11)$$

is given by the interpolation of the phase-dependent strain energies

$$f^i(\boldsymbol{\varepsilon}_n^i, \boldsymbol{\varepsilon}_t) = \frac{1}{2} \left(\langle \boldsymbol{\varepsilon}_n^i - \tilde{\boldsymbol{\varepsilon}}_n^i, \mathbf{C}_{nn}^i(\boldsymbol{\varepsilon}_n^i - \tilde{\boldsymbol{\varepsilon}}_n^i) \rangle + \langle \boldsymbol{\varepsilon}_n^i - \tilde{\boldsymbol{\varepsilon}}_n^i, \mathbf{C}_{nt}^i(\boldsymbol{\varepsilon}_t - \tilde{\boldsymbol{\varepsilon}}_t^i) \rangle + \langle \boldsymbol{\varepsilon}_t - \tilde{\boldsymbol{\varepsilon}}_t^i, \mathbf{C}_{tn}^i(\boldsymbol{\varepsilon}_n^i - \tilde{\boldsymbol{\varepsilon}}_n^i) \rangle + \langle \boldsymbol{\varepsilon}_t - \tilde{\boldsymbol{\varepsilon}}_t^i, \mathbf{C}_{tt}^i(\boldsymbol{\varepsilon}_t - \tilde{\boldsymbol{\varepsilon}}_t^i) \rangle \right),$$

with $i = \alpha, \beta$, whereby the phase-dependent strain energies depend on phase-dependent strains $\boldsymbol{\varepsilon}^\alpha \neq \boldsymbol{\varepsilon}^\beta$.

4.3.5. Cauchy stress in the diffuse interface

To derive the Cauchy stress in the diffuse interface, the inhomogeneous total normal strain and the tangential stress are used as interpolated quantities, which write as

$$\boldsymbol{\varepsilon}_n = \boldsymbol{\varepsilon}_n^\alpha h_\alpha + \boldsymbol{\varepsilon}_n^\beta h_\beta \quad \text{and} \quad \boldsymbol{\sigma}_t = \boldsymbol{\sigma}_t^\alpha h_\alpha + \boldsymbol{\sigma}_t^\beta h_\beta,$$

respectively. Hence, the substitution of the right-hand side of the phase-dependent normal strain vectors from eq. (4.10) into the interpolated normal strain vector results in

$$\boldsymbol{\varepsilon}_n = \mathbf{T}_{nn}\boldsymbol{\sigma}_n - \mathbf{T}_{nt}\boldsymbol{\varepsilon}_t + (\mathbf{T}_{nt}^\alpha \tilde{\boldsymbol{\varepsilon}}_t^\alpha + \tilde{\boldsymbol{\varepsilon}}_n^\alpha)h_\alpha + (\mathbf{T}_{nt}^\beta \tilde{\boldsymbol{\varepsilon}}_t^\beta + \tilde{\boldsymbol{\varepsilon}}_n^\beta)h_\beta, \quad (4.12)$$

with a shorthand notation

$$\begin{aligned} \mathbf{T}_{nn} &= (\mathbf{C}_{nn}^\alpha)^{-1}h_\alpha + (\mathbf{C}_{nn}^\beta)^{-1}h_\beta, \\ \mathbf{T}_{nt} &= \mathbf{T}_{nt}^\alpha h_\alpha + \mathbf{T}_{nt}^\beta h_\beta \quad \text{with} \quad \mathbf{T}_{nt}^i = (\mathbf{C}_{nn}^i)^{-1}\mathbf{C}_{nt}^i, \quad i = \alpha, \beta \end{aligned}$$

The inversion of the previous equation allows to write the following expression for the normal stress vector

$$\boldsymbol{\sigma}_n(\boldsymbol{\varepsilon}_B) = \mathbf{T}_{nn}^{-1} \left((\boldsymbol{\varepsilon}_n - \tilde{\boldsymbol{\varepsilon}}_n) + \mathbf{T}_{nt}^\alpha (\tilde{\boldsymbol{\varepsilon}}_t - \tilde{\boldsymbol{\varepsilon}}_t^\alpha)h_\alpha + \mathbf{T}_{nt}^\beta (\tilde{\boldsymbol{\varepsilon}}_t - \tilde{\boldsymbol{\varepsilon}}_t^\beta)h_\beta \right). \quad (4.13)$$

The incorporation of the normal stress vector into the interpolated tangential stress vectors uses the shorthand notation of

$$\mathbf{T}_{tt}^i = \mathbf{C}_{tn}^i + \mathbf{C}_{tn}(\mathbf{C}_{nn}^i)^{-1}\mathbf{C}_{nt}$$

and

$$\mathbf{T}_{tt} = \mathbf{T}_{tt}^\alpha h_\alpha + \mathbf{T}_{tt}^\beta h_\beta,$$

4.3. Short overview over the model by Schneider et al.

and then, by combining the formulas, the Voigt stress vector in base B writes as

$$\begin{pmatrix} \boldsymbol{\sigma}_n \\ \boldsymbol{\sigma}_t \end{pmatrix} = \begin{pmatrix} \mathbf{T}_{nn}^{-1} & \mathbf{T}_{nn}^{-1}\mathbf{T}_{nt} \\ \mathbf{T}_{tn}\mathbf{T}_{nn}^{-1} & \mathbf{T}_{tt} + \mathbf{T}_{tn}\mathbf{T}_{nn}^{-1}\mathbf{T}_{nt} \end{pmatrix} \begin{pmatrix} \begin{pmatrix} \boldsymbol{\varepsilon}_n \\ \boldsymbol{\varepsilon}_t \end{pmatrix} \\ - \begin{pmatrix} \tilde{\boldsymbol{\varepsilon}}_n \\ \tilde{\boldsymbol{\varepsilon}}_t \end{pmatrix} \end{pmatrix}, \quad (4.14)$$

with the interfacial effective eigenstrain $\tilde{\boldsymbol{\varepsilon}} = (\tilde{\boldsymbol{\varepsilon}}_n, \tilde{\boldsymbol{\varepsilon}}_t)$.

Finally, in order to write the Voigt stress vector in reference (Cartesian) coordinates, the derived stress vector in base B is multiplied with the transformation matrix \mathbf{M}_ε^T

$$\boldsymbol{\sigma}_E = \mathbf{M}_\varepsilon^T \boldsymbol{\sigma}_B. \quad (4.15)$$

4.3.6. Elastic driving force for solid-solid phase transformation

In the determination of the elastic driving force, which is basically given as a variational derivative

$$\frac{\delta f_{el}}{\delta \phi_\alpha} = \left(\frac{\partial}{\partial \phi_\alpha} - \nabla \cdot \frac{\partial}{\partial \nabla \phi_\alpha} \right) f_{el} \approx \frac{\partial f_{el}}{\partial \phi_\alpha}$$

of the interfacial elastic energy, we used the assumption of the constant strain along the curved interface, and thus neglected the divergence term with the derivative, with respect to the phase-field gradient. Therefore, the elastic driving force writes as

$$\begin{aligned} \partial_{\phi_\alpha} f_{el} = & \frac{1}{2} \left((\langle \boldsymbol{\varepsilon}_t - \tilde{\boldsymbol{\varepsilon}}_t^\alpha, \boldsymbol{\sigma}_t^\alpha \rangle - \langle \boldsymbol{\varepsilon}_n^\alpha - \tilde{\boldsymbol{\varepsilon}}_n^\alpha, \boldsymbol{\sigma}_n \rangle) \partial_{\phi_\alpha} h_\alpha + \right. \\ & \left. + (\langle \boldsymbol{\varepsilon}_t - \tilde{\boldsymbol{\varepsilon}}_t^\beta, \boldsymbol{\sigma}_t^\beta \rangle - \langle \boldsymbol{\varepsilon}_n^\beta - \tilde{\boldsymbol{\varepsilon}}_n^\beta, \boldsymbol{\sigma}_n \rangle) \partial_{\phi_\alpha} h_\beta \right). \end{aligned}$$

A similar formula can also be found in [27].

The previous formulation of elastic energy in eq. (4.11) was inspired by the chemical model in [43]. In their work, the authors derived a thermodynamically consistent phase-field model to describe isothermal solidification of binary alloys, which is driven by the diffusional process. In the chemical system, two neighbouring phases at equilibrium have different compositions which are not arbitrary, but are due to the same chemical potential. Even in the elastic system, the inhomogeneous variables are chosen in such a manner that the mechanical jump conditions, which are expressed in homogeneous variables, match. Therefore, the normal strain and tangential stresses are inhomogeneous, and the normal stress and tangential strain are homogeneous variables, respectively.

4.3.7. Some drawbacks of the model by Schneider et al.

In the mentioned work [30], for which the sketched model was presented in the previous paragraph, the verification was performed on some trivial test cases. One-dimensional simulation results for serial and parallel chains show excellent agreement with the theoretical predictions and confirm the model for one-dimensional problems. In the two-dimensional test case, we used a circular inclusion in a matrix and considered the equilibrium state. In this testing scenario, the capillary force counterbalances the elastic driving force, so that the desired equilibrium state is metastable. Therefore, it was not possible to get a final state, but we should implicitly estimate the result.

One of the mathematical drawbacks is the fact that the whole formalism depends on the used local span vectors \mathbf{t} and \mathbf{s} of the tangential plane, which are perpendicular to the normal vector \mathbf{n} , whereby the interface orientation, which is determined by \mathbf{n} , should solely be sufficient.

Throughout the demonstrated procedure, sec. 4.3.2-4.3.6, many precalculations are required to obtain the Cauchy stress and the elastic driving force. In total, a bulky concept with an inconvenient calculation of the effective stiffness tensor and of the effective eigenstrain in the diffuse interface requires several tensor inversions and tensor products. The theoretical derivations form the base for the numerical implementation, and the calculative performance is highly inefficient.

A main defect of the presented model is its quantitative limitation solely to the test cases, in which the interfacial strain is constant. Because of the neglect of the derivative, with respect to the phase-field gradient, the model is inconsistent with the variational principle and is therefore incomplete.

The endeavour to remove the errors in the presented analysis was unrewarded by success. Consequently, in order to correct the mentioned drawbacks, a renewed formulation will be derived starting at the mechanical jump conditions in sec. 4.2.

4.4. A new formulation of the elastic energy and the consequential fields

4.4.1. Decomposition of the stress and strain tensors into the homogeneous and inhomogeneous constituents

The main difference between the next derivation and the previous model in sec. 4.3 is the extraction of the homogeneous variables from the total strain and Cauchy stress tensors. Alternatively to the component-wise separation, in sec. 4.3.2, I suggest an alternative concept. Thus, by using the normal \mathbf{n} , I use the projection tensor

$$\Phi = \mathbf{n} \otimes \mathbf{n},$$

which is given as a dyadic product of the interfacial normal. The complementary disjunct projection on the perpendicular subspace is given by

$$\mathbf{1} - \Phi,$$

with the unity matrix $\mathbf{1} \in \mathbb{R}^{3 \times 3}$. Both projections image all vectors on the linear subspace spanned by \mathbf{n} and on the corresponding tangential plane, respectively.

In the next step, the following matrices are defined

$$\Sigma_n = \Phi \Sigma + \Sigma \Phi - \Phi \Sigma \Phi, \quad (4.16)$$

$$\Sigma_t = (\mathbf{1} - \Phi) \Sigma (\mathbf{1} - \Phi), \quad (4.17)$$

for the Cauchy stress tensor Σ and similarly for the strain tensor \mathbf{E} in eq. (4.3), with the notation \mathbf{E}_n and \mathbf{E}_t , respectively. Obviously, the defined tensors Σ_n , Σ_t and \mathbf{E}_n , \mathbf{E}_t are symmetric and give the original matrices

$$\Sigma = \Sigma_n + \Sigma_t \quad \text{and} \quad \mathbf{E} = \mathbf{E}_n + \mathbf{E}_t$$

in the sum. This kind of decomposition of the original strain and stress tensors Σ_n and \mathbf{E}_n in their normal and tangential constituents is more advantageous in contrast to the corresponding step in the previous analysis in sec. 4.3.2. In the preceding model, the dissection of the stress and strain was performed after the change in the coordinate system; hence, the formulation required the formulation of all base vectors. In the new proposal, the respective normal and tangential constituents of the strain or stress tensors remain in the original coordinate systems and solely depend on the normal vector.

4. Phase-Field Models with Elasticity

Moreover, the multiplication of the normal \mathbf{n} or of any tangential vector \mathbf{t} with the stress tensors is equivalent to the multiplications with the corresponding respective normal and tangential parts

$$\boldsymbol{\Sigma}\mathbf{n} = \boldsymbol{\Sigma}_n\mathbf{n}, \quad \boldsymbol{\Sigma}\mathbf{t} = \boldsymbol{\Sigma}_t\mathbf{t},$$

as $\boldsymbol{\Sigma}_n\mathbf{t} = \boldsymbol{\Sigma}_t\mathbf{n} = \mathbf{0}$. The same equalities are also true for the vector matrix products with the strain tensor and with its constituents.

In the next step, I use Hooke's law without eigenstrain, $\tilde{\mathbf{E}} = \mathbf{0}$, in order to recapitulate the tensorial notation; thus, the stress components are given as

$$\Sigma_{ij} = \sum_{k=1}^3 \sum_{l=1}^3 \mathcal{C}_{ijkl} \mathbf{E}_{kl},$$

with the symmetric fourth-rank stiffness tensor $\mathcal{C} \in \mathbb{R}^{3 \times 3 \times 3 \times 3}$ [83, 84], or written in the tensor notation as

$$\boldsymbol{\Sigma} = \mathcal{C} : \mathbf{E}.$$

Note that the multiplication of two fourth-rank tensors, $\mathcal{A}, \mathcal{B} \in \mathbb{R}^{3 \times 3 \times 3 \times 3}$, as $\mathcal{A} : \mathcal{B}$, is a fourth-rank tensor $\mathcal{D} \in \mathbb{R}^{3 \times 3 \times 3 \times 3}$, with the components

$$\mathcal{D}_{ijkl} = \sum_{m=1}^3 \sum_{n=1}^3 \mathcal{A}_{ijmn} \mathcal{B}_{mnkl}.$$

Both decompositions of the Cauchy stress tensor in eq. (4.16) and in eq.(4.17) could also be expressed as a tensor product, with the fourth-rank tensors \mathcal{N} and \mathcal{T} defined as

$$\mathcal{N} = \mathbf{1} \square \Phi + \Phi \square \mathbf{1} - \Phi \square \Phi, \quad \text{and} \quad \mathcal{T} = (\mathbf{1} - \Phi) \square (\mathbf{1} - \Phi),$$

whereby the explicit determination of the components in \mathcal{N} and \mathcal{T} is in correspondence with the definition of the fourth-rank tensor $\mathcal{D} = \mathbf{A} \square \mathbf{B}$, with the components

$$\mathcal{D}_{ijkl} = A_{ik} B_{jl}.$$

In this sense, the predefined fourth-rank tensors \mathcal{N} and \mathcal{T} are symmetric,

$$\mathcal{N}_{ijkl} = \mathcal{N}_{klij} \quad \text{and} \quad \mathcal{T}_{ijkl} = \mathcal{T}_{klij}, \quad (4.18)$$

and are the fourth-rank projection tensors for the corresponding subspaces. This is because of their idempotence:

$$\mathcal{N} : \mathcal{N} = \mathcal{N}, \quad \text{and} \quad \mathcal{T} : \mathcal{T} = \mathcal{T}.$$

4.4. A new formulation of the elastic energy and the consequential fields

Special properties of both tensors, on the one hand, are their orthogonality to each other,

$$\mathcal{T} : \mathcal{N} = \mathcal{O} = \mathcal{N} : \mathcal{T},$$

with the zero tensor \mathcal{O} and, on the other hand, their additive span of the identity tensor

$$\mathcal{N} + \mathcal{T} = \mathcal{I},$$

which is defined as $\mathcal{I} = \mathbf{1} \square \mathbf{1} \in \mathbb{R}^{3 \times 3 \times 3 \times 3}$.

The essential reason for the formulation of the projective fourth-rank tensors \mathcal{N} and \mathcal{T} is the alternative expression of the normal and tangential stress and strain constituents as

$$\begin{aligned} \boldsymbol{\Sigma}_n &= \mathcal{N} : \boldsymbol{\Sigma} \quad \text{and} \quad \boldsymbol{\Sigma}_t = \mathcal{T} : \boldsymbol{\Sigma}, \\ \mathbf{E}_n &= \mathcal{N} : \mathbf{E} \quad \text{and} \quad \mathbf{E}_t = \mathcal{T} : \mathbf{E}. \end{aligned}$$

For convenience in the next derivation, I introduce the additive decomposition of the stiffness tensor,

$$\mathcal{C} = \mathcal{C}_{nn} + \mathcal{C}_{nt} + \mathcal{C}_{tn} + \mathcal{C}_{tt}$$

with respect to the left and right multiplications, with \mathcal{N} and \mathcal{T} :

$$\begin{aligned} \mathcal{C}_{nn} &= \mathcal{N} : \mathcal{C} : \mathcal{N} \quad \text{and} \quad \mathcal{C}_{nt} = \mathcal{N} : \mathcal{C} : \mathcal{T}, \\ \mathcal{C}_{tn} &= \mathcal{T} : \mathcal{C} : \mathcal{N} \quad \text{and} \quad \mathcal{C}_{tt} = \mathcal{T} : \mathcal{C} : \mathcal{T}. \end{aligned}$$

Note that the main symmetry in the stiffness tensors is retained

$$(\mathcal{C}_{nn})_{ijkl} = (\mathcal{C}_{nn})_{klij}, \quad (\mathcal{C}_{tt})_{ijkl} = (\mathcal{C}_{tt})_{klij}, \quad \text{but} \quad (\mathcal{C}_{tn})_{ijkl} = (\mathcal{C}_{nt})_{klij}.$$

Furthermore, by using Hooke's law, the normal and tangential decompositions of the phase-dependent Cauchy stress tensor could be rewritten in dependence of the normal and tangential strains, whereby the homogeneous and inhomogeneous variables are marked by the superscript

$$\boldsymbol{\Sigma}_n = \mathcal{N} : \boldsymbol{\Sigma} = \mathcal{C}_{nn}^\alpha : (\mathbf{E}_n^\alpha - \tilde{\mathbf{E}}_n^\alpha) + \mathcal{C}_{nt}^\alpha : (\mathbf{E}_t - \tilde{\mathbf{E}}_t^\alpha) \quad (4.19)$$

$$\boldsymbol{\Sigma}_t^\alpha = \mathcal{T} : \boldsymbol{\Sigma} = \mathcal{C}_{tn}^\alpha : (\mathbf{E}_n^\alpha - \tilde{\mathbf{E}}_n^\alpha) + \mathcal{C}_{tt}^\alpha : (\mathbf{E}_t - \tilde{\mathbf{E}}_t^\alpha). \quad (4.20)$$

Note that the fourth-rank stiffness tensor \mathcal{C}_{nn}^α is singular, but in order to invert the equation of the normal stress, eq. (4.19), for the explicit dependency of the inhomogeneous strain tensor, like in eq. (4.10), in the previous model, the concept of the pseudo inverse is used. Herein, I use the usual notation of the Moore-Penrose inverse and sign it with

$$\mathcal{S}_{nn}^\alpha = (\mathcal{C}_{nn}^\alpha)^+,$$

4. Phase-Field Models with Elasticity

but specify the pseudo inverse in a different manner, namely with the properties, which are assumed to be satisfied

$$\mathcal{S}_{nn}^\alpha : \mathcal{C}_{nn}^\alpha = \mathcal{N} = \mathcal{C}_{nn}^\alpha : \mathcal{S}_{nn}^\alpha, \quad (4.21)$$

$$\mathcal{S}_{nn}^\alpha = (\mathcal{S}_{nn}^\alpha)^T, \quad (4.22)$$

$$\mathcal{S}_{nn}^\alpha = \mathcal{S}_{nn}^\alpha : \mathcal{N} = \mathcal{N} : \mathcal{S}_{nn}^\alpha. \quad (4.23)$$

Thus, the property in eq. (4.21) implies that the pseudo inverse \mathcal{S}_{nn}^α is the left and the right pseudo inverse of the original tensor \mathcal{C}_{nn}^α . Furthermore, it is symmetric, eq. (4.22), in the sense of the main stiffness and compliance symmetry, eq. (4.18), and it is invariant under the left and right product with \mathcal{N} .

With the predefined properties of the pseudo inverse tensor, its uniqueness is trivial to show, whereby the products are used

$$\mathcal{S}_{nn}^\alpha : \mathcal{T} = \mathcal{S}_{nn}^\alpha : \mathcal{T} = \mathcal{O}.$$

Note that the determination of the pseudo inverse for the model by Schneider et al. is equivalent to the calculation of the inverse of \mathbf{C}_{nn}^α in eq. (4.10). The phase-dependent normal strain in the novel approach writes as

$$\mathbf{E}_n^\alpha - \tilde{\mathbf{E}}_n^\alpha = \mathcal{S}_{nn}^\alpha : \boldsymbol{\Sigma}_n - \mathcal{S}_{nn}^\alpha : \mathcal{C}_{nt}^\alpha : \mathbf{E}_t + \mathcal{S}_{nn}^\alpha : \mathcal{C}_{nt}^\alpha : \tilde{\mathbf{E}}_t^\alpha. \quad (4.24)$$

4.4.2. Phase-dependent elastic energy

After some elementary mathematical manipulations, the incorporation of the fourth-rank unity tensor $\mathcal{I} = \mathcal{N} + \mathcal{T}$ in the phase-dependent elastic energy results in

$$f_{el}^\alpha = \frac{1}{2} \left[(\mathbf{E}_n^\alpha - \tilde{\mathbf{E}}_n^\alpha) : \boldsymbol{\Sigma}_n + (\mathbf{E}_t - \tilde{\mathbf{E}}_t^\alpha) : \boldsymbol{\Sigma}_t \right]. \quad (4.25)$$

Substituting the phase-dependent normal elastic strain with the right side of equation (4.24) firstly in the phase-dependent tangential stress in eq. (4.20)

$$\boldsymbol{\Sigma}_t^\alpha = \mathcal{C}_{tn}^\alpha : (\mathcal{S}_{nn}^\alpha : \boldsymbol{\Sigma}_n - \mathcal{S}_{nn}^\alpha : \mathcal{C}_{nt}^\alpha : \mathbf{E}_t + \mathcal{S}_{nn}^\alpha : \mathcal{C}_{nt}^\alpha : \tilde{\mathbf{E}}_t^\alpha) + \mathcal{C}_{tt}^\alpha : (\mathbf{E}_t - \tilde{\mathbf{E}}_t^\alpha)$$

and then both in the elastic energy, eq. (4.25), results in the phase-dependent elastic energy, which is expressed with the homogeneous variables \mathbf{E}_t and $\boldsymbol{\Sigma}_n$ as

$$\begin{aligned} f_{el}^\alpha = \frac{1}{2} \left[\boldsymbol{\Sigma}_n : (\mathcal{S}_{nn}^\alpha : \boldsymbol{\Sigma}_n - \mathcal{S}_{nn}^\alpha : \mathcal{C}_{nt}^\alpha : (\mathbf{E}_t - \tilde{\mathbf{E}}_t^\alpha)) + \right. \\ \left. + (\mathbf{E}_t - \tilde{\mathbf{E}}_t^\alpha) : \left(\mathcal{C}_{tn}^\alpha : (\mathcal{S}_{nn}^\alpha : \boldsymbol{\Sigma}_n - \mathcal{S}_{nn}^\alpha : \mathcal{C}_{nt}^\alpha : (\mathbf{E}_t - \tilde{\mathbf{E}}_t^\alpha)) \right) \right. \\ \left. + \mathcal{C}_{tt}^\alpha : (\mathbf{E}_t - \tilde{\mathbf{E}}_t^\alpha) \right]. \end{aligned}$$

4.4. A new formulation of the elastic energy and the consequential fields

Using the symmetry

$$\boldsymbol{\Sigma}_n : \mathcal{S}_{nn}^\alpha : \mathcal{C}_{nt}^\alpha : (\mathbf{E}_t - \tilde{\mathbf{E}}_t^\alpha) = (\mathbf{E}_t - \tilde{\mathbf{E}}_t^\alpha) : \mathcal{C}_{tn}^\alpha : \mathcal{S}_{nn}^\alpha : \boldsymbol{\Sigma}_n,$$

the phase-dependent elastic energy is simplified to

$$f_{el}^\alpha = \frac{1}{2} \left[\boldsymbol{\Sigma}_n : \mathcal{S}_{nn}^\alpha : \boldsymbol{\Sigma}_n + (\mathbf{E}_t - \tilde{\mathbf{E}}_t^\alpha) : (\mathcal{C}_{tt}^\alpha - \mathcal{C}_{tn}^\alpha : \mathcal{S}_{nn}^\alpha : \mathcal{C}_{nt}^\alpha) : (\mathbf{E}_t - \tilde{\mathbf{E}}_t^\alpha) \right].$$

For further derivations, I will simplify the expression for the elastic energy, whereby I examine the term

$$(\mathbf{E}_t - \tilde{\mathbf{E}}_t^\alpha) : (\mathcal{C}_{tt}^\alpha - \mathcal{C}_{tn}^\alpha : \mathcal{S}_{nn}^\alpha : \mathcal{C}_{nt}^\alpha) : (\mathbf{E}_t - \tilde{\mathbf{E}}_t^\alpha)$$

in a more detailed manner. Knowing that the projection tensor \mathcal{T} is invariant under the left and right multiplication with itself, $\mathcal{T} = \mathcal{T} : \mathcal{T}$, the previous term can be rewritten to

$$(\mathbf{E} - \tilde{\mathbf{E}}^\alpha) : (\mathcal{C}_{tt}^\alpha - \mathcal{C}_{tn}^\alpha : \mathcal{S}_{nn}^\alpha : \mathcal{C}_{nt}^\alpha) : (\mathbf{E} - \tilde{\mathbf{E}}^\alpha). \quad (4.26)$$

By substitution of $\mathcal{T} = \mathcal{I} - \mathcal{N}$, in the appropriate stiffness tensors

$$\begin{aligned} \mathcal{C}_{tt}^\alpha &= \mathcal{C}^\alpha - \mathcal{C}^\alpha : \mathcal{N} - \mathcal{N} : \mathcal{C}^\alpha + \mathcal{N} : \mathcal{C}^\alpha : \mathcal{N} \\ \mathcal{C}_{tn}^\alpha &= \mathcal{C}^\alpha : \mathcal{N} - \mathcal{N} : \mathcal{C}^\alpha : \mathcal{N} \\ \mathcal{C}_{nt}^\alpha &= \mathcal{N} : \mathcal{C}^\alpha - \mathcal{N} : \mathcal{C}^\alpha : \mathcal{N}, \end{aligned}$$

the previous term in (4.26) simplifies to

$$(\mathbf{E} - \tilde{\mathbf{E}}^\alpha) : (\mathcal{C}^\alpha - \mathcal{C}^\alpha : \mathcal{S}_{nn}^\alpha : \mathcal{C}^\alpha) : (\mathbf{E} - \tilde{\mathbf{E}}^\alpha), \quad (4.27)$$

whereby the property of the pseudo inverse in eq. (4.21) was also applied. Finally, the phase-dependent elastic energy can be rewritten in a simple form

$$f_{el}^\alpha = \frac{1}{2} \left[\boldsymbol{\Sigma}_n : \mathcal{S}_{nn}^\alpha : \boldsymbol{\Sigma}_n + (\mathbf{E} - \tilde{\mathbf{E}}^\alpha) : (\mathcal{C}^\alpha - \mathcal{C}^\alpha : \mathcal{S}_{nn}^\alpha : \mathcal{C}^\alpha) : (\mathbf{E} - \tilde{\mathbf{E}}^\alpha) \right].$$

Note that the previous formula of the phase-dependent elastic energy is written with the total strain tensor \mathbf{E} and with the normal Cauchy stress tensor $\boldsymbol{\Sigma}_n$. Because of the equivalence

$$(\mathcal{C}^\alpha - \mathcal{C}^\alpha : \mathcal{S}_{nn}^\alpha : \mathcal{C}^\alpha) : (\mathbf{E}_t - \tilde{\mathbf{E}}_t^\alpha) = (\mathcal{C}^\alpha - \mathcal{C}^\alpha : \mathcal{S}_{nn}^\alpha : \mathcal{C}^\alpha) : (\mathbf{E} - \tilde{\mathbf{E}}^\alpha),$$

any normal strain \mathbf{E}_n is the kernel for the composed stiffness $\mathcal{C}^\alpha - \mathcal{C}^\alpha : \mathcal{S}_{nn}^\alpha : \mathcal{C}^\alpha$. It means that any normal strain contribution could be additively incorporated into the phase-dependent tangential elastic strain, without a change in the elastic energy magnitude. In a similar manner, the normal stress could also be modified additively by any tangential constituent because they are the kernel of \mathcal{S}_{nn} .

4.4.3. Elastic energy in the diffuse interface

The reason for writing the phase-dependent elastic energies in dependence of interfacial homogeneous variables in the previous section is their further interpolation. Therefore, using the interpolation functions h_α and h_β , the interpolated elastic energy in the diffuse interface

$$f_{el}(\boldsymbol{\Sigma}_n, \mathbf{E}, \phi) = f_{el}^\alpha(\boldsymbol{\Sigma}_n, \mathbf{E})h_\alpha(\phi) + f_{el}^\beta(\boldsymbol{\Sigma}_n, \mathbf{E})h_\beta(\phi)$$

could be rewritten explicitly because of the bilinearity in the Frobenius inner product

$$\boldsymbol{\Sigma}_n : \mathcal{S}_{nn}^\alpha : \boldsymbol{\Sigma}_n h_\alpha + \boldsymbol{\Sigma}_n : \mathcal{S}_{nn}^\beta : \boldsymbol{\Sigma}_n h_\beta = \boldsymbol{\Sigma}_n : (\mathcal{S}_{nn}^\alpha h_\alpha + \mathcal{S}_{nn}^\beta h_\beta) : \boldsymbol{\Sigma}_n,$$

as

$$\begin{aligned} f_{el}(\boldsymbol{\Sigma}_n, \mathbf{E}, \phi) = & \frac{1}{2} \left[\boldsymbol{\Sigma}_n : (\mathcal{S}_{nn}^\alpha h_\alpha + \mathcal{S}_{nn}^\beta h_\beta) : \boldsymbol{\Sigma}_n + \right. \\ & + (\mathbf{E} - \tilde{\mathbf{E}}^\alpha) : (\mathcal{C}^\alpha - \mathcal{C}^\alpha : \mathcal{S}_{nn}^\alpha : \mathcal{C}^\alpha) : (\mathbf{E} - \tilde{\mathbf{E}}^\alpha) h_\alpha + \\ & \left. + (\mathbf{E} - \tilde{\mathbf{E}}^\beta) : (\mathcal{C}^\beta - \mathcal{C}^\beta : \mathcal{S}_{nn}^\beta : \mathcal{C}^\beta) : (\mathbf{E} - \tilde{\mathbf{E}}^\beta) h_\beta \right]. \quad (4.28) \end{aligned}$$

In the next derivation step, the normal stress $\boldsymbol{\Sigma}_n$ will be replaced by the expression in dependence of the total strain. Motivated by the results in the preliminary works for chemical [43] and mechanical [30] systems, the inhomogeneous variables are directly interpolated in the diffuse interface. Therefore, by the assumption that the total normal strain is nothing but the direct interpolation of the phase-dependent normal strains,

$$\mathbf{E}_n = \mathbf{E}_n^\alpha h_\alpha + \mathbf{E}_n^\beta h_\beta,$$

and with the incorporation of the right-hand sides of eq. (4.24) into the previous equation, the total normal strain equates to

$$\begin{aligned} \mathbf{E}_n = & (\mathcal{S}_{nn}^\alpha h_\alpha + \mathcal{S}_{nn}^\beta h_\beta) : \boldsymbol{\Sigma}_n - (\mathcal{S}_{nn}^\alpha : \mathcal{C}_{nt}^\alpha h_\alpha + \mathcal{S}_{nn}^\beta : \mathcal{C}_{nt}^\beta h_\beta) : \mathbf{E} + \\ & + (\mathcal{S}_{nn}^\alpha : \mathcal{C}^\alpha : \tilde{\mathbf{E}}^\alpha h_\alpha + \mathcal{S}_{nn}^\beta : \mathcal{C}^\beta : \tilde{\mathbf{E}}^\beta h_\beta). \end{aligned}$$

To express the normal stress tensor $\boldsymbol{\Sigma}_n(\mathbf{E})$ in dependency of the total strain tensor \mathbf{E} , which is given as a displacement gradient in eq. (4.3), I again use the pseudo inverse, but now the one of the interpolated normal compliance tensor, written in a shorthand notation

$$\mathcal{S}_{nn} = \mathcal{S}_{nn}^\alpha h_\alpha + \mathcal{S}_{nn}^\beta h_\beta. \quad (4.29)$$

4.4. A new formulation of the elastic energy and the consequential fields

Therefore, this reformulation step results in the expression for the homogeneous normal stress, which is now written as

$$\boldsymbol{\Sigma}_n = \mathcal{S}_{nn}^+ : (\mathcal{S}_{nn}^\alpha : \mathcal{C}^\alpha : (\mathbf{E} - \tilde{\mathbf{E}}^\alpha)h_\alpha + \mathcal{S}_{nn}^\beta : \mathcal{C}^\beta : (\mathbf{E} - \tilde{\mathbf{E}}^\beta)h_\beta). \quad (4.30)$$

By the substitution of the normal stress $\boldsymbol{\Sigma}_n$ in the interpolated elastic energy in eq. (4.28), with the right-hand side of eq. (4.30), and by using $\mathcal{S}_{nn} : \mathcal{S}_{nn}^+ = \mathcal{N}$, the strain energy takes the following form

$$\begin{aligned} f_{el}(\phi) = \frac{1}{2} & \left[((\mathbf{E} - \tilde{\mathbf{E}}^\alpha) : \mathcal{C}^\alpha : \mathcal{S}_{nn}^\alpha h_\alpha + (\mathbf{E} - \tilde{\mathbf{E}}^\beta) : \mathcal{C}^\beta : \mathcal{S}_{nn}^\beta h_\beta) : \right. \\ & : (\mathcal{S}_{nn}^\alpha h_\alpha + \mathcal{S}_{nn}^\beta h_\beta)^+ : \\ & : (\mathcal{S}_{nn}^\alpha : \mathcal{C}^\alpha : (\mathbf{E} - \tilde{\mathbf{E}}^\alpha)h_\alpha + \mathcal{S}_{nn}^\beta : \mathcal{C}^\beta : (\mathbf{E} - \tilde{\mathbf{E}}^\beta)h_\beta) + \\ & + (\mathbf{E} - \tilde{\mathbf{E}}^\alpha) : (\mathcal{C}^\alpha - \mathcal{C}^\alpha : \mathcal{S}_{nn}^\alpha : \mathcal{C}^\alpha) : (\mathbf{E} - \tilde{\mathbf{E}}^\alpha)h_\alpha + \\ & \left. + (\mathbf{E} - \tilde{\mathbf{E}}^\beta) : (\mathcal{C}^\beta - \mathcal{C}^\beta : \mathcal{S}_{nn}^\beta : \mathcal{C}^\beta) : (\mathbf{E} - \tilde{\mathbf{E}}^\beta)h_\beta \right]. \end{aligned}$$

This complex explicit expression of the interpolated elastic energy can be simplified by the straightforward manner. Doing so, I introduce some abbreviations to write the terms in shorthand notations. Thus,

$$\boldsymbol{\Sigma}^\alpha = \mathcal{C}^\alpha : (\mathbf{E} - \tilde{\mathbf{E}}^\alpha) \quad \text{and} \quad \boldsymbol{\Sigma}^\beta = \mathcal{C}^\beta : (\mathbf{E} - \tilde{\mathbf{E}}^\beta)$$

are stress tensors, which are defined for every phase, but are evaluated with the total strain \mathbf{E} and not with the phase-dependent strains \mathbf{E}^α or \mathbf{E}^β , respectively,

$$\boldsymbol{\Sigma}^\alpha \neq \mathcal{C}^\alpha : (\mathbf{E}^\alpha - \tilde{\mathbf{E}}^\alpha) \quad \text{and} \quad \boldsymbol{\Sigma}^\beta \neq \mathcal{C}^\beta : (\mathbf{E}^\beta - \tilde{\mathbf{E}}^\beta).$$

But the so defined tensors are the stresses, which could be found in the Voigt homogenisation approach, in which the total strain is assumed to be a homogeneous state variable [28, 30].

Therefore, with the introduced shorthand notations, I rewrite the interpolated elastic energy to

$$\begin{aligned} f_{el}(\phi) = \frac{1}{2} & \left[(\boldsymbol{\Sigma}^\alpha : \mathcal{S}_{nn}^\alpha h_\alpha + \boldsymbol{\Sigma}^\beta : \mathcal{S}_{nn}^\beta h_\beta) : \mathcal{S}_{nn}^+ : (\mathcal{S}_{nn}^\alpha : \boldsymbol{\Sigma}^\alpha h_\alpha + \mathcal{S}_{nn}^\beta : \boldsymbol{\Sigma}^\beta h_\beta) + \right. \\ & + (\mathbf{E} - \tilde{\mathbf{E}}^\alpha) : (\mathcal{I} - \mathcal{C}^\alpha : \mathcal{S}_{nn}^\alpha) : \boldsymbol{\Sigma}^\alpha h_\alpha + \\ & \left. + (\mathbf{E} - \tilde{\mathbf{E}}^\beta) : (\mathcal{I} - \mathcal{C}^\beta : \mathcal{S}_{nn}^\beta) : \boldsymbol{\Sigma}^\beta h_\beta \right]. \end{aligned}$$

The second and third lines are results of the factor out of the stiffness tensors

4. Phase-Field Models with Elasticity

\mathcal{C}^α and \mathcal{C}^β , respectively. Further, I dissolve the parentheses to get

$$\begin{aligned} f_{el}(\phi) = & \frac{1}{2} \left[(\boldsymbol{\Sigma}^\alpha : \mathcal{S}_{nn}^\alpha h_\alpha + \boldsymbol{\Sigma}^\beta : \mathcal{S}_{nn}^\beta h_\beta) : \mathcal{S}_{nn}^+ : (\mathcal{S}_{nn}^\alpha : \boldsymbol{\Sigma}^\alpha h_\alpha + \mathcal{S}_{nn}^\beta : \boldsymbol{\Sigma}^\beta h_\beta) \right) - \\ & - \boldsymbol{\Sigma}^\alpha : \mathcal{S}_{nn}^\alpha : \boldsymbol{\Sigma}^\alpha h_\alpha - \boldsymbol{\Sigma}^\beta : \mathcal{S}_{nn}^\beta : \boldsymbol{\Sigma}^\beta h_\beta + \\ & + (\mathbf{E} - \tilde{\mathbf{E}}^\alpha) : \boldsymbol{\Sigma}^\alpha h_\alpha + (\mathbf{E} - \tilde{\mathbf{E}}^\beta) : \boldsymbol{\Sigma}^\beta h_\beta \Big]. \end{aligned}$$

Finally, the terms $\boldsymbol{\Sigma}^\alpha h_\alpha$ and $\boldsymbol{\Sigma}^\beta h_\beta$ are excluded in the common terms:

$$\begin{aligned} f_{el}(\phi) = & \frac{1}{2} \left[(\mathbf{E} - \tilde{\mathbf{E}}^\alpha) : \boldsymbol{\Sigma}^\alpha h_\alpha + (\mathbf{E} - \tilde{\mathbf{E}}^\beta) : \boldsymbol{\Sigma}^\beta h_\beta + \right. \\ & + \boldsymbol{\Sigma}^\alpha : (\mathcal{S}_{nn}^\alpha : \mathcal{S}_{nn}^+ : (\mathcal{S}_{nn}^\alpha : \boldsymbol{\Sigma}^\alpha h_\alpha + \mathcal{S}_{nn}^\beta : \boldsymbol{\Sigma}^\beta h_\beta) - \mathcal{S}_{nn}^\alpha : \boldsymbol{\Sigma}^\alpha) h_\alpha + \\ & \left. + \boldsymbol{\Sigma}^\beta : (\mathcal{S}_{nn}^\beta : \mathcal{S}_{nn}^+ : (\mathcal{S}_{nn}^\alpha : \boldsymbol{\Sigma}^\alpha h_\alpha + \mathcal{S}_{nn}^\beta : \boldsymbol{\Sigma}^\beta h_\beta) - \mathcal{S}_{nn}^\beta : \boldsymbol{\Sigma}^\beta) h_\beta \right]. \end{aligned} \quad (4.31)$$

In order to simplify the previous expression, I separately analyse the strain terms in the big parentheses. Looking into the further derivation steps, it has proved to be useful to define an interpolated stiffness tensor

$$\bar{\mathcal{C}}^{\alpha\beta} = \mathcal{C}^\alpha h_\beta + \mathcal{C}^\beta h_\alpha.$$

Note that the interpolation appears with the appropriate functions, but in an asymmetric manner. Its projective part on the normal subspace is defined as

$$\bar{\mathcal{C}}_{nn}^{\alpha\beta} = \mathcal{N} : \bar{\mathcal{C}}^{\alpha\beta} : \mathcal{N},$$

and I use the notation

$$\bar{\mathcal{S}}_{nn}^{\alpha\beta} = (\bar{\mathcal{C}}_{nn}^{\alpha\beta})^+$$

for the pseudo inverse. With the predefined quantities, the following tensor product in eq. (4.31),

$$\begin{aligned} \mathcal{S}_{nn}^\alpha : \mathcal{S}_{nn}^+ : \mathcal{S}_{nn}^\beta &= (\mathcal{C}_{nn}^\alpha)^+ : \mathcal{S}_{nn}^+ : (\mathcal{C}_{nn}^\beta)^+ = (\mathcal{C}_{nn}^\beta : \mathcal{S}_{nn} : \mathcal{C}_{nn}^\alpha)^+ = \\ &= (\mathcal{C}_{nn}^\beta : (\mathcal{S}_{nn}^\alpha h_\alpha + \mathcal{S}_{nn}^\beta h_\beta) : \mathcal{C}_{nn}^\alpha)^+ = (\mathcal{C}_{nn}^\beta h_\alpha + \mathcal{C}_{nn}^\alpha h_\beta)^+ = \bar{\mathcal{S}}_{nn}^{\alpha\beta}, \end{aligned}$$

can be rewritten, and similarly $\mathcal{S}_{nn}^\beta : \mathcal{S}_{nn}^+ : \mathcal{S}_{nn}^\alpha = \bar{\mathcal{S}}_{nn}^{\alpha\beta}$, whereby I used the properties of the pseudo inverse product $\mathcal{A}^+ : \mathcal{B}^+ = (\mathcal{B} : \mathcal{A})^+$. Therefore, the parentheses with $\boldsymbol{\Sigma}^\alpha$ as a factor in the interpolated strain energy is modified in eq. (4.31) to the following form

$$\begin{aligned} \mathcal{S}_{nn}^\alpha : \mathcal{S}_{nn}^+ : (\mathcal{S}_{nn}^\alpha : \boldsymbol{\Sigma}^\alpha h_\alpha + \mathcal{S}_{nn}^\beta : \boldsymbol{\Sigma}^\beta h_\beta) - \mathcal{S}_{nn}^\alpha : \boldsymbol{\Sigma}^\alpha &= \\ = \bar{\mathcal{S}}_{nn}^{\alpha\beta} : \boldsymbol{\Sigma}^\beta h_\beta + \mathcal{S}_{nn}^\alpha : \mathcal{S}_{nn}^+ : \mathcal{S}_{nn}^\alpha : \boldsymbol{\Sigma}^\alpha h_\alpha - \mathcal{S}_{nn}^\alpha : \boldsymbol{\Sigma}^\alpha &= \\ = \bar{\mathcal{S}}_{nn}^{\alpha\beta} : \boldsymbol{\Sigma}^\beta h_\beta - (\mathcal{N} - \mathcal{S}_{nn}^\alpha : \mathcal{S}_{nn}^+ h_\alpha) : \mathcal{S}_{nn}^\alpha : \boldsymbol{\Sigma}^\alpha. \end{aligned} \quad (4.32)$$

4.4. A new formulation of the elastic energy and the consequential fields

Here, I used the invariance of the pseudo inverse, with respect to the left product with the projection tensor $\mathcal{N} : \mathcal{S}_{nn}^\alpha = \mathcal{S}_{nn}^\alpha$. Furthermore, using

$$\mathcal{N} = \mathcal{S}_{nn} : \mathcal{S}_{nn}^+,$$

and incorporating it in eq. (4.32), it can be simplified with the following modifications by using the definitions of \mathcal{S}_{nn} in eq. (4.29)

$$\begin{aligned} & \bar{\mathcal{S}}_{nn}^{\alpha\beta} : \Sigma^\beta h_\beta - (\mathcal{N} - \mathcal{S}_{nn}^\alpha : \mathcal{S}_{nn}^+ h_\alpha) : \mathcal{S}_{nn}^\alpha : \Sigma^\alpha = \\ & = \bar{\mathcal{S}}_{nn}^{\alpha\beta} : \Sigma^\beta h_\beta - (\mathcal{S}_{nn} : \mathcal{S}_{nn}^+ - \mathcal{S}_{nn}^\alpha : \mathcal{S}_{nn}^+ h_\alpha) : \mathcal{S}_{nn}^\alpha : \Sigma^\alpha = \\ & = \bar{\mathcal{S}}_{nn}^{\alpha\beta} : \Sigma^\beta h_\beta - (\mathcal{S}_{nn} - \mathcal{S}_{nn}^\alpha h_\alpha) : \mathcal{S}_{nn}^+ : \mathcal{S}_{nn}^\alpha : \Sigma^\alpha = \\ & = \bar{\mathcal{S}}_{nn}^{\alpha\beta} : \Sigma^\beta h_\beta - \mathcal{S}_{nn}^\beta : \mathcal{S}_{nn}^+ : \mathcal{S}_{nn}^\alpha : \Sigma^\alpha h_\beta = \\ & = \bar{\mathcal{S}}_{nn}^{\alpha\beta} : \Sigma^\beta h_\beta - \bar{\mathcal{S}}_{nn}^{\alpha\beta} : \Sigma^\alpha h_\beta = \\ & = \bar{\mathcal{S}}_{nn}^{\alpha\beta} : (\Sigma^\beta - \Sigma^\alpha) h_\beta. \end{aligned} \tag{4.33}$$

Similar simplifications are derived for

$$\mathcal{S}_{nn}^\beta : \mathcal{S}_{nn}^+ : (\mathcal{S}_{nn}^\alpha : \Sigma^\alpha h_\alpha + \mathcal{S}_{nn}^\beta : \Sigma^\beta h_\beta) - \mathcal{S}_{nn}^\beta : \Sigma^\beta = \bar{\mathcal{S}}_{nn}^{\alpha\beta} : (\Sigma^\alpha - \Sigma^\beta) h_\alpha. \tag{4.34}$$

Finally, the substitution of the simplified terms in eqs. (4.33) and (4.34), for their equivalents in the big parentheses in the elastic energy in eq. (4.31), allows to rewrite the interpolated strain energy in the diffuse interface in its final elegant form as

$$\boxed{f_{el}(\phi, \nabla\phi, \mathbf{E}) = \frac{1}{2} \left[(\mathbf{E} - \tilde{\mathbf{E}}^\alpha) : \Sigma^\alpha h_\alpha + (\mathbf{E} - \tilde{\mathbf{E}}^\beta) : \Sigma^\beta h_\beta - (\Sigma^\alpha - \Sigma^\beta) : \bar{\mathcal{S}}_{nn}^{\alpha\beta} : (\Sigma^\alpha - \Sigma^\beta) h_\alpha h_\beta \right]} \tag{4.35}$$

The previous formula is the central result of this thesis. The interpolated elastic energy is written in terms of the thermodynamically consistent system variables, namely the displacement \mathbf{u} , the phase-field ϕ and their gradients \mathbf{E} and $\nabla\phi$. Therefore, all variational derivatives are determined by the explicit dependencies on the state variables.

Note that both elastic energies, given for the previous model in eq. (4.11) and for the new formalism, eq. (4.35), formally differ, but are equivalent to each other. A disadvantage of the previous formulation in eq. (4.11) lies in the dependency on the unknown phase-dependent strains ε^α and ε^β . This is not the case in the new formula, eq. (4.35). Furthermore, the dependence of the elastic energy on the tangential vectors in the previous model in sec. 4.3 is not present in the renewed expression, eq. (4.35).

4. Phase-Field Models with Elasticity

On the other hand, the question of the explicit determination of the pseudo inverse $\tilde{\mathcal{S}}_{nn}$ in the newly formulated elastic energy interpolation is not clear but is treated in the next section. Referring to the next section, sec. 4.5, in which the Voigt notation of the stress and strain is used, the explicit calculation of the last term in the brackets in eq. (4.35) is presented and the mentioned lack is removed.

Since the sum of the first two summands corresponds to the strain energy with the Voigt homogenisation scheme [28], the subtrahend corrects the erroneous interpolation in the diffuse interface. Moreover, in the diffuse interface of two elastic twin phases, also with the same elastic stiffness tensors and the same eigenstrains, the subtrahend vanishes and the strain energy solely reduces to a bulk contribution.

By using the variational principle, the other required quantities are derived in a straightforward manner. Thus, the Cauchy stress tensor is given by the variation of the strain energy, with respect to the displacement, and the elastic driving force results from the variational derivative with respect to the appropriate phase-field variable.

4.4.4. Calculation of the stress tensor

As mentioned, I calculate the Cauchy stress by the variational approach in accordance with the thermodynamical connection between the stress tensor components and the derivatives of the strain energy, with respect to the strain tensor components

$$\Sigma_{ij} = \frac{\partial f_{el}}{\partial E_{ij}}.$$

Therefore, the Cauchy stress tensor writes as

$$\Sigma = \Sigma^\alpha h_\alpha + \Sigma^\beta h_\beta - (\mathcal{C}^\alpha - \mathcal{C}^\beta) : \tilde{\mathcal{S}}_{nn}^{\alpha\beta} : (\Sigma^\alpha - \Sigma^\beta) h_\alpha h_\beta.$$

By introducing a shorthand notation for the stress difference $\Delta\Sigma^{\alpha\beta} = \Sigma^\alpha - \Sigma^\beta$, the stress calculation in the diffuse interface results in

$$\Sigma = \Sigma^\alpha h_\alpha + \Sigma^\beta h_\beta - (\mathcal{C}^\alpha - \mathcal{C}^\beta) : \tilde{\mathcal{S}}_{nn}^{\alpha\beta} : \Delta\Sigma^{\alpha\beta} h_\alpha h_\beta. \quad (4.36)$$

Note that in the case of the same stiffness tensors the stress calculation reduces to the Voigt stress calculation scheme [28].

Alternatively, the stress tensor could be derived by the summation of the normal stress Σ_n in eq. (4.30), together with the interpolated tangential stress

$$\Sigma_t = \Sigma_t^\alpha h_\alpha + \Sigma_t^\beta h_\beta.$$

4.4. A new formulation of the elastic energy and the consequential fields

Following this procedure, the phase-dependent tangential stresses Σ_t^α and Σ_t^β should be rewritten in terms of the total strain tensor \mathbf{E} . At first, the phase-dependent normal elastic strains are substituted by the right-hand side eq. (4.24), and the normal stress is replaced with its equivalent from eq. (4.30). In the end, the resulting Cauchy stress takes the same form as eq. (4.36).

4.4.5. Elastic driving force

The elastic driving force for the phase transformation is given as a variational derivative of the strain energy, with respect to the phase-field variable, written as

$$\frac{\delta f_{el}}{\delta \phi_\alpha} = \frac{\partial f_{el}}{\partial \phi_\alpha} - \nabla \cdot \frac{\partial f_{el}}{\partial \nabla \phi_\alpha}. \quad (4.37)$$

Since the derivative with respect to the phase-field variable is straightforward, the calculation of the derivative with respect to phase-field gradient requires a sophisticated approach. The main difficulty lies in the calculation of the derivative for the subtrahend because the tensor $\bar{\mathcal{S}}_{nn}^{\alpha\beta}(\phi, \nabla\phi)$ depends on the phase-field variables as well as on the phase-field gradient.

In the next paragraphs, I will write the derivatives exemplarily to the phase-field function ϕ_α and to its gradient $\nabla\phi_\alpha$.

The variational derivative with respect to ϕ_α

The derivative of the pseudo inverse tensor

$$\frac{\partial \bar{\mathcal{S}}_{nn}^{\alpha\beta}}{\partial \phi_\alpha} = \frac{\partial \left(\mathcal{N} : (\mathcal{C}^\alpha h_\beta(\phi) + \mathcal{C}^\beta h_\alpha(\phi_\alpha)) : \mathcal{N} \right)^+}{\partial \phi_\alpha}$$

can be derived by the derivative of the projection tensor \mathcal{N} , which will be written as a tensor product

$$\frac{\partial}{\partial \phi_\alpha} \mathcal{N} = \mathcal{O} = \frac{\partial}{\partial \phi_\alpha} \left(\bar{\mathcal{S}}_{nn}^{\alpha\beta} : \bar{\mathcal{C}}_{nn}^{\alpha\beta} \right).$$

Hence, by the usage of the product rule on the right hand side of the previous equation, it rewrites to

$$\frac{\partial}{\partial \phi_\alpha} \bar{\mathcal{S}}_{nn}^{\alpha\beta} : \bar{\mathcal{C}}_{nn}^{\alpha\beta} = -\bar{\mathcal{S}}_{nn}^{\alpha\beta} : \frac{\partial}{\partial \phi_\alpha} \bar{\mathcal{C}}_{nn}^{\alpha\beta}.$$

4. Phase-Field Models with Elasticity

By multiplying both sides with $\bar{\mathcal{S}}_{nn}^{\alpha\beta}$, it results in

$$\frac{\partial}{\partial\phi_\alpha}\bar{\mathcal{S}}_{nn}^{\alpha\beta} : \mathcal{N} = -\bar{\mathcal{S}}_{nn}^{\alpha\beta} : \frac{\partial}{\partial\phi_\alpha}\bar{\mathcal{C}}_{nn}^{\alpha\beta} : \bar{\mathcal{S}}_{nn}^{\alpha\beta} = -\bar{\mathcal{S}}_{nn}^{\alpha\beta} : \mathcal{C}^\beta : \bar{\mathcal{S}}_{nn}^{\alpha\beta} h'_\alpha, \quad (4.38)$$

whereby I assume the dependency of the interpolation functions $h_\alpha(\phi)$ to be solely on the corresponding phase-field variable $h_\alpha(\phi) = h(\phi_\alpha)$; consequently,

$$\frac{\partial h_\beta(\phi)}{\partial\phi_\alpha} = 0, \quad \text{for } \beta \neq \alpha.$$

For the general formulation, see examples in [47, 85] and appendix A. Analogous to the formula in eq. (4.38), a similar expression can be derived with the left product

$$\mathcal{N} : \frac{\partial}{\partial\phi_\alpha}\bar{\mathcal{S}}_{nn}^{\alpha\beta} = -\bar{\mathcal{S}}_{nn}^{\alpha\beta} : \frac{\partial}{\partial\phi_\alpha}\bar{\mathcal{C}}_{nn}^{\alpha\beta} : \bar{\mathcal{S}}_{nn}^{\alpha\beta} = -\bar{\mathcal{S}}_{nn}^{\alpha\beta} : \mathcal{C}^\beta : \bar{\mathcal{S}}_{nn}^{\alpha\beta} h'_\alpha.$$

Therefore, the derivative of the elastic energy, with respect to the phase-field variable ϕ_α , results in

$$\begin{aligned} \frac{\partial f_{el}}{\partial\phi_\alpha} = \frac{1}{2} & \left[(\mathbf{E} - \tilde{\mathbf{E}}^\alpha) : \Sigma^\alpha - \Delta\Sigma^{\alpha\beta} : \bar{\mathcal{S}}_{nn}^{\alpha\beta} : \Delta\Sigma^{\alpha\beta} h_\beta + \right. \\ & \left. + \Delta\Sigma^{\alpha\beta} : \bar{\mathcal{S}}_{nn}^{\alpha\beta} : \mathcal{C}^\beta : \bar{\mathcal{S}}_{nn}^{\alpha\beta} : \Delta\Sigma^{\alpha\beta} h_\beta h_\alpha \right] h'_\alpha. \end{aligned}$$

The first expression of the derivative can be simplified using the required invariance of the pseudo inverse due to the left and right products with the projection tensor \mathcal{N} , which also can be expressed as a product. Thus, I rewrite the previous equation to equivalent forms

$$\begin{aligned} \frac{\partial f_{el}}{\partial\phi_\alpha} &= \frac{1}{2} \left[(\mathbf{E} - \tilde{\mathbf{E}}^\alpha) : \Sigma^\alpha - \Delta\Sigma^{\alpha\beta} : \bar{\mathcal{S}}_{nn}^{\alpha\beta} : \bar{\mathcal{C}}^{\alpha\beta} : \bar{\mathcal{S}}_{nn}^{\alpha\beta} : \Delta\Sigma^{\alpha\beta} h_\beta + \right. \\ & \quad \left. + \Delta\Sigma^{\alpha\beta} : \bar{\mathcal{S}}_{nn}^{\alpha\beta} : \mathcal{C}^\beta h_\alpha : \bar{\mathcal{S}}_{nn}^{\alpha\beta} : \Delta\Sigma^{\alpha\beta} h_\beta \right] h'_\alpha = \\ &= \frac{1}{2} \left[(\mathbf{E} - \tilde{\mathbf{E}}^\alpha) : \Sigma^\alpha - \Delta\Sigma^{\alpha\beta} : \bar{\mathcal{S}}_{nn}^{\alpha\beta} : (\bar{\mathcal{C}}^{\alpha\beta} - \mathcal{C}^\beta h_\alpha) : \bar{\mathcal{S}}_{nn}^{\alpha\beta} : \Delta\Sigma^{\alpha\beta} h_\beta \right] h'_\alpha, \end{aligned}$$

and by remembering the definition of $\bar{\mathcal{C}}^{\alpha\beta}$, the difference can be replaced with its equivalent $\mathcal{C}^\alpha h_\beta = \bar{\mathcal{C}} - \mathcal{C}^\beta h_\alpha$. Subsequently, the derivative of the interfacial elastic energy, with respect to the phase-field variable ϕ_α , writes as

$$\frac{\partial f_{el}}{\partial\phi_\alpha} = \frac{1}{2} \left[(\mathbf{E} - \tilde{\mathbf{E}}^\alpha) : \Sigma^\alpha - \Delta\Sigma^{\alpha\beta} : \bar{\mathcal{S}}_{nn}^{\alpha\beta} : \mathcal{C}^\alpha : \bar{\mathcal{S}}_{nn}^{\alpha\beta} : \Delta\Sigma^{\alpha\beta} h_\beta^2 \right] h'_\alpha,$$

or, using the abbreviation $\Delta\bar{\mathbf{E}}^{\alpha\beta} = \bar{\mathcal{S}}_{nn}^{\alpha\beta} : (\Sigma^\alpha - \Sigma^\beta)$, as

$$\boxed{\frac{\partial f_{el}}{\partial\phi_\alpha} = \frac{1}{2} \left[(\mathbf{E} - \tilde{\mathbf{E}}^\alpha) : \Sigma^\alpha - \Delta\bar{\mathbf{E}}^{\alpha\beta} : \mathcal{C}^\alpha : \Delta\bar{\mathbf{E}}^{\alpha\beta} h_\beta^2 \right] h'_\alpha.} \quad (4.39)$$

4.4. A new formulation of the elastic energy and the consequential fields

The variational derivative with respect to $\nabla\phi_\alpha$

The derivation of the derivative of the elastic energy in eq. (4.35), with respect to the phase-field gradient, is more technical. Basically, the whole formalism is founded on the usage of the normal vector \mathbf{n} , and the projection tensors \mathcal{N} and $\mathcal{T} = \mathcal{I} - \mathcal{N}$ as well as the projective stiffness and compliance tensors are written explicitly depending on the normal vector components.

The normal vector can be defined in several ways. In their works [40, 20], Nestler and Garcke use the asymmetric vector

$$\mathbf{q}_{\alpha\beta} = \phi_\alpha \nabla\phi_\beta - \phi_\beta \nabla\phi_\alpha$$

to identify the orientation of the α - β interface. Therefore, the normal vector is given as $\mathbf{n} = \mathbf{q}_{\alpha\beta}/|\mathbf{q}_{\alpha\beta}|$. In the two-phase case, the vector $\mathbf{q}_{\alpha\beta}$ is parallel to both $\nabla\phi_\alpha$ and $\nabla\phi_\beta$. Looking ahead, it turned out to take another definition of the normal vector, namely

$$\mathbf{n} = \frac{\nabla(\phi_\alpha - \phi_\beta)}{|\nabla(\phi_\alpha - \phi_\beta)|}. \quad (4.40)$$

Contrary to the asymmetric vector $\mathbf{q}_{\alpha\beta}$, the normal in eq. (4.40) is also perpendicular to the locus $\phi_\alpha - \phi_\beta = \text{const}$ in the multipoint junctions.

Nevertheless, regardless of the determination of the normal vector \mathbf{n} , the derivative with respect to the phase-field gradient is derived by the usage of the chain rule

$$\frac{\partial f_{el}}{\partial \nabla\phi_\alpha} = \frac{\partial \mathbf{n}}{\partial \nabla\phi_\alpha} \frac{\partial f_{el}}{\partial \mathbf{n}}.$$

The term $\frac{\partial f_{el}}{\partial \mathbf{n}}$ depends on the normal vector components. For a further derivation, I use the preliminary equivalences

$$\frac{\partial}{\partial n_i} \mathcal{N} = \frac{\partial}{\partial n_i} \bar{\mathcal{S}}_{nn}^{\alpha\beta} : \bar{\mathcal{C}}_{nn}^{\alpha\beta} + \bar{\mathcal{S}}_{nn}^{\alpha\beta} : \frac{\partial}{\partial n_i} \bar{\mathcal{C}}_{nn}^{\alpha\beta} = \mathcal{D}_i \quad (4.41)$$

$$\frac{\partial}{\partial n_i} (\bar{\mathcal{S}}_{nn}^{\alpha\beta} : \mathcal{N}) = \frac{\partial}{\partial n_i} \bar{\mathcal{S}}_{nn}^{\alpha\beta} : \mathcal{N} + \bar{\mathcal{S}}_{nn}^{\alpha\beta} : \mathcal{D}_i = \frac{\partial}{\partial n_i} \bar{\mathcal{S}}_{nn}^{\alpha\beta} \quad (4.42)$$

where the tensor \mathcal{D}_i is the derivative of the projection \mathcal{N} , with respect to the normal component n_i . Thus, I reformulate eq. (4.41) by the right multiplication with $\bar{\mathcal{S}}_{nn}^{\alpha\beta}$, and by using the identity $\bar{\mathcal{C}}_{nn}^{\alpha\beta} : \bar{\mathcal{S}}_{nn}^{\alpha\beta} = \mathcal{N}$ once again, I obtain the equality

$$\frac{\partial}{\partial n_i} \bar{\mathcal{S}}_{nn}^{\alpha\beta} : \mathcal{N} = \mathcal{D}_i : \bar{\mathcal{S}}_{nn}^{\alpha\beta} - \bar{\mathcal{S}}_{nn}^{\alpha\beta} : \frac{\partial}{\partial n_i} \bar{\mathcal{C}}_{nn}^{\alpha\beta} : \bar{\mathcal{S}}_{nn}^{\alpha\beta}.$$

4. Phase-Field Models with Elasticity

In the next step, I substitute $\frac{\partial}{\partial n_i} \bar{\mathcal{S}}_{nn}^{\alpha\beta} : \mathcal{N}$ in eq. (4.42) with the right-hand side of the previous equation to get

$$\frac{\partial}{\partial n_i} \bar{\mathcal{S}}_{nn}^{\alpha\beta} = \mathcal{D}_i : \bar{\mathcal{S}}_{nn}^{\alpha\beta} + \bar{\mathcal{S}}_{nn}^{\alpha\beta} : \mathcal{D}_i - \bar{\mathcal{S}}_{nn}^{\alpha\beta} : \frac{\partial}{\partial n_i} \bar{\mathcal{C}}_{nn}^{\alpha\beta} : \bar{\mathcal{S}}_{nn}^{\alpha\beta}.$$

Now, I explicitly write the derivative of the projective, asymmetrically interpolated stiffness tensor

$$\frac{\partial}{\partial n_i} \bar{\mathcal{C}}_{nn}^{\alpha\beta} = \mathcal{D}_i : \bar{\mathcal{C}}^{\alpha\beta} : \mathcal{N} + \mathcal{N} : \bar{\mathcal{C}}^{\alpha\beta} : \mathcal{D}_i.$$

The incorporation of the derived expressions into the variational derivative of the elastic energy, with respect to the i -th component of the normal vector, yields

$$\begin{aligned} \frac{\partial f_{el}}{\partial n_i} = & -\frac{1}{2} \Delta \Sigma^{\alpha\beta} : \left(\mathcal{D}_i : \bar{\mathcal{S}}_{nn}^{\alpha\beta} + \bar{\mathcal{S}}_{nn}^{\alpha\beta} : \mathcal{D}_i - \right. \\ & \left. - \bar{\mathcal{S}}_{nn}^{\alpha\beta} : \left(\mathcal{D}_i : \bar{\mathcal{C}}^{\alpha\beta} : \mathcal{N} + \mathcal{N} : \bar{\mathcal{C}}^{\alpha\beta} : \mathcal{D}_i \right) : \bar{\mathcal{S}}_{nn}^{\alpha\beta} \right) : \Delta \Sigma^{\alpha\beta} h_\alpha h_\beta. \end{aligned}$$

Furthermore, by using the symmetry of the fourth-rank tensors

$$\begin{aligned} \mathcal{N} &= \mathcal{N}^T \\ \mathcal{D}_i &= \mathcal{D}_i^T \\ \mathcal{D}_i : \bar{\mathcal{C}}^{\alpha\beta} : \mathcal{N} &= (\mathcal{N} : \bar{\mathcal{C}}^{\alpha\beta} : \mathcal{D}_i)^T \end{aligned}$$

and of the second-rank stress and strain tensors $\mathbf{E} = \mathbf{E}^T$ and $\Sigma = \Sigma^T$, the previous formula for the variational derivative of the interpolated strain energy f_{el} , with respect to the normal component n_i , reduces to

$$\boxed{\frac{\partial f_{el}}{\partial n_i} = -\Delta \Sigma^{\alpha\beta} : \left(\mathcal{D}_i - \bar{\mathcal{S}}_{nn}^{\alpha\beta} : \mathcal{D}_i : \bar{\mathcal{C}}^{\alpha\beta} \right) : \Delta \bar{\mathbf{E}}^{\alpha\beta} h_\alpha h_\beta.}$$

Finally, and for completeness, if the normal vector \mathbf{n} is defined like in eq. (4.40), the derivative $\partial \mathbf{n} / \partial \nabla \phi_\alpha$ is given as a matrix

$$\frac{\partial \mathbf{n}}{\partial \nabla \phi_\alpha} = \frac{1}{|\nabla(\phi_\alpha - \phi_\beta)|} (\mathbf{1} - \mathbf{n} \otimes \mathbf{n}),$$

and the derivative of the elastic energy, with respect to the phase-field gradient $\nabla \phi_\alpha$, writes in a short form as

$$\boxed{\frac{\partial f_{el}}{\partial \nabla \phi_\alpha} = \frac{1}{|\nabla(\phi_\alpha - \phi_\beta)|} (\mathbf{1} - \Phi) \begin{pmatrix} \frac{\partial f_{el}}{\partial n_1} \\ \frac{\partial f_{el}}{\partial n_2} \\ \frac{\partial f_{el}}{\partial n_3} \end{pmatrix}.} \quad (4.43)$$

4.4.6. A short summary of the main equations

In this section, I want to summarise the main findings. Since the interpolated elastic energy

$$f_{el} = \frac{1}{2} \left((\mathbf{E} - \tilde{\mathbf{E}}^\alpha) : \Sigma^\alpha h_\alpha + (\mathbf{E} - \tilde{\mathbf{E}}^\beta) : \Sigma^\beta h_\beta - \Delta \Sigma^{\alpha\beta} : \Delta \bar{\mathbf{E}}^{\alpha\beta} h_\alpha h_\beta \right)$$

is given in dependency of the required system variables, using the variational principle, the Cauchy stress

$$\Sigma = \frac{\partial f_{el}}{\partial \mathbf{E}} = \Sigma^\alpha h_\alpha + \Sigma^\beta h_\beta - (\mathcal{C}^\alpha - \mathcal{C}^\beta) : \Delta \bar{\mathbf{E}}^{\alpha\beta} h_\alpha h_\beta$$

and the elastic driving force

$$\begin{aligned} \frac{\delta f_{el}}{\delta \phi_\alpha} = & \frac{1}{2} \left((\mathbf{E} - \tilde{\mathbf{E}}^\alpha) : \Sigma^\alpha - \Delta \bar{\mathbf{E}}^{\alpha\beta} : \mathcal{C}^\alpha : \Delta \bar{\mathbf{E}}^{\alpha\beta} h_\beta^2 \right) h'_\alpha - \\ & - \nabla \cdot \left(\frac{1}{|\nabla(\phi_\alpha - \phi_\beta)|} (\mathbf{1} - \Phi) \frac{\partial f_{el}}{\partial \mathbf{n}} \right) \end{aligned}$$

are given by the respective derivatives. The following shorthand notations are used

$$\begin{aligned} \mathbf{n} &= \frac{\nabla(\phi_\alpha - \phi_\beta)}{|\nabla(\phi_\alpha - \phi_\beta)|}, & \mathcal{N} &= \mathbf{1} \square \Phi + \Phi \square \mathbf{1} - \Phi \square \Phi, & \Phi &= \mathbf{n} \otimes \mathbf{n}, \\ \Sigma^\alpha &= \mathcal{C}^\alpha : (\mathbf{E} - \tilde{\mathbf{E}}^\alpha), & \Sigma^\beta &= \mathcal{C}^\beta : (\mathbf{E} - \tilde{\mathbf{E}}^\beta), & \Delta \Sigma^{\alpha\beta} &= \Sigma^\alpha - \Sigma^\beta, \\ \bar{\mathcal{C}}^{\alpha\beta} &= (\mathcal{C}^\alpha h_\beta + \mathcal{C}^\beta h_\alpha), & \bar{\mathcal{S}}_{nn}^{\alpha\beta} &= (\mathcal{N} : \bar{\mathcal{C}}^{\alpha\beta} : \mathcal{N})^+, & \Delta \bar{\mathbf{E}}^{\alpha\beta} &= \bar{\mathcal{S}}_{nn}^{\alpha\beta} : \Delta \Sigma^{\alpha\beta}, \\ i &= 1, 2, 3, & \frac{\partial f_{el}}{\partial \mathbf{n}} &= \left(\frac{\partial f_{el}}{\partial n_1}, \frac{\partial f_{el}}{\partial n_2}, \frac{\partial f_{el}}{\partial n_3} \right), & \mathcal{D}_i &= \frac{\partial \mathcal{N}}{\partial n_i}, \\ \frac{\partial f_{el}}{\partial n_i} &= \Delta \Sigma^{\alpha\beta} : \left(\mathcal{D}_i - \bar{\mathcal{S}}_{nn}^{\alpha\beta} : \mathcal{D}_i : \bar{\mathcal{C}}^{\alpha\beta} \right) : \Delta \bar{\mathbf{E}}^{\alpha\beta} h_\alpha h_\beta \end{aligned}$$

Retrospectively, there also exist alternative derivation steps, which will result in the same strain energy formulation, but which require fewer reformulations and mathematical manipulations.

In the next section, the important fields and quantities will be formulated in the closed form in the Voigt notation of the symmetric Cauchy stress and strain tensors.

4.5. Explicit formulation of the elastic fields in the Voigt notation

In the previous section, the interpolation type of the phase-dependent elastic energies in the diffuse interface between two transitional phases was presented. The basic assumptions for the thermodynamically consistent model are the mechanical jump conditions, which are valid on the coherent interface. Since the derivation was done in a general manner, with the strain and stress in a matrix form, the linear relation between the elastic strain and the Cauchy stress, due to Hooke's law, is given as a fourth-rank tensor, which is also known as stiffness and compliance tensor.

Under the assumption of the infinitesimal deformations of a continuum body, the second- and higher-order gradients of the displacement vector are neglected, and the strain tensor becomes symmetric. With the angular momentum balance, the Cauchy stress matrix is symmetric as well, and in this case the Voigt notation is well established for a more convenient usage.

Using the Voigt notation in all required fields, all assumptions and results of the new formalism in sec. 4.4 should be adopted. In order to differentiate the matrix form of the stress and strain tensors

$$\boldsymbol{\Sigma} = \begin{pmatrix} \Sigma_{11} & \Sigma_{12} & \Sigma_{13} \\ \Sigma_{12} & \Sigma_{22} & \Sigma_{23} \\ \Sigma_{13} & \Sigma_{23} & \Sigma_{33} \end{pmatrix} \quad \text{and} \quad \mathbf{E} = \begin{pmatrix} E_{11} & E_{12} & E_{13} \\ E_{12} & E_{22} & E_{23} \\ E_{13} & E_{23} & E_{33} \end{pmatrix}$$

and their respective Voigt stress and strain vectors [83], I will use capital or small letters

$$\begin{aligned} \boldsymbol{\varepsilon}^T &= (\varepsilon_1, \varepsilon_2, \varepsilon_3, \varepsilon_4, \varepsilon_5, \varepsilon_6) = (E_{11}, E_{22}, E_{33}, 2E_{23}, 2E_{13}, 2E_{12}), \\ \tilde{\boldsymbol{\varepsilon}}^T &= (\tilde{\varepsilon}_1, \tilde{\varepsilon}_2, \tilde{\varepsilon}_3, \tilde{\varepsilon}_4, \tilde{\varepsilon}_5, \tilde{\varepsilon}_6) = (\tilde{E}_{11}, \tilde{E}_{22}, \tilde{E}_{33}, 2\tilde{E}_{23}, 2\tilde{E}_{13}, 2\tilde{E}_{12}), \\ \boldsymbol{\sigma}^T &= (\sigma_1, \sigma_2, \sigma_3, \sigma_4, \sigma_5, \sigma_6) = (\Sigma_{11}, \Sigma_{22}, \Sigma_{33}, \Sigma_{23}, \Sigma_{13}, \Sigma_{12}), \end{aligned}$$

respectively.

Because of the reformulation of the stress and strain matrices into a vector form, the stiffness (compliance) fourth-rank tensors undergo the corresponding transformation. The components of the original fourth-rank stiffness (compliance) tensor are symmetric if the indices permute in the manner of [83, 84]

$$C_{ijkl} = C_{jikl} = C_{jilk} = C_{ijlk} = C_{klij} = C_{klji} = C_{lkji} = C_{lkij}.$$

With respect to the previous notation in the Voigt stress (strain), the corresponding stiffness tensor, as a matrix $\mathbf{C} \in \text{Sym}(6, 6; \mathbb{R})$, remains symmetric,

4.5. Explicit formulation of the elastic fields in the Voigt notation

and the matrix components c_{ij} correspond to the stiffness components due to the index map,

$$I : \{11, 22, 33, (23, 32), (13, 31), (12, 21)\} \mapsto \{1, 2, 3, 4, 5, 6\}, \quad (4.44)$$

with $\mathcal{C}_{ijkl} \rightarrow c_{I(ij)I(kl)}$. Therefore, the stiffness matrix writes as

$$\mathbf{C} = \begin{pmatrix} c_{11} & c_{12} & c_{13} & c_{14} & c_{15} & c_{16} \\ c_{12} & c_{22} & c_{23} & c_{24} & c_{25} & c_{26} \\ c_{13} & c_{23} & c_{33} & c_{34} & c_{35} & c_{36} \\ c_{14} & c_{24} & c_{34} & c_{44} & c_{45} & c_{46} \\ c_{15} & c_{25} & c_{35} & c_{45} & c_{55} & c_{56} \\ c_{16} & c_{26} & c_{36} & c_{46} & c_{56} & c_{66} \end{pmatrix},$$

and Hooke's law takes its usual form as a matrix vector product

$$\boldsymbol{\sigma} = \mathbf{C}(\boldsymbol{\varepsilon} - \tilde{\boldsymbol{\varepsilon}}). \quad (4.45)$$

The fourth-rank tensor \mathcal{N} in sec. 4.4.1 was used for the decomposition of the symmetric stress and strain tensors into their homogeneous and inhomogeneous constituents. Since the fourth-rank tensor in the tensorial notation was the same for both symmetric stress and strain matrices, following the different definitions of shear strain and shear stress in the Voigt notation, the corresponding projective matrices \mathbf{N}_ε and \mathbf{N}_σ differ. By evaluating the normal constituent of the strain and stress tensors $\mathcal{N} : \boldsymbol{\Sigma}$ and $\mathcal{N} : \mathbf{E}$, and by comparing the corresponding coefficients, both matrices are derived and write as

4. Phase-Field Models with Elasticity

$$\mathbf{N}_\sigma = \begin{pmatrix} n_1^2(2-n_1^2) & -n_1^2n_2^2 & -n_1^2n_3^2 & -2n_1^2n_2n_3 & 2n_1n_3(1-n_1^2) & 2n_1n_2(1-n_1^2) \\ -n_1^2n_2^2 & n_2^2(2-n_2^2) & -n_2^2n_3^2 & 2n_2n_3(1-n_2^2) & -2n_1n_3(1-n_1^2) & 2n_1n_2(1-n_2^2) \\ -n_1^2n_3^2 & -n_2^2n_3^2 & n_3^2(2-n_3^2) & 2n_2n_3(1-n_3^2) & 2n_1n_3(1-n_3^2) & -2n_1n_2n_3^2 \\ -n_1^2n_2n_3 & n_2n_3(1-n_2^2) & n_2n_3(1-n_3^2) & 1-n_1^2-2n_2^2n_3^2 & n_1n_2(1-2n_3^2) & n_1n_3(1-2n_2^2) \\ n_1n_3(1-n_1^2) & -n_1n_2n_3 & n_1n_3(1-n_3^2) & n_1n_2(1-2n_3^2) & 1-n_2^2-2n_1^2n_3^2 & n_2n_3(1-2n_1^2) \\ n_1n_2(1-n_1^2) & n_1n_2(1-n_2^2) & -n_1n_2n_3^2 & n_1n_3(1-2n_2^2) & n_2n_3(1-2n_1^2) & 1-n_3^2-2n_1^2n_2^2 \end{pmatrix}$$

and

$$\mathbf{N}_\epsilon = \begin{pmatrix} n_1^2(2-n_1^2) & -n_1^2n_2^2 & -n_1^2n_3^2 & -n_1^2n_2n_3 & n_1n_3(1-n_1^2) & n_1n_2(1-n_1^2) \\ -n_1^2n_2^2 & n_2^2(2-n_2^2) & -n_2^2n_3^2 & n_2n_3(1-n_2^2) & -n_1n_2n_3 & n_1n_2(1-n_2^2) \\ -n_1^2n_3^2 & -n_2^2n_3^2 & n_3^2(2-n_3^2) & n_2n_3(1-n_3^2) & n_1n_3(1-n_3^2) & -n_1n_2n_3^2 \\ -2n_1^2n_2n_3 & 2n_2n_3(1-n_2^2) & 2n_2n_3(1-n_3^2) & 1-n_1^2-2n_2^2n_3^2 & n_1n_2(1-2n_3^2) & n_1n_3(1-2n_2^2) \\ 2n_1n_3(1-n_1^2) & -2n_1n_2n_3 & 2n_1n_3(1-n_3^2) & n_1n_2(1-2n_3^2) & 1-n_2^2-2n_1^2n_3^2 & n_2n_3(1-2n_1^2) \\ 2n_1n_2(1-n_1^2) & 2n_1n_2(1-n_2^2) & -2n_1n_2n_3^2 & n_1n_3(1-2n_2^2) & n_2n_3(1-2n_1^2) & 1-n_3^2-2n_1^2n_2^2 \end{pmatrix}$$

4.5. Explicit formulation of the elastic fields in the Voigt notation

with the normal vector components $\mathbf{n} = (n_1, n_2, n_3)^T$. Both matrices are the transpositions of each other, $\mathbf{N}_\sigma^T = \mathbf{N}_\varepsilon$. Thus, the usage of only one matrix can be applied in the further derivations, here \mathbf{N}_σ .

In the next preliminary derivation step, I respecify the properties of the pseudo inverse, which should be satisfied in the Voigt notation. As mentioned, the left and right projective matrices are different, $\mathbf{N}_\sigma \neq \mathbf{N}_\varepsilon$, and thus the corresponding stiffness tensor to \mathbf{C}_{nn} , in eq. (4.21), is written as

$$\mathbf{C}_{nn} = \mathbf{N}_\sigma \mathbf{C} \mathbf{N}_\varepsilon = \mathbf{N}_\sigma \mathbf{C} \mathbf{N}_\sigma^T. \quad (4.46)$$

While I use the same notation for the normal stiffness tensors like in the previous model in sec. 4.3.3, where it was a 3×3 matrix, now, in the current situation, it is a 6×6 matrix. Obviously, the resulting matrix \mathbf{C}_{nn} is symmetric. Therefore, the pseudo inverse \mathbf{S}_{nn} should also be quadratic and symmetric, $\mathbf{S}_{nn} = \mathbf{S}_{nn}^T$, see eq. (4.22), but because of different projective matrices, the left and the right products of \mathbf{C}_{nn} , with the pseudo inverse \mathbf{S}_{nn} , are different

$$\mathbf{S}_{nn} \mathbf{C}_{nn} = \mathbf{N}_\varepsilon \quad \text{and} \quad \mathbf{C}_{nn} \mathbf{S}_{nn} = \mathbf{N}_\sigma. \quad (4.47)$$

Furthermore, the invariance with the left and right matrix product, with \mathbf{N}_ε and \mathbf{N}_σ , respectively writes as

$$\mathbf{S}_{nn} \mathbf{N}_\sigma = \mathbf{S}_{nn} = \mathbf{N}_\varepsilon \mathbf{S}_{nn}. \quad (4.48)$$

This requirement corresponds to the assumption in eq. (4.23) in the general formalism.

In order to give the explicit form of the pseudo inverse, I will present the relevant findings of the detailed examination of the projection matrix \mathbf{N}_σ . First of all, it is straightforward to determine the rank of the matrix \mathbf{N}_σ to be

$$\text{rank}(\mathbf{N}_\sigma) = \text{rank}(\mathbf{N}_\varepsilon) = 3.$$

The dimension of the quadratic matrix \mathbf{N}_σ is 6×6 , and its rank is lower than the number of its rows and columns. Therefore, applying the theorems of the linear algebra, there exist matrices $\mathbf{A} \in \mathbb{R}^{6 \times 3}$ and $\mathbf{B} \in \mathbb{R}^{3 \times 6}$, the product of which results in the original matrix

$$\mathbf{N}_\sigma = \mathbf{A} \mathbf{B}. \quad (4.49)$$

Since the determination of these matrices can be done with the singular value determination, the desired matrices have been found by trial to be

$$\mathbf{A} = \begin{pmatrix} n_1(2 - n_1^2) & -n_1^2 n_2 & -n_1^2 n_3 \\ -n_1 n_2^2 & n_2(2 - n_2^2) & -n_2^2 n_3 \\ -n_1 n_3^2 & -n_3^2 n_2 & n_3(2 - n_3^2) \\ -n_1 n_2 n_3 & n_3(1 - n_2^2) & n_2(1 - n_3^2) \\ n_3(1 - n_1^2) & -n_1 n_2 n_3 & n_1(1 - n_3^2) \\ n_2(1 - n_1^2) & n_1(1 - n_2^2) & -n_1 n_2 n_3 \end{pmatrix} \quad (4.50)$$

4. Phase-Field Models with Elasticity

and

$$\mathbf{B} = \begin{pmatrix} n_1 & 0 & 0 & 0 & n_3 & n_2 \\ 0 & n_2 & 0 & n_3 & 0 & n_1 \\ 0 & 0 & n_3 & n_2 & n_1 & 0 \end{pmatrix}. \quad (4.51)$$

A further useful property of both matrices is that their other product results in the 3×3 unity matrix

$$\mathbf{B}\mathbf{A} = \mathbf{A}^T\mathbf{B}^T = \mathbf{1}, \quad (4.52)$$

whereby the property $n_1^2 + n_2^2 + n_3^2 = 1$ was used. Therefore, the idempotence of \mathbf{N}_σ , and consequently its projective property, follows immediately using the product in eq. (4.49)

$$\mathbf{N}_\sigma\mathbf{N}_\sigma = \mathbf{A}\mathbf{B}\mathbf{A}\mathbf{B} = \mathbf{A}\underbrace{\mathbf{B}\mathbf{A}}_{\mathbf{1}}\mathbf{B} = \mathbf{A}\mathbf{B} = \mathbf{N}_\sigma,$$

and the matrix \mathbf{C}_{nn} in eq. (4.46) rewrites to

$$\mathbf{C}_{nn} = \mathbf{A}\mathbf{B}\mathbf{C}\mathbf{B}^T\mathbf{A}^T.$$

Note that the matrix $\mathbf{B}\mathbf{C}\mathbf{B}^T \in \mathbb{R}^{3 \times 3}$ inside the product is a symmetric regular matrix.

By trial approach for the pseudo inverse matrix as

$$\boxed{\mathbf{S}_{nn} = \mathbf{B}^T(\mathbf{B}\mathbf{C}\mathbf{B}^T)^{-1}\mathbf{B}}, \quad (4.53)$$

all assumed properties are fulfilled.

The symmetry of the matrix \mathbf{S}_{nn} is trivial to show. The invariance with the left and right products with the appropriate projection in eq. (4.48), follows by using the product in eq. (4.52)

$$\mathbf{N}_\varepsilon\mathbf{S}_{nn} = \mathbf{B}^T\underbrace{\mathbf{A}^T\mathbf{B}^T}_{\mathbf{1}}(\mathbf{B}\mathbf{C}\mathbf{B}^T)^{-1}\mathbf{B} = \mathbf{B}^T(\mathbf{B}\mathbf{C}\mathbf{B}^T)^{-1}\mathbf{B} = \mathbf{S}_{nn}$$

$$\mathbf{S}_{nn}\mathbf{N}_\sigma = \mathbf{B}^T(\mathbf{B}\mathbf{C}\mathbf{B}^T)^{-1}\underbrace{\mathbf{B}\mathbf{A}}_{\mathbf{1}}\mathbf{B} = \mathbf{B}^T(\mathbf{B}\mathbf{C}\mathbf{B}^T)^{-1}\mathbf{B} = \mathbf{S}_{nn}.$$

The products with the normal stiffness matrix \mathbf{C}_{nn} write as

$$\begin{aligned} \mathbf{C}_{nn}\mathbf{S}_{nn} &= \mathbf{A}\mathbf{B}\mathbf{C}\mathbf{B}^T\underbrace{\mathbf{A}^T\mathbf{B}^T}_{\mathbf{1}}(\mathbf{B}\mathbf{C}\mathbf{B}^T)^{-1}\mathbf{B} = \\ &= \mathbf{A}\underbrace{(\mathbf{B}\mathbf{C}\mathbf{B}^T)(\mathbf{B}\mathbf{C}\mathbf{B}^T)^{-1}}_{\mathbf{1}}\mathbf{B} = \mathbf{A}\mathbf{B} = \mathbf{N}_\sigma \end{aligned}$$

$$\begin{aligned} \mathbf{S}_{nn}\mathbf{C}_{nn} &= \mathbf{B}^T(\mathbf{B}\mathbf{C}\mathbf{B}^T)^{-1}\underbrace{\mathbf{B}\mathbf{A}}_{\mathbf{1}}\mathbf{B}\mathbf{C}\mathbf{B}^T\mathbf{A}^T = \\ &= \mathbf{B}^T\underbrace{(\mathbf{B}\mathbf{C}\mathbf{B}^T)^{-1}\mathbf{B}\mathbf{C}\mathbf{B}^T}_{\mathbf{1}}\mathbf{A}^T = \mathbf{B}^T\mathbf{A}^T = \mathbf{N}_\varepsilon, \end{aligned}$$

4.5. Explicit formulation of the elastic fields in the Voigt notation

and finally, the matrix in eq. (4.53) is the searched pseudo inverse matrix with the assumed properties, which is already written with respect to the Voigt notation of the strain and Cauchy stress.

What is remarkable is the product between the Voigt stress and the matrix \mathbf{B} , which results in the original traction vector

$$\mathbf{B}\boldsymbol{\sigma} = \begin{pmatrix} \sigma_1 n_1 + \sigma_6 n_2 + \sigma_5 n_3 \\ \sigma_6 n_1 + \sigma_2 n_2 + \sigma_4 n_3 \\ \sigma_5 n_1 + \sigma_4 n_2 + \sigma_2 n_3 \end{pmatrix} = \begin{pmatrix} \Sigma_{11} n_1 + \Sigma_{12} n_2 + \Sigma_{13} n_3 \\ \Sigma_{12} n_1 + \Sigma_{22} n_2 + \Sigma_{23} n_3 \\ \Sigma_{13} n_1 + \Sigma_{23} n_2 + \Sigma_{33} n_3 \end{pmatrix} = \boldsymbol{\Sigma} \mathbf{n}.$$

Thus, the former expressions of the elastic energy, the stress and the driving force are expressed using the sparse matrix \mathbf{B} . Using the definitions of the phase-dependent stresses again, but noted as $\boldsymbol{\sigma}^\alpha = \mathbf{C}^\alpha(\boldsymbol{\varepsilon} - \tilde{\boldsymbol{\varepsilon}}^\alpha)$, the interpolated strain energy in eq (4.35), with Voigt stress and strain, writes as

$$f_{el}(\phi, \boldsymbol{\varepsilon}) = \frac{1}{2} \left[\langle \boldsymbol{\varepsilon} - \tilde{\boldsymbol{\varepsilon}}^\alpha, \boldsymbol{\sigma}^\alpha \rangle h_\alpha + \langle \boldsymbol{\varepsilon} - \tilde{\boldsymbol{\varepsilon}}^\beta, \boldsymbol{\sigma}^\beta \rangle h_\beta - \langle \mathbf{B}(\boldsymbol{\sigma}^\alpha - \boldsymbol{\sigma}^\beta), (\mathbf{B}\bar{\mathbf{C}}^{\alpha\beta}\mathbf{B}^T)^{-1}\mathbf{B}(\boldsymbol{\sigma}^\alpha - \boldsymbol{\sigma}^\beta) \rangle h_\alpha h_\beta \right],$$

with an asymmetrically interpolated stiffness tensor $\bar{\mathbf{C}}^{\alpha\beta} = \mathbf{C}^\alpha h_\beta + \mathbf{C}^\beta h_\alpha$. The big chevrons $\langle \cdot, \cdot \rangle$ sign the dot product of six-dimensional strain and stress vectors, and the small chevrons $\langle \cdot, \cdot \rangle$ represent a usual inner product in the three-dimensional Euclidean³ space. By the introduction of the shorthand notation, like in the stress equation 4.36, the difference of the phase-dependent stresses is signed as

$$\Delta\boldsymbol{\sigma}^{\alpha\beta} = \boldsymbol{\sigma}^\alpha - \boldsymbol{\sigma}^\beta.$$

Note that the matrix vector product

$$B\Delta\boldsymbol{\sigma}^{\alpha\beta} = \Delta\boldsymbol{\Sigma}^{\alpha\beta} \mathbf{n}^{\alpha\beta}$$

corresponds to the jump of phase-dependent normal stresses. Further, in similarity to the introduced abbreviations in sec. 4.4.6, I use the shorthand notation for the following strain jump

$$\Delta\tilde{\boldsymbol{\varepsilon}}_{nn}^{\alpha\beta} = \mathbf{B}^T (\mathbf{B}\bar{\mathbf{C}}^{\alpha\beta}\mathbf{B}^T)^{-1} \mathbf{B}(\boldsymbol{\sigma}^\alpha - \boldsymbol{\sigma}^\beta)$$

and rewrite the interpolated strain energy in the diffuse interface as a sum of scalar products

$$\boxed{f_{el}(\phi, \boldsymbol{\varepsilon}) = \frac{1}{2} \left[\langle \boldsymbol{\varepsilon} - \tilde{\boldsymbol{\varepsilon}}^\alpha, \boldsymbol{\sigma}^\alpha \rangle h_\alpha + \langle \boldsymbol{\varepsilon} - \tilde{\boldsymbol{\varepsilon}}^\beta, \boldsymbol{\sigma}^\beta \rangle h_\beta - \langle \Delta\boldsymbol{\sigma}^{\alpha\beta}, \Delta\tilde{\boldsymbol{\varepsilon}}_{nn}^{\alpha\beta} \rangle h_\alpha h_\beta \right].} \quad (4.54)$$

³Euclid of Alexandria, fl. 300 BCE, Greek mathematician. He is often referred to as the "father of geometry".

4. Phase-Field Models with Elasticity

The interfacial stress in the Voigt notation is derived by the derivative of the strain energy, with respect to the Voigt strain, and, in accordance with eq. (4.36), writes as

$$\sigma = \sigma^\alpha h_\alpha + \sigma^\beta h_\beta - (\mathbf{C}^\alpha - \mathbf{C}^\beta) \Delta \bar{\varepsilon}_{nn}^{\alpha\beta} h_\alpha h_\beta. \quad (4.55)$$

As mentioned for two phases with the same stiffness matrices, but with different eigenstrains, the previous formula reduces to the stress with the Voigt interpolation type.

The elastic driving force results from the first variation of the elastic energy, with respect to the phase-field function, and consists of two parts. The variational derivative, with respect to the phase field-variable ϕ_α , is given as

$$\frac{\partial f_{el}}{\partial \phi_\alpha} = \frac{1}{2} \left(\langle \varepsilon - \bar{\varepsilon}^\alpha, \sigma^\alpha \rangle - \langle \Delta \bar{\varepsilon}_{nn}^{\alpha\beta}, \mathbf{C}^\alpha \Delta \bar{\varepsilon}_{nn}^{\alpha\beta} \rangle h_\beta^2 \right) h'_\alpha, \quad (4.56)$$

whereby the variational derivative of the elastic energy, with respect to the phase field gradient $\nabla \phi_\alpha$, is

$$\frac{\partial f_{el}}{\partial \nabla \phi_\alpha} = \frac{\partial \mathbf{n}}{\partial \nabla \phi_\alpha} \frac{\partial f_{el}}{\partial \mathbf{n}} = \frac{\partial \mathbf{n}}{\partial \nabla \phi_\alpha} = \frac{1}{|\nabla(\phi_\alpha - \phi_\beta)|} (\mathbf{1} - \mathbf{n} \otimes \mathbf{n}) \begin{pmatrix} \frac{\partial f_{el}}{\partial n_1} \\ \frac{\partial f_{el}}{\partial n_2} \\ \frac{\partial f_{el}}{\partial n_3} \end{pmatrix}. \quad (4.57)$$

The previous equation (4.57) can be simplified.

In the next step, I explicitly write the variational derivative of the strain energy, with respect to the components of the normal vector. For this purpose, I define the derivative matrices

$$\mathbf{D}_i = \frac{\partial \mathbf{B}}{\partial n_i}, \quad i = 1, 2, 3,$$

given explicitly as

$$\mathbf{D}_1^T = \begin{pmatrix} 1 & 0 & 0 \\ 0 & 0 & 0 \\ 0 & 0 & 0 \\ 0 & 0 & 0 \\ 0 & 0 & 1 \\ 0 & 1 & 0 \end{pmatrix}, \quad \mathbf{D}_2^T = \begin{pmatrix} 0 & 0 & 0 \\ 0 & 1 & 0 \\ 0 & 0 & 0 \\ 0 & 0 & 1 \\ 0 & 0 & 0 \\ 1 & 0 & 0 \end{pmatrix}, \quad \mathbf{D}_3^T = \begin{pmatrix} 0 & 0 & 0 \\ 0 & 0 & 0 \\ 0 & 0 & 1 \\ 0 & 1 & 0 \\ 1 & 0 & 0 \\ 0 & 0 & 0 \end{pmatrix},$$

and remark a useful relation with the original matrix \mathbf{B}

$$\mathbf{B} = n_1 \mathbf{D}_1 + n_2 \mathbf{D}_2 + n_3 \mathbf{D}_3.$$

4.5. Explicit formulation of the elastic fields in the Voigt notation

Therefore, the derivative of the pseudo inverse matrix, with respect to the i -th normal component, is given by

$$\begin{aligned}\frac{\partial \bar{\mathbf{S}}_{nn}^{\alpha\beta}}{\partial n_i} &= \frac{\partial}{\partial n_i} (\mathbf{B}^T (\mathbf{B} \bar{\mathbf{C}}^{\alpha\beta} \mathbf{B}^T)^{-1} \mathbf{B}) = \\ &= \mathbf{D}_i^T (\mathbf{B} \bar{\mathbf{C}}^{\alpha\beta} \mathbf{B}^T)^{-1} \mathbf{B} + \mathbf{B}^T (\mathbf{B} \bar{\mathbf{C}}^{\alpha\beta} \mathbf{B}^T)^{-1} \mathbf{D}_i^T - \\ &\quad - \mathbf{B}^T (\mathbf{B} \bar{\mathbf{C}}^{\alpha\beta} \mathbf{B}^T)^{-1} (\mathbf{D}_i \bar{\mathbf{C}}^{\alpha\beta} \mathbf{B}^T + \mathbf{B} \bar{\mathbf{C}}^{\alpha\beta} \mathbf{D}_i^T) (\mathbf{B} \bar{\mathbf{C}}^{\alpha\beta} \mathbf{B}^T)^{-1} \mathbf{B}.\end{aligned}$$

For a later simplification, I consider the following summation and use the derived expression in the previous two equations to get

$$\frac{\partial \bar{\mathbf{S}}_{nn}^{\alpha\beta}}{\partial n_1} n_1 + \frac{\partial \bar{\mathbf{S}}_{nn}^{\alpha\beta}}{\partial n_2} n_2 + \frac{\partial \bar{\mathbf{S}}_{nn}^{\alpha\beta}}{\partial n_2} n_2 = 2(\bar{\mathbf{S}}_{nn}^{\alpha\beta} - \bar{\mathbf{S}}_{nn}^{\alpha\beta} \bar{\mathbf{C}}^{\alpha\beta} \bar{\mathbf{S}}_{nn}^{\alpha\beta}).$$

But because the pseudo inverse is invariant under the left and right products with \mathbf{N}_ϵ and \mathbf{N}_σ , respectively, the right-hand side of the foregoing equation can be modified

$$\begin{aligned}2(\bar{\mathbf{S}}_{nn}^{\alpha\beta} - \bar{\mathbf{S}}_{nn}^{\alpha\beta} \bar{\mathbf{C}}^{\alpha\beta} \bar{\mathbf{S}}_{nn}^{\alpha\beta}) &= 2(\bar{\mathbf{S}}_{nn}^{\alpha\beta} - \bar{\mathbf{S}}_{nn}^{\alpha\beta} \underbrace{\mathbf{N}_\sigma \bar{\mathbf{C}}^{\alpha\beta} \mathbf{N}_\epsilon}_{\bar{\mathbf{C}}_{nn}^{\alpha\beta}} \bar{\mathbf{S}}_{nn}^{\alpha\beta}) = \\ &= 2(\bar{\mathbf{S}}_{nn}^{\alpha\beta} - \bar{\mathbf{S}}_{nn}^{\alpha\beta} \underbrace{\bar{\mathbf{C}}_{nn}^{\alpha\beta} \bar{\mathbf{S}}_{nn}^{\alpha\beta}}_{\mathbf{N}_\sigma}) = 2(\bar{\mathbf{S}}_{nn}^{\alpha\beta} - \bar{\mathbf{S}}_{nn}^{\alpha\beta}) = \mathbf{O}\end{aligned}$$

to the zero matrix \mathbf{O} . Therefore, the vector matrix product in eq. (4.57)

$$(\mathbf{1} - \mathbf{n} \otimes \mathbf{n}) \frac{\partial f_{el}}{\partial \mathbf{n}} = \frac{\partial f_{el}}{\partial \mathbf{n}} - \langle \mathbf{n}, \frac{\partial f_{el}}{\partial \mathbf{n}} \rangle \mathbf{n}$$

can be rewritten in such a manner that the scalar product

$$\begin{aligned}\left\langle \frac{\partial f_{el}}{\partial \mathbf{n}}, \mathbf{n} \right\rangle &= -\frac{1}{2} \sum_{i=1}^3 \left\langle \Delta \sigma^{\alpha\beta}, \frac{\partial \bar{\mathbf{S}}_{nn}^{\alpha\beta}}{\partial n_i} \Delta \sigma^{\alpha\beta} \right\rangle n_i = \\ &= -\frac{1}{2} \left\langle \Delta \sigma^{\alpha\beta}, \underbrace{\left(\sum_{i=1}^3 \frac{\partial \bar{\mathbf{S}}_{nn}^{\alpha\beta}}{\partial n_i} n_i \right)}_{\mathbf{O}} \Delta \sigma^{\alpha\beta} \right\rangle = 0.\end{aligned}$$

vanishes. It means nothing, but that the derivative of the elastic energy, with respect to the interface orientation, which is given by the normal vector, is perpendicular to the interface orientation and is lying in the tangential plane.

Finally, the derivative of the elastic energy, with respect to the phase-field gra-

4. Phase-Field Models with Elasticity

gradient $\nabla\phi_\alpha$, simplifies to

$$\boxed{\begin{aligned} \frac{\partial f_{el}}{\partial \nabla\phi_\alpha} &= \frac{1}{|\nabla(\phi_\alpha - \phi_\beta)|} \begin{pmatrix} \frac{\partial f_{el}}{\partial n_1} \\ \frac{\partial f_{el}}{\partial n_2} \\ \frac{\partial f_{el}}{\partial n_3} \end{pmatrix}, & \text{with} \\ \frac{\partial f_{el}}{\partial n_i} &= \left\langle \bar{\mathbf{C}}^{\alpha\beta} \Delta \bar{\boldsymbol{\varepsilon}}_{nn}^{\alpha\beta} - \Delta \boldsymbol{\sigma}^{\alpha\beta}, \mathbf{D}_i^T (\mathbf{B} \bar{\mathbf{C}}^{\alpha\beta} \mathbf{B}^T)^{-1} \mathbf{B} \Delta \boldsymbol{\sigma}^{\alpha\beta} \right\rangle h_\alpha h_\beta. \end{aligned}} \quad (4.58)$$

4.5.1. Simplifications for the elastic isotropic materials

In the case of the elastic isotropic materials, the stiffness matrix can be rewritten with only two independent elastic constants. In the further derivations, I will use the first Lamé constant λ , the shear modulus G and sometimes the longitudinal modulus M for the shorthand notation of the resulting formulas. The chosen constants relate to the isotropic Young modulus E and to the isotropic Poisson ratio ν as follows:

$$\begin{aligned} \lambda &= \frac{E\nu}{(1-2\nu)(1+\nu)}, & G &= \frac{E}{2(1+\nu)}, \\ M &= \lambda + 2G = \frac{E(1-\nu)}{(1-2\nu)(1+\nu)}. \end{aligned}$$

Thus, a stiffness tensor writes as a sparse matrix

$$C = \begin{pmatrix} M & \lambda & \lambda & 0 & 0 & 0 \\ \lambda & M & \lambda & 0 & 0 & 0 \\ \lambda & \lambda & M & 0 & 0 & 0 \\ 0 & 0 & 0 & G & 0 & 0 \\ 0 & 0 & 0 & 0 & G & 0 \\ 0 & 0 & 0 & 0 & 0 & G \end{pmatrix}.$$

In the case of isotropic materials, the derived formulas for the stress calculation as well as for the driving forces can be simplified significantly for an efficient numerical calculation. Knowing the total strain as a symmetrised displacement gradient, the preliminary elastic strains for every phase are calculated,

$$\boldsymbol{\varepsilon}_{el}^\alpha = \boldsymbol{\varepsilon} - \tilde{\boldsymbol{\varepsilon}}^\alpha.$$

Note that this elastic strain does not correspond to the phase-dependent elastic strain, which is the argument of the phase-dependent elastic energy in eq. (4.25). The previous elastic strain definition is used to calculate the stresses for every

4.5. Explicit formulation of the elastic fields in the Voigt notation

phase, which are in accordance with the Voigt homogenisation scheme, and which for elastic isotropic material can be written as

$$\sigma_i^\alpha = \begin{cases} \lambda^\alpha (\varepsilon_{el1}^\alpha + \varepsilon_{el2}^\alpha + \varepsilon_{el3}^\alpha) + G^\alpha \varepsilon_{eli}^\alpha & i = 1, 2, 3, \\ G^\alpha \varepsilon_{eli}^\alpha & i = 4, 5, 6. \end{cases} \quad (4.59)$$

Remark that a linear combination of elastic isotropic stiffness tensors, for example in the interface as

$$\bar{\mathbf{C}}^{\alpha\beta} = \mathbf{C}^\alpha h_\beta + \mathbf{C}^\beta h_\alpha$$

or

$$\Delta \mathbf{C}^{\alpha\beta} = \mathbf{C}^\alpha - \mathbf{C}^\beta,$$

remains isotropic with the appropriate constants

$$\begin{aligned} \bar{M}^{\alpha\beta} &= M^\alpha h_\beta + M^\beta h_\alpha, & \bar{\lambda}^{\alpha\beta} &= \lambda^\alpha h_\beta + \lambda^\beta h_\alpha, & \bar{G}^{\alpha\beta} &= G^\alpha h_\beta + G^\beta h_\alpha, \\ \Delta M^{\alpha\beta} &= M^\alpha - M^\beta, & \Delta \lambda^{\alpha\beta} &= \lambda^\alpha - \lambda^\beta, & \Delta G^{\alpha\beta} &= G^\alpha - G^\beta, \end{aligned}$$

respectively. Therefore, relevant simplifications can be performed by the calculation of the pseudo inverse, which was derived in the Voigt notation in eq. (4.53), and writes as

$$\bar{\mathbf{S}}_{nn}^{\alpha\beta} = \mathbf{B}^T (\mathbf{B} \bar{\mathbf{C}}^{\alpha\beta} \mathbf{B}^T)^{-1} \mathbf{B}.$$

It is meaningful to write the regular matrix $\mathbf{B} \bar{\mathbf{C}}^{\alpha\beta} \mathbf{B}^T$ explicitly, which results after the straightforward evaluation in

$$\mathbf{B} \bar{\mathbf{C}}^{\alpha\beta} \mathbf{B}^T = \bar{M}^{\alpha\beta} \Phi + \bar{G}^{\alpha\beta} (\mathbf{1} - \Phi). \quad (4.60)$$

The projection matrix Φ is given as a dyadic product of the normal vectors $\Phi = \mathbf{n} \otimes \mathbf{n}$; consequently, the inverse of the foregoing matrix can be given directly as

$$(\mathbf{B} \bar{\mathbf{C}}^{\alpha\beta} \mathbf{B}^T)^{-1} = \left(\bar{M}^{\alpha\beta} \Phi + \bar{G}^{\alpha\beta} (\mathbf{1} - \Phi) \right)^{-1} = \frac{1}{\bar{M}^{\alpha\beta}} \Phi + \frac{1}{\bar{G}^{\alpha\beta}} (\mathbf{1} - \Phi), \quad (4.61)$$

and the determination of the pseudo inverse does not require any matrix inversion, but simplifies to the direct form, which is written with reciprocal elastic constants

$$\bar{\mathbf{S}}_{nn}^{\alpha\beta} = \mathbf{B}^T \left(\frac{1}{\bar{M}^{\alpha\beta}} \Phi + \frac{1}{\bar{G}^{\alpha\beta}} (\mathbf{1} - \Phi) \right) \mathbf{B}. \quad (4.62)$$

Efficient stress calculation

Firstly, it is more convenient to split the outer matrices \mathbf{B}^T and \mathbf{B} from the pseudo inverse and to consider the vector matrix product $\mathbf{B} \Delta \sigma^{\alpha\beta}$. Remember the mentioned relation between the different notations. By taking this into

4. Phase-Field Models with Elasticity

account, the product in the Voigt notation results in the jump of the corresponding stresses $\Delta \Sigma^{\alpha\beta} \mathbf{n}$, which is written in tensorial notation of Cauchy stress and which up to now is signed with $\Delta \sigma_n^{\alpha\beta}$

$$\Delta \sigma_n^{\alpha\beta} = \mathbf{B} \Delta \sigma^{\alpha\beta} = \begin{pmatrix} \sum_{k=1}^3 n_k \Delta \sigma_{I(1k)}^{\alpha\beta} \\ \sum_{k=1}^3 n_k \Delta \sigma_{I(2k)}^{\alpha\beta} \\ \sum_{k=1}^3 n_k \Delta \sigma_{I(3k)}^{\alpha\beta} \end{pmatrix} = \begin{pmatrix} \sum_{k=1}^3 n_k \Delta \Sigma_{1k}^{\alpha\beta} \\ \sum_{k=1}^3 n_k \Delta \Sigma_{2k}^{\alpha\beta} \\ \sum_{k=1}^3 n_k \Delta \Sigma_{3k}^{\alpha\beta} \end{pmatrix} = \Delta \Sigma^{\alpha\beta} \mathbf{n}. \quad (4.63)$$

In the previous relation, I used the map $I(jk)$ of the underscore change from tensor to vector notation, which is explicitly given in (4.44), and therefore is to be beneficial.

Since I split the pseudo inverse into its constituents and use the associativity of the vector matrix multiplications, I consider the product in the stress calculation in eq. (4.55), between the matrix \mathbf{B}^T and the stiffness difference $(\mathbf{C}^\alpha - \mathbf{C}^\beta)$. Thus, the direct evaluation of the products yields

$$(\mathbf{C}^\alpha - \mathbf{C}^\beta) \mathbf{B}^T = \Delta \lambda^{\alpha\beta} \begin{pmatrix} n_1 & n_2 & n_3 \\ n_1 & n_2 & n_3 \\ n_1 & n_2 & n_3 \\ 0 & 0 & 0 \\ 0 & 0 & 0 \\ 0 & 0 & 0 \end{pmatrix} + \Delta G^{\alpha\beta} \begin{pmatrix} 2n_1 & 0 & 0 \\ 0 & 2n_2 & 0 \\ 0 & 0 & 2n_3 \\ 0 & n_3 & n_2 \\ n_3 & 0 & n_1 \\ n_2 & n_1 & 0 \end{pmatrix},$$

with the matrices which only depend on the normal vector components, and which are scaled with the differences in the appropriate Lamé constants. Further, by considering the matrix product $\Delta \mathbf{C}^{\alpha\beta} \mathbf{B}^T (\mathbf{B} \bar{\mathbf{C}}^{\alpha\beta} \mathbf{B}^T)^{-1}$ in the stress calculation

$$\boldsymbol{\sigma} = \boldsymbol{\sigma}^\alpha h_\alpha + \boldsymbol{\sigma}^\beta h_\beta - \Delta \mathbf{C}^{\alpha\beta} \mathbf{B}^T (\mathbf{B} \bar{\mathbf{C}}^{\alpha\beta} \mathbf{B}^T)^{-1} \Delta \sigma_n^{\alpha\beta} h_\alpha h_\beta,$$

it results in the following matrix addition

$$\Delta \mathbf{C}^{\alpha\beta} \mathbf{B}^T (\mathbf{B} \bar{\mathbf{C}}^{\alpha\beta} \mathbf{B}^T)^{-1} = \frac{\Delta \lambda^{\alpha\beta}}{\bar{M}^{\alpha\beta}} \begin{pmatrix} n_1 & n_2 & n_3 \\ n_1 & n_2 & n_3 \\ n_1 & n_2 & n_3 \\ 0 & 0 & 0 \\ 0 & 0 & 0 \\ 0 & 0 & 0 \end{pmatrix} + \frac{\Delta G^{\alpha\beta}}{\bar{G}^{\alpha\beta}} \begin{pmatrix} 2n_1 & 0 & 0 \\ 0 & 2n_2 & 0 \\ 0 & 0 & 2n_3 \\ 0 & n_3 & n_2 \\ n_3 & 0 & n_1 \\ n_2 & n_1 & 0 \end{pmatrix} \\ + 2\Delta G^{\alpha\beta} \left(\frac{1}{\bar{M}^{\alpha\beta}} - \frac{1}{\bar{G}^{\alpha\beta}} \right) \begin{pmatrix} n_1^3 & n_1^2 n_2 & n_1^2 n_3 \\ n_1 n_2^2 & n_2^3 & n_2^2 n_3 \\ n_1 n_2^2 & n_2 n_3^2 & n_3^3 \\ n_1 n_2 n_3 & n_2^2 n_3 & n_2 n_3^2 \\ n_1^2 n_3 & n_1 n_2 n_3 & n_1 n_3^2 \\ n_1^2 n_2 & n_1 n_2^2 & n_1 n_2 n_3 \end{pmatrix}$$

4.5. Explicit formulation of the elastic fields in the Voigt notation

whereby the matrices are scaled with the coefficients which depend on the phase field functions ($\bar{M}^{\alpha\beta} = M^\alpha h_\beta + M^\beta h_\alpha$) and on differences in the elastic constants. For a shorthand notation, and also for the implementation, the introduction of the constants

$$J_2^{\alpha\beta} = \frac{\lambda^\alpha - \lambda^\beta}{M^\alpha h_\beta + M^\beta h_\alpha}, \quad J_4^{\alpha\beta} = \frac{G^\alpha - G^\beta}{G^\alpha h_\beta + G^\beta h_\alpha}$$

$$\bar{J}^{\alpha\beta} = 2\left(\frac{G^\alpha - G^\beta}{M^\alpha h_\beta + M^\beta h_\alpha} - J_4^{\alpha\beta}\right)$$

optimises the computational calculation. Finally, the cumbersome evaluation of the stress components can be given in the explicit manner and in a simplified form as

$$\sigma_i = \sigma_i^\alpha h_\alpha + \sigma_i^\beta h_\beta - h_\alpha h_\beta \sum_{j=1}^3 (J_2^{\alpha\beta} + \bar{J}^{\alpha\beta} n_i^2 + \delta_{ij} J_4^{\alpha\beta}) n_j (\Delta \sigma_n^{\alpha\beta})_j,$$

for the orthogonal normal stresses σ_1, σ_2 and σ_3 , and in a more tricky form for the orthogonal shear stresses σ_4, σ_5 and σ_6 , together with the applied, reduced indices $k = i - 3$ and $m = 9 - i - j$, as

$$\sigma_i = \sigma_i^\alpha h_\alpha + \sigma_i^\beta h_\beta - \sum_{j=1}^3 (\delta_{kj} \bar{J}^{\alpha\beta} n_1 n_2 n_3 + n_m (1 - \delta_{kj}) (J_4^{\alpha\beta} n_j^2 + J_4^{\alpha\beta})) (\Delta \sigma_n^{\alpha\beta})_j.$$

In both preceding formulas, I use a Kronecker⁴ delta

$$\delta_{ij} = \begin{cases} 1 & i = j, \\ 0 & i \neq j. \end{cases}$$

Efficient calculation of the elastic driving force

The expressions for the variational derivatives (4.56) and (4.57) can also be simplified for isotropic materials. Using the expression for the pseudo inverse in eq. (4.62), the first term writes as

$$\frac{\partial f_{el}}{\partial \phi_\alpha} = \frac{1}{2} \left[\langle \sigma^\alpha, \varepsilon_{el}^\alpha \rangle - \langle \Delta \sigma_n^{\alpha\beta}, \left(\frac{M^\alpha}{(\bar{M}^{\alpha\beta})^2} \Phi + \frac{G^\alpha}{(\bar{G}^{\alpha\beta})^2} (1 - \Phi) \right) \Delta \sigma_n^{\alpha\beta} \rangle h_\beta^2 \right] h'_\alpha.$$

Using the equivalences of the normal stress difference in eq. (4.63) for the auxiliary stresses, which are evaluated in every phase and are written in the Voigt

⁴Leopold Kronecker, 7.12.1823 – 29.12.1891, German mathematician who worked on number theory, algebra and logic.

4. Phase-Field Models with Elasticity

and in the tensorial notations, the second term in the previous equation can be rewritten as a linear combination of the scalar products for three-dimensional vectors. Thus, in the tensorial notation, the variational derivative with respect to the phase-field variable ϕ_α becomes

$$\begin{aligned} \frac{\partial f_{el}}{\partial \phi_\alpha} = \frac{1}{2} \left[\boldsymbol{\Sigma}^\alpha : \mathbf{E}_{el}^\alpha - \left(\frac{G^\alpha}{(\bar{G}^{\alpha\beta})^2} \langle \Delta \boldsymbol{\Sigma}^{\alpha\beta} \mathbf{n}, \Delta \boldsymbol{\Sigma}^{\alpha\beta} \mathbf{n} \rangle + \left(\frac{M^\alpha}{(\bar{M}^{\alpha\beta})^2} - \frac{G^\alpha}{(\bar{G}^{\alpha\beta})^2} \right) \langle \Delta \boldsymbol{\Sigma}^{\alpha\beta} \mathbf{n}, \mathbf{n} \rangle^2 \right) h_\beta^2 \right] h'_\alpha. \end{aligned}$$

The derivative of the interpolated elastic energy, with respect to the i -th component of the normal vectors in eq. (4.58), can also be written as a linear combination of the vector scalar products

$$\begin{aligned} \frac{\partial f_{el}}{\partial n_i} = -h_\alpha h_\beta \left(\frac{1}{\bar{G}^{\alpha\beta}} \langle \Delta \boldsymbol{\Sigma}^{\alpha\beta} \mathbf{e}_i, \Delta \boldsymbol{\Sigma}^{\alpha\beta} \mathbf{n} \rangle + \left(\frac{1}{\bar{M}^{\alpha\beta}} - \frac{1}{\bar{G}^{\alpha\beta}} \right) \langle \Delta \boldsymbol{\Sigma}^{\alpha\beta} \mathbf{e}_i, \mathbf{n} \rangle \langle \Delta \boldsymbol{\Sigma}^{\alpha\beta} \mathbf{n}, \mathbf{n} \rangle - \left(\frac{1}{\bar{M}^{\alpha\beta}} - \frac{1}{\bar{G}^{\alpha\beta}} \right)^2 \langle \Delta \boldsymbol{\Sigma}^{\alpha\beta} \mathbf{n}, \mathbf{n} \rangle^2 \langle \mathbf{F}_i^{\alpha\beta} \mathbf{n}, \mathbf{n} \rangle - \left(\frac{1}{\bar{G}^{\alpha\beta}} \right)^2 \langle \mathbf{F}_i^{\alpha\beta} \Delta \boldsymbol{\Sigma}^{\alpha\beta} \mathbf{n}, \Delta \boldsymbol{\Sigma}^{\alpha\beta} \mathbf{n} \rangle - \frac{1}{\bar{G}^{\alpha\beta}} \left(\frac{1}{\bar{M}^{\alpha\beta}} - \frac{1}{\bar{G}^{\alpha\beta}} \right) \langle \Delta \boldsymbol{\Sigma}^{\alpha\beta} \mathbf{n}, \mathbf{n} \rangle \langle \mathbf{F}_i^{\alpha\beta} \mathbf{n}, \mathbf{F}_i^{\alpha\beta} \Delta \boldsymbol{\Sigma}^{\alpha\beta} \mathbf{n} \rangle \right). \end{aligned}$$

The regular repetition of the vectors in the vector scalar products allows to optimise computational performance, see sec. C; however, it will not be able to fully escape the vector matrix multiplications, whereby the auxiliary matrices are

$$\mathbf{F}_1^{\alpha\beta} = \begin{pmatrix} \bar{M}^{\alpha\beta} n_1 & \bar{\lambda}^{\alpha\beta} n_2 & \bar{\lambda}^{\alpha\beta} n_3 \\ \bar{G}^{\alpha\beta} n_2 & \bar{G}^{\alpha\beta} n_1 & 0 \\ \bar{G}^{\alpha\beta} n_3 & 0 & \bar{G}^{\alpha\beta} n_1 \end{pmatrix}, \quad \mathbf{F}_2^{\alpha\beta} = \begin{pmatrix} \bar{G}^{\alpha\beta} n_2 & \bar{G}^{\alpha\beta} n_1 & 0 \\ \bar{G}^{\alpha\beta} n_1 & \bar{M}^{\alpha\beta} n_2 & \bar{\lambda}^{\alpha\beta} n_3 \\ 0 & \bar{G}^{\alpha\beta} n_3 & \bar{G}^{\alpha\beta} n_2 \end{pmatrix}$$

$$\text{and} \quad \mathbf{F}_3^{\alpha\beta} = \begin{pmatrix} \bar{G}^{\alpha\beta} n_3 & 0 & \bar{G}^{\alpha\beta} n_1 \\ 0 & \bar{G}^{\alpha\beta} n_3 & \bar{G}^{\alpha\beta} n_2 \\ \bar{\lambda}^{\alpha\beta} n_1 & \bar{\lambda}^{\alpha\beta} n_2 & \bar{M}^{\alpha\beta} n_3 \end{pmatrix}.$$

4.6. Extension of the model to multiphases

One of the drawbacks in the model by Schneider et al., in sec. 4.3, is the obscure procedure for the extension of the original two-phase model to the multiphase

4.6. Extension of the model to multiphases

case. Contrary to this mentioned difficulty, the enhancement of the presented alternative phase-field model in sec. 4.4 can be performed in a straightforward manner.

Since the two-phase-field model with elasticity is derived based on the mechanical jump conditions in sec. 4.2, according to the authors knowledge, there is no general explicit mechanical jump condition for the multipoint junctions. Therefore, the derivation of the multiphase-field model could not be derived theoretically, but is constructed ad hoc in such a way that the mechanical laws, which are valid for the two-phase systems, are preserved. Additionally to the assumption of the *two-phase system preservation*, further trivial assumptions should also be satisfied by the expansion procedure of the phase field elasticity model. Thus, if the two neighbouring phases are elastically the same, but also differ in the concentration, for example, but not in the eigenstrain and in the stiffness constants, then the presenting interface should not influence the homogeneous pseudo bulk elastic fields, and I name this requirement as *twin phases*. Furthermore, in the multipoint junctions, the formulation of all elastic fields should be *invariant under the index permutation* of the present phases. Moreover, the formulation should be *symmetric* in the sense that there is no preferred or reference phase.

By taking a closer look at the formula of the interpolated strain energy for two phases in eq. (4.54), the elastic energy potential is written in the system variables and depends on the total strain \mathbf{E} , on the phase-field ϕ and on the phase-field gradient $\nabla\phi$. In spite of the fact that the stresses are written as $\boldsymbol{\sigma}^\alpha$ and $\boldsymbol{\sigma}^\beta$, and the strain jump as $\Delta\bar{\boldsymbol{\varepsilon}}_{nn}^{\alpha\beta}$, their explicit definition in sec. 4.4.6 reveals the absence of any implicit phase-corresponding quantities.

In order to avoid confusion from the two-phase case, the used quantities in the extended formulation are redefined. In the following, the Voigt notation of strain and stress is used to write the phase-field elasticity model for multiphases. The total strain $\boldsymbol{\varepsilon}$ is a system variable and is locally calculated by the symmetrised displacement gradient, eq. (4.3). In the diffuse interface, all active phases, see sec. (2.2.1), are indexed from 1 to N_A , and the following stresses are defined as

$$\boldsymbol{\sigma}^\alpha = \mathbf{C}^\alpha(\boldsymbol{\varepsilon} - \bar{\boldsymbol{\varepsilon}}^\alpha), \quad \alpha \in \{1, \dots, N_A\},$$

so that the stress differences write as

$$\Delta\boldsymbol{\sigma}^{\alpha\beta} = \boldsymbol{\sigma}^\alpha - \boldsymbol{\sigma}^\beta, \quad \alpha, \beta \in \{1, \dots, N_A\}.$$

Furthermore, in the multipoint junctions, the normal of the two-phase interface is given by

$$\mathbf{n}^{\alpha\beta} = \frac{\nabla(\phi_\alpha - \phi_\beta)}{|\nabla(\phi_\alpha - \phi_\beta)|} \quad \alpha, \beta \in \{1, \dots, N_A\}.$$

4. Phase-Field Models with Elasticity

Independently of the shape of the diffuse multipoint junctions, the predefined normal vector is always perpendicular to the locus $\phi_\alpha - \phi_\beta = \text{const}$. By the previous definition of the normal vectors, there are also the corresponding sparse matrices $\mathbf{B}^{\alpha\beta}$ from eq. (4.51), which are given by

$$\mathbf{B}^{\alpha\beta} = \begin{pmatrix} n_1^{\alpha\beta} & 0 & 0 & 0 & n_3^{\alpha\beta} & n_2^{\alpha\beta} \\ 0 & n_2^{\alpha\beta} & 0 & n_3^{\alpha\beta} & 0 & n_1^{\alpha\beta} \\ 0 & 0 & n_3^{\alpha\beta} & n_2^{\alpha\beta} & n_1^{\alpha\beta} & 0 \end{pmatrix} \quad \alpha, \beta \in \{1, \dots, N_A\}.$$

And after the definition of the asymmetrically interpolated stiffness tensors

$$\bar{\mathbf{C}}^{\alpha\beta} = \mathbf{C}^\alpha h_\beta + \mathbf{C}^\beta h_\alpha, \quad \text{for } \alpha, \beta \in \{1, \dots, N_A\},$$

the required pseudo inverses write as

$$\bar{\mathbf{S}}_{nn}^{\alpha\beta} = (\mathbf{B}^{\alpha\beta})^T \left(\mathbf{B}^{\alpha\beta} \bar{\mathbf{C}}^{\alpha\beta} (\mathbf{B}^{\alpha\beta})^T \right)^{-1} \mathbf{B}^{\alpha\beta}, \quad \alpha, \beta \in \{1, \dots, N_A\}.$$

Finally, with the predefinitions of the auxiliary quantities, the interpolated strain energy for the multiphase can be formulated as

$$f_{el}(\phi, \nabla\phi, \varepsilon) = \frac{1}{2} \sum_{\alpha=1}^N \left[\langle \varepsilon - \tilde{\varepsilon}^\alpha, \boldsymbol{\sigma}^\alpha \rangle - \frac{1}{2} \sum_{\beta \neq \alpha} \langle \Delta\boldsymbol{\sigma}^{\alpha\beta}, \bar{\mathbf{S}}_{nn}^{\alpha\beta} \Delta\boldsymbol{\sigma}^{\alpha\beta} \rangle h_\beta \right] h_\alpha. \quad (4.64)$$

Since the normals

$$\mathbf{n}^{\alpha\beta} = -\mathbf{n}^{\beta\alpha}$$

are oriented in the opposite directions, and also the matrices are $\mathbf{B}^{\alpha\beta} = -\mathbf{B}^{\beta\alpha}$, the corresponding pseudo inverses equate

$$\bar{\mathbf{S}}_{nn}^{\alpha\beta} = \bar{\mathbf{S}}_{nn}^{\beta\alpha}.$$

Hence, the terms

$$\langle \Delta\boldsymbol{\sigma}^{\alpha\beta}, \bar{\mathbf{S}}_{nn}^{\alpha\beta} \Delta\boldsymbol{\sigma}^{\alpha\beta} \rangle = \langle \Delta\boldsymbol{\sigma}^{\beta\alpha}, \bar{\mathbf{S}}_{nn}^{\beta\alpha} \Delta\boldsymbol{\sigma}^{\beta\alpha} \rangle$$

are the same because of the bilinearity of the vector scalar product. Therefore, the interpolated interfacial strain energy can be rewritten in an alternative manner as

$$f_{el}(\phi, \nabla\phi, \varepsilon) = \frac{1}{2} \sum_{\alpha=1}^N \left[\langle \varepsilon - \tilde{\varepsilon}^\alpha, \boldsymbol{\sigma}^\alpha \rangle h_\alpha - \sum_{\beta < \alpha} \langle \Delta\boldsymbol{\sigma}^{\alpha\beta}, \bar{\mathbf{S}}_{nn}^{\alpha\beta} \Delta\boldsymbol{\sigma}^{\alpha\beta} \rangle h_\beta h_\alpha \right].$$

4.6. Extension of the model to multiphases

And the reduction of the general formulations for a two-phase case is nothing but the formula in eq. (4.54).

The generality of the formulation in eq. (4.64) is obvious, and the phase indices α and β can permute in the arbitrary manner. Thus, the expression remains unchanged because the expression is written in a symmetric manner.

Using the expression for the strain energy for multiphases, the appropriate interfacial Voigt stress is given by the corresponding derivative, with respect to the Voigt strain ε , and explicitly writes as

$$\boldsymbol{\sigma} = \frac{\partial f_{el}}{\partial \boldsymbol{\varepsilon}} = \sum_{\alpha=1}^N \left(\boldsymbol{\sigma}^{\alpha} - \frac{1}{2} \sum_{\beta \neq \alpha}^N (\mathbf{C}^{\alpha} - \mathbf{C}^{\beta}) \bar{\mathbf{S}}_{nn}^{\alpha\beta} \Delta \boldsymbol{\sigma}^{\alpha\beta} h_{\beta} \right) h_{\alpha}.$$

Note that in the case of twin phases, α and β , both stiffness tensors equate and the difference $\mathbf{C}^{\alpha} - \mathbf{C}^{\beta}$ eliminates the contribution of the $\alpha\beta$ interface.

The alternative formula for the stress calculation

$$\boldsymbol{\sigma} = \frac{\partial f_{el}}{\partial \boldsymbol{\varepsilon}} = \sum_{\alpha=1}^N \left(\boldsymbol{\sigma}^{\alpha} - \sum_{\beta < \alpha}^N (\mathbf{C}^{\alpha} - \mathbf{C}^{\beta}) \bar{\mathbf{S}}_{nn}^{\alpha\beta} \Delta \boldsymbol{\sigma}^{\alpha\beta} h_{\beta} \right) h_{\alpha} \quad (4.65)$$

is beneficial because of the halving of the required calculations.

By the derivation of the driving force, the respective variational derivatives write as

$$\frac{\partial f_{el}}{\partial \phi_{\alpha}} = \frac{1}{2} \left(\langle \boldsymbol{\varepsilon} - \tilde{\boldsymbol{\varepsilon}}^{\alpha}, \boldsymbol{\sigma}^{\alpha} \rangle - \sum_{\beta \neq \alpha} \langle \bar{\mathbf{S}}_{nn}^{\alpha\beta} \Delta \boldsymbol{\sigma}^{\alpha\beta}, \mathbf{C}^{\alpha} \bar{\mathbf{S}}_{nn}^{\alpha\beta} \Delta \boldsymbol{\sigma}^{\alpha\beta} \rangle h_{\beta}^2 \right) h'_{\alpha}, \quad (4.66)$$

and again in the case of the twin phases, the vanishing stress difference $\Delta \boldsymbol{\sigma}^{\alpha\beta} = \mathbf{0}$ removes the undesired terms from the driving force of the α phase. The same appears in the second term, which is given by

$$\frac{\partial f_{el}}{\partial \nabla \phi_{\alpha}} = \sum_{\beta \neq \alpha} \frac{1}{|\nabla \phi_{\alpha} - \nabla \phi_{\beta}|} \frac{\partial f_{el}}{\partial \mathbf{n}^{\alpha\beta}}$$

with

$$\frac{\partial f_{el}}{\partial n_i^{\alpha\beta}} = -h_{\alpha} h_{\beta} \left\langle \Delta \boldsymbol{\sigma}^{\alpha\beta} - \bar{\mathbf{C}}^{\alpha\beta} \bar{\mathbf{S}}_{nn}^{\alpha\beta} \Delta \boldsymbol{\sigma}^{\alpha\beta}, \mathbf{D}_i^T (\bar{\mathbf{C}}_{nn}^{\alpha\beta})^{-1} \mathbf{B}^{\alpha\beta} \Delta \boldsymbol{\sigma}^{\alpha\beta} \right\rangle.$$

Therefore, the assumed absence of all interfacial effects in the interface between two elastic twin phases is fulfilled.

In summary, by the formulation of the interpolated strain energy for multiphases, all assumed properties to the construction are achieved. Thus, the formulation

4. *Phase-Field Models with Elasticity*

is given in a general form and in a symmetric manner, so that the expression is invariant under the renaming of phases. Furthermore, by the reduction to the two-phase case, the general formula of the strain energy and the consequential stress and driving force formulations all result in the known expressions in sec. 4.4, and hence are in accordance with the thermodynamically and mechanically consistent derivation. Finally, the additional requirement of the elimination of all interfacial elastic effects in the interface between two elastic twin phases is also realised.

Note that the simplifications in the appropriate calculations of the required elastic fields in the case of elastic isotropic phases, sec. 4.5.1, can also be applied in the general multiphase case, whereby the elastic isotropy should be fulfilled in the stiffness matrix, but is not assumed in the eigenstrain. Hence anisotropic shapes could be reached.

5. Validation of the presented phase-field elasticity models

Since the previous analysis is quantitatively derived for the transformation of two phases, which is driven by the elastic driving force, the verification of the model is also based on the simulation setup with two transitional phases. As mentioned in sec. 2.1.1, only one phase-field parameter ϕ suffices to rewrite the model.

5.1. Introduction

In our recent work [30], we also analysed a simulation setup consisting of two phases and investigated numerical solutions in one dimension and one scenario in two dimensions. While the analytical solutions are given for the equilibrium states, we performed simulations, in which the two-phase system are mimicked numerically to converge into the system equilibrium.

The shown matches in [30], between the analytical and the numerical results, for the one-dimensional case are excellent. For the performed 2-D simulation of a circular inclusion in a surrounded matrix, which was influenced by elastic transformational and capillary forces, we also get a brilliant agreement between the theoretical prediction of the surface tension and the computational parameter.

In the thermodynamical and in the mechanical equilibria, both the capillary and the configurational forces equate. This fact is also known as a Gibbs-Thomson equation [82] and explicitly writes as

$$\sigma_{\alpha\beta}\kappa = f_{el}^{\alpha}(\mathbf{E}^{\alpha}) - f_{el}^{\alpha}(\mathbf{E}^{\beta}) - \langle \boldsymbol{\Sigma}\mathbf{n}_{\alpha\beta}, (\mathbf{E}^{\alpha} - \mathbf{E}^{\beta})\mathbf{n}_{\alpha\beta} \rangle,$$

with the surface tension parameter $\sigma_{\alpha\beta}$ and the local interfacial curvature κ . Hence, by matching the equilibrium properties for the sharp interface, and by applying them in the diffuse interface simulations, we can assign the accordance between the modelling and the analysis.

The mentioned disadvantage of the used procedure in [30] is the metastability of the final state. Thus, the equality of capillary and elastic forces is not stable

5. Validation of the presented phase-field elasticity models

and any small perturbation of the ideally equilibrated system would result in a growth or shrinkage of the circular inclusion. Therefore, we performed a series of simulations in [30], with the same initial circular shape and the same elastic field contributions, but with a different surface energy parameter around the analytical value. The assignment of the numerical parameter to the analytical value was done by the evolution change from a shrinking ($\partial_t\phi < 0$) to a growing ($\partial_t\phi > 0$) behaviour, and consequently from balancing the capillary and elastic driving forces.

To stabilise the quasi-equilibrium state between the elastic transformational and capillary forces in the thermodynamic equilibrium, the considered phase-field model in this work is extended by the chemical part, which is presented in the next paragraph. Therefore, an additional driving force in the force balance equation as well as the conservation of the total composition concentration in the isolated system both strengthen the desired equilibrium state. Furthermore, the coupling of the phase-field model with the quantitative elastic and chemical models is also relevant to simulate different manufacturing processes. This also applies to the postwelded phase transformations. This is because, the composition of the fastly solidified grains is also not equilibrated thermodynamically, so that the segregation of the components occurs and the formation of new phases takes place, which also produces residual stresses in the weld sample.

Moreover, in order to validate the presented models in more detail, as well as the model by Schneider et al. in sec. 4.3 and the newly suggested formulation in sec. (4.4), two-dimensional simulations will be performed. A two-phase setup is of interest, for which all required quantities and, in particular, the elastic fields are known. Pursuing this objective, the Eshelby inclusion is found as an ideal setup. For an *elliptical* inclusion or inhomogeneity in the embedded infinite matrix, which is without any residual strains, the elastic fields are given in a closed-form solution [86]. A short analytical base of the tested scenarios and the adoption of the corresponding simulation parameters are presented in the following paragraphs.

Finally, the simulation results for nine different scenarios are presented for both models and are compared to the analytical solutions.

5.2. Extension of the model by the chemical part

Wide spectrums of different alloys over a processing temperature regime are studied and often result in thermodynamic databases such as CALPHAD. The equilibrium phase diagrams for multicomponent alloys are constructed with approximated free energies, wherein the Redlich-Kister approach is used. For the

5.2. Extension of the model by the chemical part

performance of simulations for the real manufacturing processes with real materials, simplifying assumptions are often used. In [87], Eiken et al. suggested to evaluate the evolution equations with extrapolated quasi-equilibrium thermodynamic data. Using the parabolic extrapolation scheme, the large-scale simulations of the directional solidification can be performed quantitatively [88].

In the further analysis, the consideration is limited to two components and, for simplicity, the same molar volume for both transitioning phases is assumed. Furthermore, assuming the Helmholtz free energies of the different phases (α and β) to depend on the independent concentration $c_A = c$ ($c_B = 1 - c$), and to be the parabolas with the appropriate coefficients

$$f_{ch}^{\alpha,\beta}(c) = A_0^{\alpha,\beta} + A_1^{\alpha,\beta}c + A_2^{\alpha,\beta}c^2,$$

the corresponding grand potentials, also known as Landau potentials,

$$\omega^{\alpha,\beta}(\mu) = -\frac{(\mu - A_1^{\alpha,\beta})^2}{4A_2^{\alpha,\beta}} + A_0^{\alpha,\beta}$$

are derived straightforwardly using the Legendre¹ transformation, see Figure 2.4.

In the phase-field context [43], the free energy in the diffuse interface is interpolated with the phase-dependent concentrations

$$f_{ch}(c, \phi) = f_{ch}^\alpha(c^\alpha)h(\phi) + f_{ch}^\beta(c^\beta)(1 - h(\phi)), \quad (5.1)$$

see also eq. (2.13). In this context, compare the interpolation of the elastic energy with phase-dependent strains in sec. 4.4.3.

Therefore, and under the assumption of the homogeneous chemical potential in the diffuse interface

$$\mu = \left. \frac{\partial f_{ch}^\alpha(c)}{\partial c} \right|_{c^\alpha} = \left. \frac{\partial f_{ch}^\beta(c)}{\partial c} \right|_{c^\beta},$$

the chemical driving force for the phase transformation writes as

$$\delta_\phi f_{ch} = \left(f_{ch}^\alpha(c^\alpha) - f_{ch}^\beta(c^\beta) - \mu(c^\alpha - c^\beta) \right) h'(\phi) \quad (5.2)$$

or, equivalently, directly as the difference of the Landau potentials

$$\delta_\phi f_{ch} = (\omega^\alpha(\mu) - \omega^\beta(\mu))h'(\phi), \quad (5.3)$$

¹Adrien-Marie Legendre, 18.09.1752 – 10.01.1833, French mathematician. His name is one of the 72 names inscribed on the Eiffel Tower. The Moon crater Legendre is named after him.

5. Validation of the presented phase-field elasticity models

as a consequent result of the grand chemical potential interpolation

$$\omega(\mu, \phi) = \omega^\alpha(\mu)h(\phi) + \omega^\beta(\mu)(1 - h(\phi)), \quad (5.4)$$

like in [41, 42]. Thus, the objective functional of Ginzburg-Landau type can be written as a Helmholtz free energy

$$\mathcal{F} = \int_V f_{cap}(\phi, \nabla\phi) + f_{ch}(c, \phi) + f_{el}(\phi, \nabla\phi, \boldsymbol{\varepsilon})dV$$

or, in terms of the Landau potential,

$$\Omega = \int_V f_{cap}(\phi, \nabla\phi) + \omega_{ch}(\mu, \phi) + f_{el}(\phi, \nabla\phi, \boldsymbol{\varepsilon})dV,$$

whereby the interfacial energy contribution is noted as a capillary part

$$f_{cap}(\phi, \nabla\phi) = \gamma(\epsilon|\nabla\phi|^2 + \frac{1}{\epsilon}\frac{16}{\pi^2}\phi(1 - \phi)).$$

5.2.1. Evolution equations

The corresponding evolution equations of the model extended with the chemical part follow the variational principle and write for the phase-field variable as

$$\tau\epsilon\partial_t\phi = -\left(\delta_\phi f_{cap}(\phi, \nabla\phi) + \delta_\phi f_{ch}(c(\mu)) + \delta_\phi f_{el}(\phi, \nabla\phi, \boldsymbol{\varepsilon})\right). \quad (5.5)$$

As the focus in the further computational study lies on the validation of the elastic model, for simplicity I use a chemical model with the same diffusivity $D = D^\alpha = D^\beta$ in both phases. Therefore, the anti-trapping current [42, 15] is neglected and the matter diffusion is given as a tempo-spatial differential equation of chemical potential μ , which writes explicitly as

$$\partial_t\mu = \frac{1}{\chi(\phi)}\left(D\nabla \cdot (\chi(\phi)\nabla\mu) - (c^\alpha(\mu) - c^\beta(\mu))\partial_t h\right), \quad (5.6)$$

with the susceptibility

$$\chi(\phi) = \frac{1}{2}\left(\frac{h(\phi)}{A_2^\alpha} + \frac{1 - h(\phi)}{A_2^\beta}\right),$$

and with the concentrations

$$c^i(\mu) = -\frac{\partial\omega^i(\mu)}{\partial\mu} = \frac{(\mu - A_1^i)}{2A_2^i}, \quad i = \alpha, \beta.$$

5.2. Extension of the model by the chemical part

The evolution equation for the displacement field is given by the momentum balance equation

$$\rho \ddot{\mathbf{u}} = - \frac{\delta f_{el}}{\delta \mathbf{u}} = \nabla \cdot \frac{\partial f_{el}}{\partial \boldsymbol{\varepsilon}} = \nabla \cdot \boldsymbol{\Sigma}. \quad (5.7)$$

While the evolution equations of the system variables are presented, the analysed setup is presented in the next paragraph.

5.2.2. Thermodynamical and mechanical equilibrium

Therefore, and after the incorporation of the chemical part into the model, the corresponding thermodynamical and mechanical equilibria are given by the conditions written in the sharp interface formulation [82]

$$\mu = const \quad (5.8)$$

$$\mathbf{0} = \nabla \cdot \boldsymbol{\Sigma} \quad (5.9)$$

$$0 = \sigma_{\alpha\beta} \kappa^{\alpha\beta} + f_{ch}^{\alpha}(c^{\alpha}(\mu)) - f_{ch}^{\beta}(c^{\beta}) - \mu(c^{\alpha}(\mu) - c^{\beta}(\mu)) + f_{el}^{\alpha}(\boldsymbol{\varepsilon}^{\alpha}) - f_{el}^{\beta}(\boldsymbol{\varepsilon}^{\beta}) - \langle \boldsymbol{\Sigma}^{\alpha} \mathbf{n}, (\mathbf{E}^{\alpha} - \mathbf{E}^{\beta}) \mathbf{n} \rangle. \quad (5.10)$$

Eq. (5.8) means that the chemical potential is constant in the total simulation domain in the end state, and that, furthermore, there is no mass flux

$$\nabla \mu = 0 \rightarrow \partial_t c = 0,$$

so that the composition is stationary. The mechanical equilibrium, eq. (5.9), implies a steady distribution of the stress field, with a vanishing traction vector $\boldsymbol{\Sigma}^{\alpha} \mathbf{n}_{\alpha\beta} = \boldsymbol{\Sigma}^{\beta} \mathbf{n}_{\alpha\beta}$ on the common interface. Equation (5.10) is also known as Gibbs-Thomson equation, which balances the forces acting on the interface, namely (1.) the capillary force, (2.) the constant chemical force, as a difference of both grand chemical potentials,

$$\Delta \omega^{\alpha\beta}(\mu) = \omega^{\alpha}(\mu) - \omega^{\beta}(\mu) = f_{ch}^{\alpha}(c^{\alpha}) - \mu c^{\alpha} - (f_{ch}^{\beta}(c^{\beta}) - \mu c^{\beta})$$

and (3.) the elastic driving force, which up to now is noted as

$$\Delta p_{el}^{\alpha\beta} = f_{el}(\mathbf{E}^{\alpha}) - \langle \boldsymbol{\Sigma} \mathbf{n}, \mathbf{E}^{\alpha} \mathbf{n} \rangle - (f_{el}(\mathbf{E}^{\beta}) - \langle \boldsymbol{\Sigma} \mathbf{n}, \mathbf{E}^{\beta} \mathbf{n} \rangle).$$

The Gibbs-Thomson equation rewrites to the shorthand notation as

$$0 = \sigma_{\alpha\beta} \kappa^{\alpha\beta} + \Delta p_{el}^{\alpha\beta} + \Delta \omega^{\alpha\beta}. \quad (5.11)$$

Thus, if the force balance is achieved, the interface is stationary.

5. Validation of the presented phase-field elasticity models

However, allow me to say a few more words about this fundamental balance equation. Because of the homogeneous chemical potential, eq. (5.8), the corresponding chemical driving is constant along the interface. Therefore, two other summands, the capillary and the elastic terms, should also summarise to a constant. Furthermore, since the surface energy and the elastic potential jump act contradictory, the jump in the grand potentials negates the shrinkage. In this sense, the inclusion should be chemically undercooled.

Furthermore, by the comparison of eqs. (5.5) and (5.11), the similarity of both equations is obvious, and thus the diffuse interface formulation should resolve the sharp interface condition [89].

5.3. Eshelby inclusion

As mentioned in the introduction to this chapter, an elliptical inclusion or inhomogeneity in the infinitely embedded matrix is found as an ideal simulation setup for the detailed validation of the presented models. But, at the beginning, I want to pay attention to the difference between both the **inclusion** and the **inhomogeneity**, notions which are used in the sense of Eshelby [90], whereby the former has a non-vanishing eigenstrain but the same stiffness as the environmental matrix ($\mathbf{C}^{Inc} = \mathbf{C}^M$), and the latter is also characterised by the different stiffness tensor ($\mathbf{C}^{Inh} \neq \mathbf{C}^M$) and the eigenstrain [86]. As already used, in order to differentiate the different phases, the superscripts *Inc*, *M* and *Inh* are used for the inclusion, for the matrix and for the inhomogeneity, respectively. Sometimes the superscript *I* is used if there is no relevant difference between the type of the precipitate. Thus, for example, σ_{IM} is the surface energy parameter for the interface between the inlay and the matrix.

For simplicity, a plane strain case in 2-D is considered in the analysis and in the following simulations. Thus, the reduced Voigt stress and strain vectors write as

$$\boldsymbol{\sigma} = (\Sigma_{xx}, \Sigma_{yy}, \Sigma_{zz}, \Sigma_{xy},) = (\sigma_{xx}, \sigma_{yy}, \sigma_{zz}, \sigma_{xy})$$

and

$$\boldsymbol{\varepsilon} = (\mathbf{E}_{xx}, \mathbf{E}_{yy}, 0, 2\mathbf{E}_{xy}) = (\varepsilon_{xx}, \varepsilon_{yy}, 0, \varepsilon_{xy}),$$

respectively.

For an elliptical inclusion, see Figure 5.1, which is embedded in the infinite plane strain matrix with the same stiffness constants and whose ratio of semi-axes is [86]

$$t = \frac{b}{a},$$

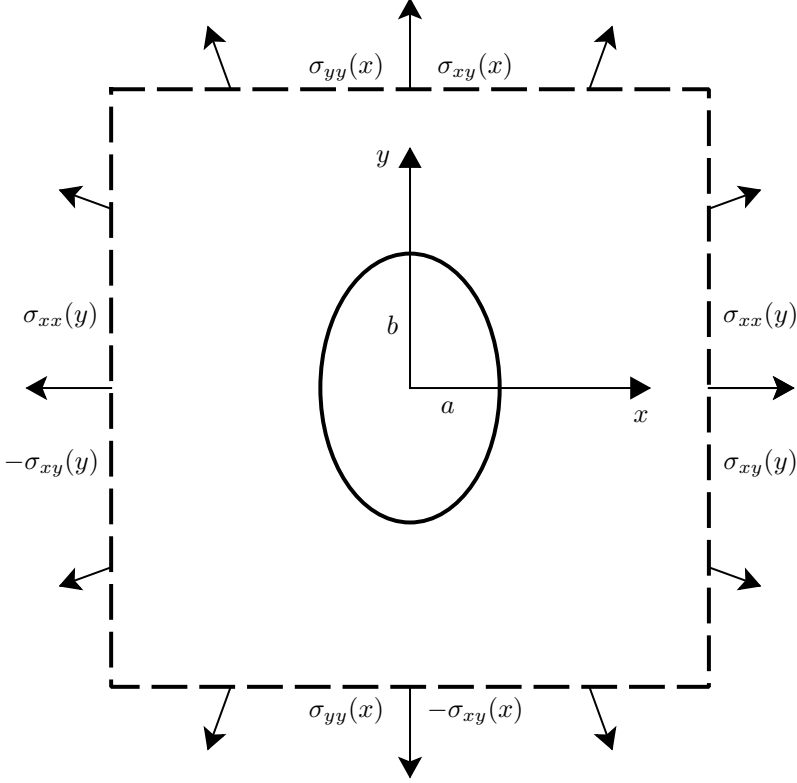


Figure 5.1.: Elliptical inclusion in the matrix and the simulation setup

there is the Eshelby tensor \mathbf{S} , which depends on the geometry of the inclusion, t as well as on the same Poisson ratio $\nu = \nu^M = \nu^{Inc}$, see appendix B.

The **eigenstrain in the inclusion** writes as $\hat{\boldsymbol{\varepsilon}} = (\hat{\varepsilon}_{xx}, \hat{\varepsilon}_{yy}, 0, \hat{\varepsilon}_{xy})^T$ for the plane strain case, and the total inner strain in the inclusion is constant [90] and is given by [86]

$$\boldsymbol{\varepsilon}^{Inc} = \mathbf{S}(t, \nu)\hat{\boldsymbol{\varepsilon}}. \quad (5.12)$$

The corresponding constant inner stress field is given by Hooke's law as

$$\boldsymbol{\sigma}^{Inc} = \mathbf{C}(\boldsymbol{\varepsilon}^{Inc} - \hat{\boldsymbol{\varepsilon}}) = \mathbf{C}(\mathbf{S}(t, \nu) - \mathbf{1}_{(4 \times 4)})\hat{\boldsymbol{\varepsilon}}. \quad (5.13)$$

To derive the stress and strain distribution in the matrix, Jin et al. presented an auxiliary spatially dependent matrix $\mathbf{H}(x, y)$ in [86], so that the elastic fields

5. Validation of the presented phase-field elasticity models

outside the inclusion are given as

$$\boldsymbol{\sigma}^M(x, y) = \mathbf{H}(x, y)\hat{\boldsymbol{\varepsilon}}, \quad (5.14)$$

$$\boldsymbol{\varepsilon}^M(x, y) = \mathbf{C}^{-1}\boldsymbol{\sigma}^M(x, y). \quad (5.15)$$

For completeness, all used tensors in the calculations are listed in the appendix B. With the given strain and stress distribution, the corresponding driving force for the inclusion writes in the sharp interface as

$$\Delta p_{el}^{Inc}(\hat{\boldsymbol{\varepsilon}}) = \frac{1}{2}\langle \boldsymbol{\sigma}^{Inc}, \boldsymbol{\varepsilon}^{Inc} - \hat{\boldsymbol{\varepsilon}} \rangle - \frac{1}{2}\langle \boldsymbol{\sigma}^M, \boldsymbol{\varepsilon}^M \rangle - \langle \mathbf{N}_\sigma \boldsymbol{\sigma}^{Inc}, \boldsymbol{\varepsilon}^{Inc} - \boldsymbol{\varepsilon}^M \rangle, \quad (5.16)$$

with the tensor \mathbf{N}_σ for the normal constituent of the Voigt stress, written for a two-dimensional plane strain case as

$$\mathbf{N}_\sigma = \begin{pmatrix} n_x^2(2 - n_x^2) & -n_x^2 n_y^2 & 0 & 2n_x n_y^3 \\ -n_x^2 n_y^2 & n_y^2(2 - n_y^2) & 0 & 2n_x^3 n_y \\ 0 & 0 & 0 & 0 \\ n_x n_y^3 & n_x^3 n_y & 0 & 1 - 2n_x^2 n_y^2 \end{pmatrix}.$$

5.3.1. Elastic constants versus geometrical form

The elastic driving force $\Delta p_{el}(\hat{\boldsymbol{\varepsilon}})$ in the sharp interface, in eq. (5.16) solely depends on the eigenstrain and on the location at the elliptical phase boundary by the local change in $\mathbf{N}_\sigma(x, y)$ and in $\mathbf{H}(x, y)$. In particular, at both vertices, it is

$$\Delta p_{el}^{Inc}(a, 0) = \frac{G}{1 - \nu} \frac{(2 + t)\hat{\boldsymbol{\varepsilon}}_{xx}^2 + 2t\hat{\boldsymbol{\varepsilon}}_{xx}\hat{\boldsymbol{\varepsilon}}_{yy} + (t^2 - t - 1)\hat{\boldsymbol{\varepsilon}}_{yy}^2}{(1 + t)^2}, \quad \text{and} \quad (5.17)$$

$$\Delta p_{el}^{Inc}(0, b) = \frac{G}{1 - \nu} \frac{(1 - t - t^2)\hat{\boldsymbol{\varepsilon}}_{xx}^2 + 2t\hat{\boldsymbol{\varepsilon}}_{xx}\hat{\boldsymbol{\varepsilon}}_{yy} + t(1 + 2t)\hat{\boldsymbol{\varepsilon}}_{yy}^2}{(1 + t)^2},$$

respectively. Moreover, the curvatures at the vertices are also known, $\kappa(a, 0) = \frac{a}{b^2}$ and $\kappa(0, b) = \frac{b}{a^2}$. Then, writing the Gibbs-Thomson equation (5.11) for both critical points of the ellipse, and taking the difference of both, after some elementary mathematical reformulations, it results in

$$\frac{G}{1 - \nu} (\hat{\boldsymbol{\varepsilon}}_{xx}^2 - \hat{\boldsymbol{\varepsilon}}_{yy}^2) = \sigma_{IM} \left(\frac{b}{a^2} - \frac{a}{b^2} \right), \quad (5.18)$$

whereby the chemical driving force contribution vanishes by the constant value at any interface point. Consequently, for the desired ellipse with the semi-axes a and b , and with the surface energy σ_{IM} , the components of the residual strain in the inclusion could not be arbitrary, but should satisfy the foregoing equality. Hence, the previous equation prescribes the match between the elastic constants on the left and the capillary values on the right.

5.3.2. Elliptical inhomogeneity and the equivalent inclusion method

In the case, in which the stiffness tensor of the embedded elliptical precipitate differs from its counterpart in the matrix $\mathbf{C}^{Inh} \neq \mathbf{C}^M$, one speaks of inhomogeneity. Herein, the notation $\tilde{\boldsymbol{\varepsilon}}^{Inh}$ is used for the **eigenstrain in the inhomogeneity**. To calculate the corresponding elastic fields in this setup, a spatial equivalent system, but with an inclusion, is considered. The challenge herein is the determination of the eigenstrain $\hat{\boldsymbol{\varepsilon}}$ for this equivalent inclusion. But by using the equivalent internal stress $\boldsymbol{\sigma}^{Inh} = \boldsymbol{\sigma}^{Inc}$ and the strains $\boldsymbol{\varepsilon}^{Inh} = \boldsymbol{\varepsilon}^{Inc}$ in both the inhomogeneity and the inclusion, the following equation should be satisfied

$$\left((\mathbf{C}^{Inh} - \mathbf{C}^M) \mathbf{S} + \mathbf{C}^M \right) \hat{\boldsymbol{\varepsilon}} = \mathbf{C}^{Inh} \tilde{\boldsymbol{\varepsilon}}^{Inh}.$$

In the next validation scenarios, the presented approach of the equivalent inclusion method is used in an inverse manner. Using the relation between the eigenstrains in the inclusion and in the inhomogeneity, the residual strain for the inhomogeneity calculates as

$$\tilde{\boldsymbol{\varepsilon}}^{Inh} = (\mathbf{C}^{Inh})^{-1} \left((\mathbf{C}^{Inh} - \mathbf{C}^M) \mathbf{S} + \mathbf{C}^M \right) \hat{\boldsymbol{\varepsilon}}. \quad (5.19)$$

Thus, to a fixed eigenstrain in the inclusion $\hat{\boldsymbol{\varepsilon}}$, the spatial distributions of stress and strain are given by the equations (5.12) - (5.15) and would not change by varying the stiffness constants in the precipitate \mathbf{C}^{Inh} , as long as the corresponding eigenstrain $\tilde{\boldsymbol{\varepsilon}}^{Inh}$ is given by the previous equation. This remarkable property is used in the following simulations.

In spite of the fact that the stress and strain contributions remain the same for all setups, the elastic driving force will change with varying stiffness constants in the inhomogeneity \mathbf{C}^{Inh} and with changing eigenstrain $\tilde{\boldsymbol{\varepsilon}}^{Inh}$. But by using the equivalence in the stress and strain fields for the equivalent inclusion, $\boldsymbol{\sigma}^{Inh} = \boldsymbol{\sigma}^{Inc}$ and $\boldsymbol{\varepsilon}^{Inc} = \boldsymbol{\varepsilon}^{Inh}$, the elastic driving force can be rewritten as

$$\begin{aligned} \Delta p^{Inh} &= \frac{1}{2} \langle \boldsymbol{\sigma}^{Inh}, \boldsymbol{\varepsilon}^{Inh} - \tilde{\boldsymbol{\varepsilon}}^{Inh} \rangle - \frac{1}{2} \langle \boldsymbol{\sigma}^M, \boldsymbol{\varepsilon}^M \rangle - \langle \mathbf{N}_\sigma \boldsymbol{\sigma}^{Inh}, \boldsymbol{\varepsilon}^{Inh} - \boldsymbol{\varepsilon}^M \rangle = \\ &= \frac{1}{2} \langle \boldsymbol{\sigma}^{Inc}, \boldsymbol{\varepsilon}^{Inc} - \tilde{\boldsymbol{\varepsilon}}^{Inh} \rangle - \frac{1}{2} \langle \boldsymbol{\sigma}^M, \boldsymbol{\varepsilon}^M \rangle - \langle \mathbf{N}_\sigma \boldsymbol{\sigma}^{Inc}, \boldsymbol{\varepsilon}^{Inc} - \boldsymbol{\varepsilon}^M \rangle = \\ &= \frac{1}{2} \langle \boldsymbol{\sigma}^{Inc}, \boldsymbol{\varepsilon}^{Inc} - \tilde{\boldsymbol{\varepsilon}}^{Inh} \rangle - \frac{1}{2} \langle \boldsymbol{\sigma}^M, \boldsymbol{\varepsilon}^M \rangle - \langle \mathbf{N}_\sigma \boldsymbol{\sigma}^{Inc}, \boldsymbol{\varepsilon}^{Inc} - \boldsymbol{\varepsilon}^M \rangle = \\ &= \Delta p_{el}^{Inc}(\hat{\boldsymbol{\varepsilon}}) + \frac{1}{2} \langle \boldsymbol{\sigma}^{Inc}, \hat{\boldsymbol{\varepsilon}} - \tilde{\boldsymbol{\varepsilon}}^{Inh} \rangle. \end{aligned}$$

By the substitution of the right-hand side of eq. (5.19), and the expression for the inner stress in eq. (5.13), the elastic driving force for the elliptical inhomogeneity

5. Validation of the presented phase-field elasticity models

is given by

$$\Delta p_{el}^{Inh}(\hat{\boldsymbol{\varepsilon}}, \mathbf{C}^{Inh}) = \Delta p_{el}^{Inc}(\hat{\boldsymbol{\varepsilon}}) + \frac{1}{2} \left\langle \boldsymbol{\sigma}^{Inc}(\hat{\boldsymbol{\varepsilon}}), \left(\mathbf{1} - (\mathbf{C}^{Inh})^{-1} \mathbf{C}^M \right) (\mathbf{1} - \mathbf{S}) \hat{\boldsymbol{\varepsilon}} \right\rangle. \quad (5.20)$$

Therefore, by changing the stiffness tensor for an inhomogeneity, and by the corresponding change in the eigenstrain, eq. (5.19), the resulting elastic driving force is nothing but the configurational force for the inclusion in eq. (5.16), added to a constant value. Thus, the elastic driving force, and consequently the ratio of the elastic contribution in the Gibbs-Thomson equation (5.11), can be scaled up and down. The foregoing procedure allows to perform a more detailed and accurate validation of the elastic driving force for different scenarios with a minimal computational effort.

5.4. Preparation of the simulations

As a first step, theoretical calculations of the elastic fields as well as for the chemical model are performed with the computer algebra system **Wolfram Mathematica**, for an ellipse with semi-axes $a = 60$ and $b = 90$, see Figure 5.1. In the following, all quantities are dimensionless, and the interfacial energy parameter is

$$\sigma_{IM} = 0.0942214.$$

5.4.1. Parameter and conditions for the elastic model

In the considered simulation setups, both the matrix phase and the inclusion/inhomogeneity phases are assumed to be elastically isotropic. The corresponding values of the Young modules and of the Poisson ratios in the matrix and in the inclusion are

$$E^M = E^{Inc} = 2100 \quad \text{and} \quad \nu^M = \nu^{Inc} = 0.25,$$

respectively. For the chosen semi-axes of the elliptical inclusion, the components of the corresponding residual strain are chosen with respect to eq. (5.18) and are

$$\hat{\boldsymbol{\varepsilon}} = (0.00205, 0.00165, 0, 0).$$

The analytical expressions for the inner and outer elastic fields in eqs. (5.12) - (5.15) are derived for an infinite plane strain plate [86] and are

$$\begin{aligned} \boldsymbol{\varepsilon}^I &= (0.001624, 0.000869333, 0, 0), \\ \boldsymbol{\sigma}^I &= (-1.72928, -2.32512, -1.0136, 0). \end{aligned}$$

5.4. Preparation of the simulations

Note that it is not possible to replicate an infinite domain in the simulation. In order to solve this question, the stress distribution is calculated along the boundary of the rectangular simulation domain with the dimensions $L_x = L_y = 441$. The spatial step in both directions is assumed to be the same namely, $\Delta x = \Delta y = 1$. Thus, to adopt the analytical and computational results, the analytical stress components at the boundary are impressed as stress boundary conditions. Note that not all stress components are used at the boundary, but only the orthogonal stress components, see Figure 5.1.

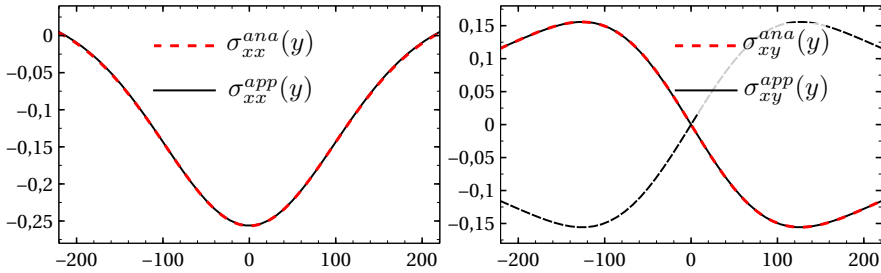


Figure 5.2.: Analytical and approximated distribution of stress components along the vertical domain boundaries.

Unfortunately, the analytical expression of the stresses along the chosen vertical and horizontal lines, due to the simulation domain boundary, are very bulky and useless for the simulation. But with an appropriate approximation approach the necessary functions could be fitted by the desired accuracy. Both the analytical solutions and the approximated stress component distributions are shown for the stress profile along the vertical domain boundary in Figure 5.2 and along the horizontal domain boundaries in Figure 5.3.

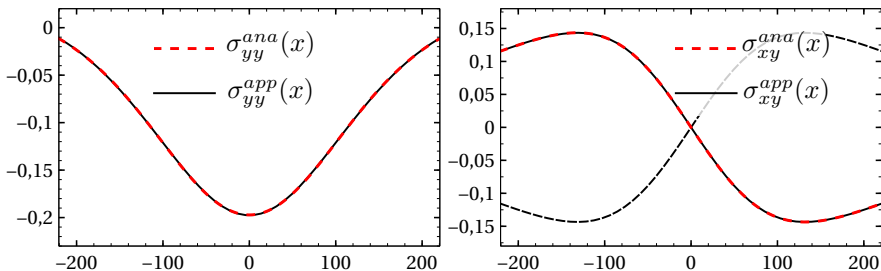


Figure 5.3.: Analytical and approximated distribution of stress components along the vertical domain boundaries.

5. Validation of the presented phase-field elasticity models

Since the orthogonal normal stresses

$$\sigma_{xx}\left(-\frac{L_x}{2}, y\right) = \sigma_{xx}\left(\frac{L_x}{2}, y\right)$$

and

$$\sigma_{yy}\left(x, -\frac{L_y}{2}\right) = \sigma_{yy}\left(x, \frac{L_y}{2}\right)$$

equated at the opposite domain boundaries, the orthogonal shear stresses are asymmetric

$$\begin{aligned}\sigma_{xy}\left(-\frac{L_x}{2}, y\right) &= -\sigma_{xy}\left(\frac{L_x}{2}, y\right), \\ \sigma_{xy}\left(x, -\frac{L_y}{2}\right) &= -\sigma_{xy}\left(x, \frac{L_y}{2}\right).\end{aligned}$$

In order to reduce the influence of the boundary load, the dimension of the simulation domain is chosen in such a way that the distance of the boundary to the essential inclusion is several times longer than its semi-axes.

5.4.2. Functions for the chemical model

While the chemical driving force is written in terms of the grand potential, and is the difference between the corresponding grand chemical potentials, it is more convenient for the theoretical calculation and also for the numerical computations to relate all necessary potentials to a fixed one. Thus, and without loss of generality, the grand chemical potential of the inclusion/inhomogeneity is assumed to be zero, $\omega^I = 0$, and other functions are defined as follows

$$\begin{aligned}\omega^M(\mu) &= 0.0703(\mu + 1.18108)(1 + 0.083215(\mu + 1.18108)), \\ c^I(\mu) &= 0.4682 + 0.0722(\mu + 1.18108), \\ c^M(\mu) &= 0.3979 + 0.0605(\mu + 1.18108).\end{aligned}$$

The intersection of both grand chemical potentials $\omega^M(\mu^{eq}) = \omega^I(\mu^{eq})$ in $\mu^{eq} = -1.18108$ appears for the chemical potential at equilibrium and coincides with the slope of the common tangent of the corresponding free energies, see Figure 2.4.

Note that the required relations in the introduced chemical model in sec. 5.2, which is defined between the grand chemical potentials and the corresponding concentrations

$$\frac{\partial \omega^I(\mu)}{\partial \mu} \neq -c^I(\mu) \quad \text{and} \quad \frac{\partial \omega^M(\mu)}{\partial \mu} \neq -c^M(\mu)$$

is not fulfilled any more. But with the remained equivalence

$$\frac{\partial \omega^I(\mu)}{\partial \mu} - \frac{\partial \omega^M(\mu)}{\partial \mu} = -(c^I(\mu) - c^M(\mu))$$

all required terms in the evolution equations, eq. (5.5) and eq. (5.6), are given in a computationally efficient way. The dimensionless phase-dependent diffusivities in the mass diffusion equation D are assumed to be the same $D^{M,I} = 50$ in both phases. At all simulation domain boundaries, the homogeneous Neumann boundary condition is applied for the mass flux, so that the total composition inside the simulation domain remains constant.

As mentioned, this fact is crucial for the stabilisation of the inlay. The chemical driving force alone is not sufficient to preserve the precipitate, but the mass diffusion controls the shrinking and growing process. The equilibration of these three terms in virtual and real experiments is an interesting issue and should be investigated in future works, see sec. 7, since the counterplay between the different driving forces is a classical topic of the stability theory of dynamical systems.

5.4.3. Matching between capillary, elastic and chemical systems

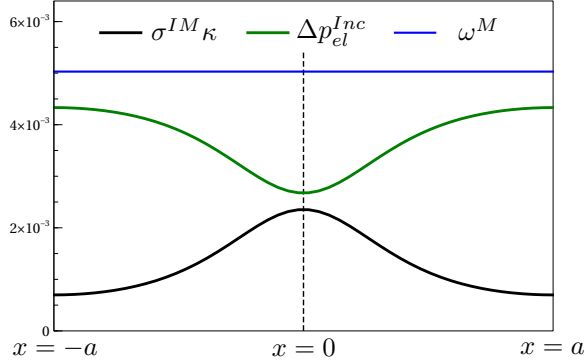


Figure 5.4.: The distribution of the capillary, the elastic and the chemical driving forces along the elliptical interface for the inclusion at the thermodynamic equilibrium eq. (5.11).

Then, knowing the elastic field contribution from eqs. (5.12) - (5.15), the elastic driving force for the inclusion is given in eq. (5.16). The capillary driving force

5. Validation of the presented phase-field elasticity models

is given by the interfacial parameter σ^{IM} and by the local curvature of the ellipse

$$\kappa(x, y) = \frac{1}{a^2 b^2} \left(\frac{x^2}{a^4} + \frac{y^2}{b^4} \right)^{-\frac{3}{2}}.$$

Since all the terms are known, the determination of the required chemical driving force is given by the summation of the previous two terms

$$\omega^M(\mu) = \sigma^{IM} \kappa + \Delta p_{el}^{Inc}(\hat{\boldsymbol{\varepsilon}}). \quad (5.21)$$

The corresponding forces, which act on the boundary of the inclusion are shown along the elliptical interface in Figure 5.4.

By evaluating the right-hand side of the rewritten Gibbs-Thomson equation (5.21), and by equating the result to the grand chemical potential of the matrix, the equilibrium chemical potential, noted as $\bar{\mu}$, is calculated in the straightforward manner, see Figure 5.5.

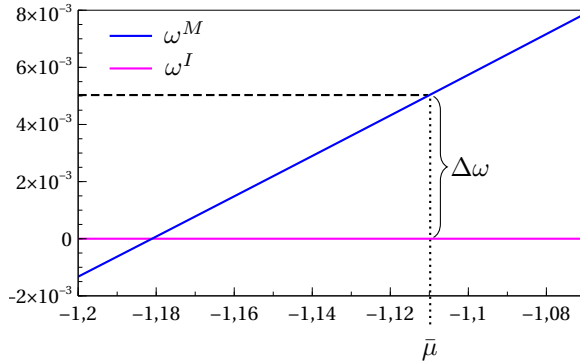


Figure 5.5.: Grand chemical potentials for the inlay ω^I and for the matrix ω^M , in dependence on the chemical potential μ .

Hence, by knowing the chemical potential, the corresponding compositions of the different phases, $c^I(\bar{\mu})$ and $c^M(\bar{\mu})$, are also given by the functions in the previous paragraph 5.2 and the average composition in the whole simulation domain is matched by the condition

$$\bar{c} = c^M(\bar{\mu}) + \frac{\pi ab}{L_x L_y} (c^I(\bar{\mu}) - c^M(\bar{\mu})).$$

Therefore, by the initial filling of the phases in the simulation domain, both with their corresponding compositions, the average concentration should correspond to the theoretical value. Otherwise, the chemical driving force would not match the magnitude in the Gibbs-Thomson equation.

5.4.4. Definition of tested scenarios

In the previous sections, the procedure of the matching simulation parameters is presented. Thus, different testing scenarios can be approved, whereby the elliptical inhomogeneity shape and the resulting elastic fields are identical in all testing cases. Therefore, the mechanical boundary load is the same in all simulation scenarios.

In summary, the prescribed procedure for the determination of the simulation parameters consists of the following steps:

1. Select a stiffness parameters for the inhomogeneity.
2. Calculate the corresponding eigenstrain $\tilde{\epsilon}^{Inh}$ using eq. (5.19).
3. Calculate the elastic driving force at the vertex of the ellipse $\Delta p^{Inh}(a, 0)$ with eq. (5.20) and eq. (5.17).
4. Sum the elastic driving force $\Delta p^{Inh}(a, 0)$ to the local capillary force $\frac{\sigma^{IM}a}{b^2}$ and equate the result to the grand chemical potential, eq. (5.21).
5. Calculate the equilibrium chemical potential $\bar{\mu}$ and the corresponding concentrations.
6. Set an initial filling of the elliptical inhomogeneity in the environmental matrix phase, with the appropriate concentrations due to the average composition.

Since the capillary term remains the same in all scenarios, the modification in the elastic driving force in eq. (5.20), due to the change in the elastic constants and in the corresponding eigenstrain, is given by a summation of the elastic driving force for the inclusion, eq. (5.16), and a constant value. Therefore, the green line in Figure 5.4 is shifted up and down, and the corresponding chemical force, the blue line in Figure 5.4, follows the same shift.

In the following, the nine different theoretical scenarios are investigated in the simulations. The Young modulus and the Poisson ratio in the matrix are uniform in all scenarios. Using varying elastic constants in the inhomogeneity, the corresponding components of the eigenstrain as well as the chemical potential at equilibrium are given in Table 5.1. The fifth testing scenario corresponds to the inclusion.

5. Validation of the presented phase-field elasticity models

sc.	ν^{Inh}	E^{Inh}	$\bar{\varepsilon}^{Inh}_{xx}$ [%]	$\bar{\varepsilon}^{Inh}_{yy}$ [%]	$\bar{\varepsilon}^{Inh}_{zz}$ [%]	$\bar{\mu}$	$\Delta\omega \times 10^{-3}$
1.	0.1	1050	0.295296	0.282251	0.05792	-1.07578	7.4674555
2.	0.1	2100	0.228848	0.184592	0.02896	-1.10179	5.6108655
3.	0.1	3150	0.206699	0.152039	0.0193067	-1.11048	4.9923386
4.	0.25	1050	0.2476	0.243067	0.0	-1.09204	6.3058916
5.	0.25	2100	0.205	0.165	0.0	-1.10995	5.030037
6.	0.25	3150	0.1908	0.138978	0.0	-1.11593	4.6048755
7.	0.3	1050	0.231701	0.230005	-0.0193067	-1.09747	5.9186783
8.	0.3	2100	0.197051	0.158469	-0.00965	-1.11267	4.8366006
9.	0.3	3150	0.1855	0.134624	-0.00643556	-1.11775	4.4755616

Table 5.1.: Parameters for the investigated simulation setups.

As the reader can see, three different Poisson ratios and three different Young modules are used in the combinations. In the test cases, in which the Poisson ratios for the matrix and the inhomogeneity are different, the residual strain component $\tilde{\varepsilon}_{zz}$ is not zero. Furthermore, for a fixed Poisson ratio, but with an increasing Young modulus, the inhomogeneity becomes "harder" than the environmental matrix and the elastic force, and consequently the chemical driving force decreases.

5.5. Simulation results and discussion

For every presented scenario in Table 5.1, six different computational experiments are performed. For the phase-field elasticity model by Schneider et al. in sec. 4.3 as well as for the newly presented formalism in sec. 4.5, three different diffuse interface widths W are applied in the simulations. Thus, the characteristic length scales in the considered simulation scenarios are

$$W\kappa \approx 0.25, 0.5, 0.75,$$

respectively.

The reason of the different interface widths is explained by the dependency of the erroneous interfacial energy, in the case of a thermodynamically inconsistent model. As was shown in the previous section 2, and especially for the chemical system in [47], the interfacial energy density is evaluated for an equilibrated system and is given by the integral throughout the diffuse interface

$$\sigma^{\alpha\beta} = \frac{2\sqrt{\gamma^{\alpha\beta}}}{\pi} \int_0^1 \sqrt{4\gamma^{\alpha\beta}\phi(1-\phi) + W\Delta P(\mu, \varepsilon, \phi, \nabla\phi)} d\phi,$$

whereby the term $\Delta P(\mu, \varepsilon, \phi, \nabla\phi)$ is the erroneous interfacial excess energy, which is scaled by the diffuse interface width W . In the absence of the non-physical and artificial excess energy $\Delta P = 0$, the previous equation reduces to $\sigma^{\alpha\beta} = \gamma^{\alpha\beta}$. Therefore, the real physical surface tension can be applied in the quantitative simulation scenarios.

Otherwise, if also the excess energy $\Delta P \neq 0$ does not vanish because of the incomplete model, its influence can be identified in the simulations by the change in the capillary effects with changing interface width.

In the following figures, 5.6 - 5.14, the equilibrium shapes of the precipitate are presented for the nine scenarios in Table 5.1. Because of the symmetry in the elliptical inhomogeneity, only a representative quarter of the whole shape is presented. The black solid line in all figures represents the theoretical inhomogeneity shape, whereby the red lines on the top and green lines below correspond

5. Validation of the presented phase-field elasticity models

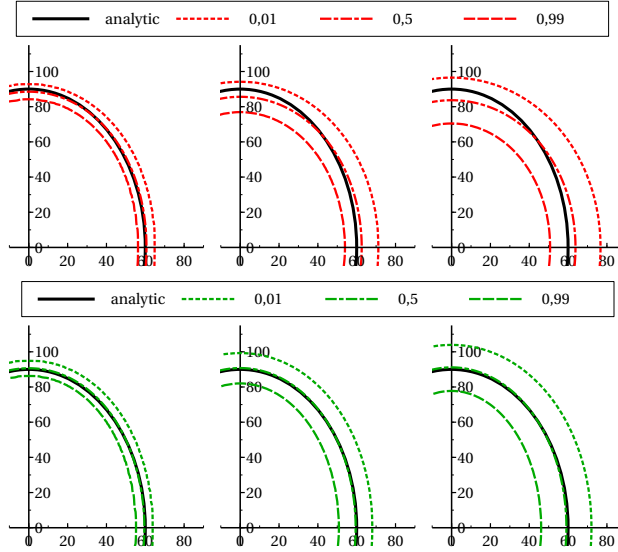


Figure 5.6.: Resulting shapes for the 1. scenario: $\nu^{Inh} = 0.1$ $E^{Inh} = 1050$.

to the models by Schneider et al. in sec. 4.3 and to the new formulation in sec. 4.5, respectively. Since throughout the diffuse interface the phase-field for the precipitate varies smoothly from one to zero, the location of the locus

$$\phi^I = 0.5$$

is the representative position of the sharp interface and is marked by the dashed-dotted lines. In order to highlight the diffuse interface width, the isolines

$$\phi^I = 0.01, \quad \text{and} \quad \phi^I = 0.99$$

are also shown with the dotted and dashed lines, respectively.

As the reader can see in the previous and in the following figures, the inhomogeneity shapes in the simulations, due to the model by Schneider et al. verify a strong dependency on the interface width. In the first (Figure 5.6), fourth (Figure 5.9) and seventh (Figure 5.12) scenarios, an extreme shape change is observed. In these cases, the inhomogeneity is softer than the environmental matrix

$$E^{Inh} = 0.5E^M,$$

and consequently the elastic driving force is higher than in the test cases, in which the Young modulus of the precipitate is the same as in the matrix or

5.5. Simulation results and discussion

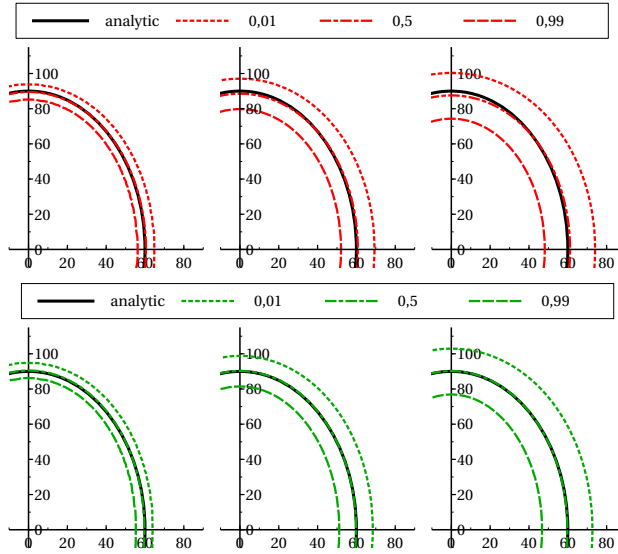


Figure 5.7.: Resulting shapes for the 2. scenario: $\nu^{Inh} = 0.1$ $E^{Inh} = 2100$.

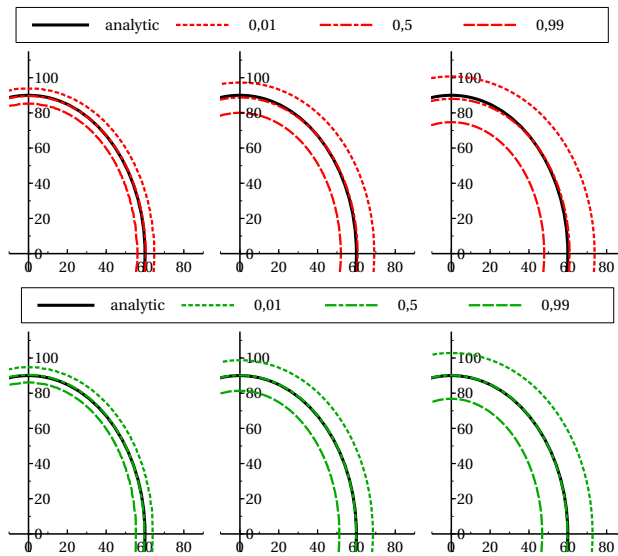


Figure 5.8.: Resulting shapes for the 3. scenario: $\nu^{Inh} = 0.1$ $E^{Inh} = 3150$.

5. Validation of the presented phase-field elasticity models

even higher. This strong dependency is signed by the magnitude of the chemical driving force in Table 5.1. Thus, in the tested scenarios, in which the inhomogeneity has the same (Figures 5.7, 5.10, and 5.13) or a higher elastic modulus (Figures 5.8, 5.11 and 5.14), the elastic driving force is smaller and the erroneous interfacial excess energy in the model by Schneider et al. also seems to be rudimentary, so that the shape change is present, but insignificant.

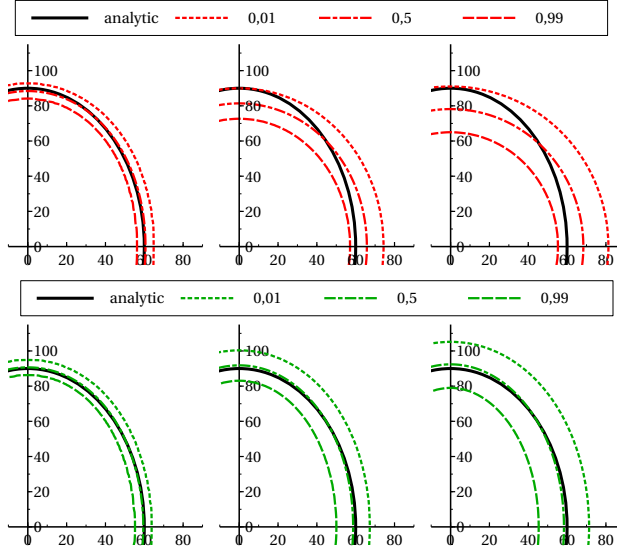


Figure 5.9.: Resulting shapes for the 4. scenario: $\nu^{Inh} = 0.25$ $E^{Inh} = 1050$.

But for this incomplete model, not only the Young modulus is relevant for the high deviation in the computationally resulting shape. Since the elastic and chemical driving forces in the first scenario have the highest tested magnitudes, the biggest mismatch in the simulated precipitate shape is achieved in the fourth and seventh scenario, Figure 5.9 and Figure 5.12. In these test cases, the inhomogeneity is softer and the Poisson ratio is higher than in the first scenario with the highest elastic driving force. Hence, the higher transversal contraction in the inhomogeneity also increases the magnitude of the erroneous interfacial excess energy.

Based on the simulation results, the following findings to the model, which was sketchily presented in sec. 4.3, and was named here as the model by Schneider et al. [30], can be concluded. Since the preceding model was derived based on the mechanical jump conditions, the formulation of the elastic energy in the diffuse

5.5. Simulation results and discussion

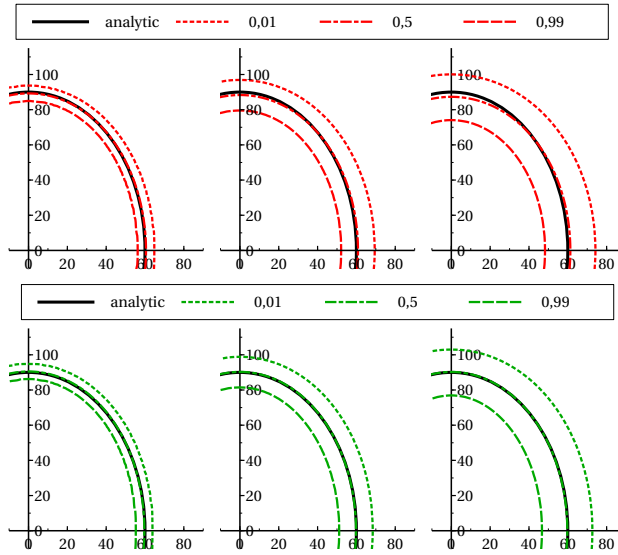


Figure 5.10.: Resulting shapes for the 5. scenario: $\nu^{Inh} = 0.25$ $E^{Inh} = 2100$.

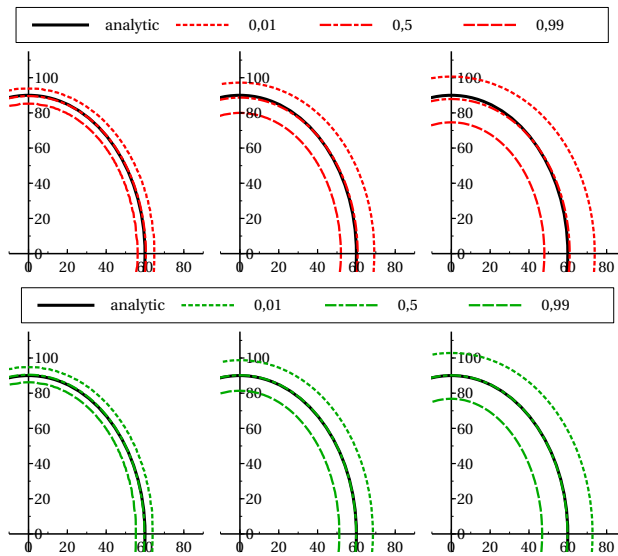


Figure 5.11.: Resulting shapes for the 6. scenario: $\nu^{Inh} = 0.25$ $E^{Inh} = 3150$.

5. Validation of the presented phase-field elasticity models

interface seems to be correct. The derivation of the Cauchy stress, is thermodynamically consistent, as was shown in one-dimensional and two-dimensional simulation results in [30, 91]. But the relevant mismatch of the resulting computational shapes from the expected form emphasizes the deficiencies of the model by Schneider et al.

For the simulation setups with stationary but diffuse interfaces, the calculation of stress follows for quantitative results. The relevant weakness of the model by Schneider et al. is the erroneous calculation of the elastic driving force for the non-stationary diffuse interface by missing the variational derivative of the interpolated strain energy, with respect to the phase-field gradient. Since the term of the elastic driving force in the sharp interface description [82]

$$f_{el}^\alpha(\mathbf{E}^\alpha) - f_{el}^\beta(\mathbf{E}^\beta) - \langle \Sigma^\alpha \mathbf{n}, (\mathbf{E}_n^\alpha - \mathbf{E}^\beta) \rangle$$

formally coincides with the derived expression in the diffuse interface context in [30],

$$(f_{el}^\alpha(\mathbf{E}^\alpha) - f_{el}^\beta(\mathbf{E}^\beta) - \langle \Sigma^\alpha \mathbf{n}, (\mathbf{E}^\alpha - \mathbf{E}^\beta) \mathbf{n} \rangle) h'(\phi),$$

and both correspond to each other in the one-dimensional case, the latter expression incompletely resolves the former formula in a general two- or three-dimensional case with a curved interface and with non-constant interfacial strain. See Figure 5.12 for a comparison between the numerical and analytical results.

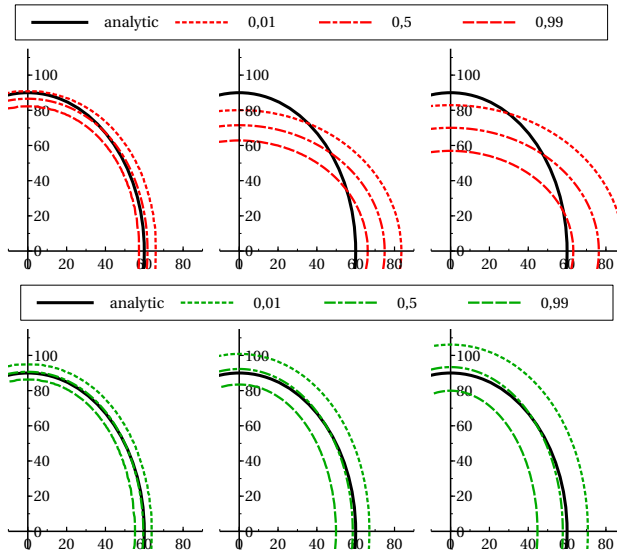


Figure 5.12.: Resulting shapes for the 7. scenario: $\nu^{Inh} = 0.3$ $E^{Inh} = 1050$.

5.5. Simulation results and discussion

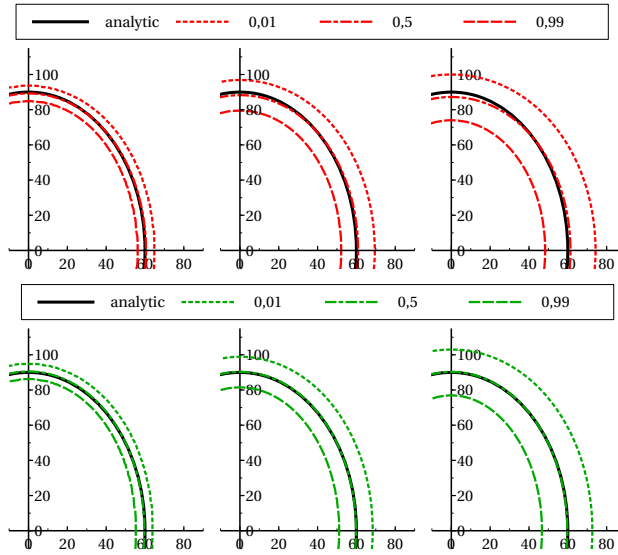


Figure 5.13.: Resulting shapes for the 8. scenario: $\nu^{Inh} = 0.3$ $E^{Inh} = 2100$.

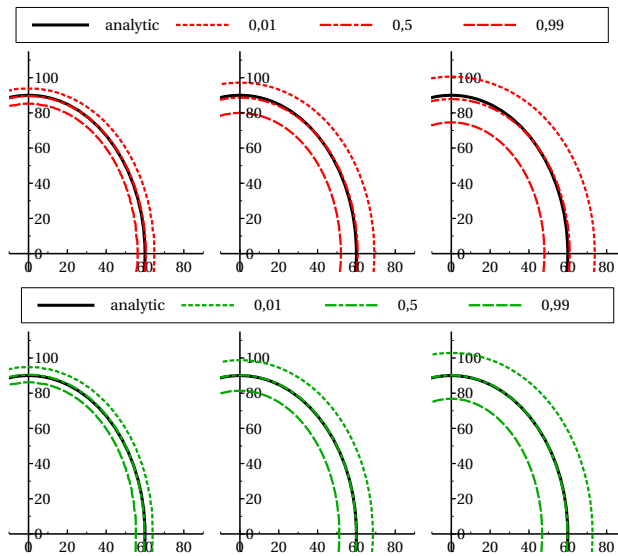


Figure 5.14.: Resulting shapes for the 9. scenario: $\nu^{Inh} = 0.3$ $E^{Inh} = 3150$.

5. Validation of the presented phase-field elasticity models

In the phase-field model, the derivation of the driving force for the phase transformation basically consists of two terms: the one is the variational derivative with respect to the phase-field variable and the second is the divergence of the variational derivative with respect to the phase-field gradient

$$\frac{\delta}{\delta\phi} = \frac{\partial}{\partial\phi} - \nabla \cdot \frac{\partial}{\partial\nabla\phi}.$$

And although the formulation of the interpolated strain energy in eq. (4.11) explicitly and implicitly depends on the phase-field gradient, the second term was argued away because of the formal unhandiness of the model. The result of this drawback is revealed by the mismatching shapes in the presented scenarios.

In contrast to the significantly deviating precipitate shapes in some scenarios for the model by Schneider et al., the simulation results for the alternatively formulated model in sec. 4.4 and sec. 4.5 show an excellent agreement with the theoretical predictions in all considered testing scenarios. Except for the fourth and seventh scenarios, Figure 5.9 and Figure 5.12, the theoretical sharp interface boundary is amazingly overlapped by the representative phase-field locus of $\phi = 0.5$. Even in the test cases, in which the representative location curve in the diffuse interface does not ideally match the sharp interface, the deviation of the resulting shape is insignificant.

In summary, the exceptional conformity of the simulated shapes and of the theoretical predictions is highly encouraging. Additional to the coincidental, final formations of the precipitate, the relevant elastic and chemical fields should also match quantitatively. The resulting chemical potentials are presented for three selected scenarios, for the inclusion in Figure 5.10, for the third scenario in Figure 5.8, with an excellent shape agreement, and for the seventh scenario with maximal deviation, Figure 5.12. In Table 5.2 the final constant chemical potential in the simulation domain is listed. Since the characteristic length scale of zero corresponds to the sharp interface solution, the marginal spread of smaller than 1‰ in the simulated chemical potentials is awesome. Remarkable is not only the perfect accuracy, but also a marginal dependence on the diffuse interface width.

Motivated by the excellent match in the theoretical and computational chemical potentials in Table 5.2, and therefore by the quantitative chemical driving force in the simulations, the minimal mismatch in the precipitate shape, for example in the seventh scenario (bottom figures in Figure 5.12), should be explained by a deviation in the elastic force, which compensates the deviating capillary driving force, as a result of the modified form. Since all resulting simulated inhomogeneities recapitulate the sharp interface for the thin diffuse interface width ($W\kappa = 0.25$), the distribution of elastic fields, due to the characteristic lengths of $W\kappa = 0.5$ and $W\kappa = 0.75$ are presented for the third and seventh

$W\kappa$	μ^{eq}		
	3. scenario	5. scenario	7. scenario
0	-1.11048	-1.10995	-1.09747
0.25	-1.11084	-1.1104	-1.0981
0.50	-1.11076	-1.11027	-1.09801
0.75	-1.11076	-1.11024	-1.0984

Table 5.2.: Final constant chemical potential for the chosen simulation scenarios and in dependence on the diffuse interface width.

testing scenarios. Figures 5.15 and 5.16 show the profiles of the orthogonal normal stress components along the symmetry axes, for the third and seventh test cases, respectively. These two scenarios represent both extremes in the simulation study as a scenario with the best and with the worst result.

In both figures, Figure 5.15 and Figure 5.16, the stress fields along the semi-axes match well with the analytical stress distribution. In the inhomogeneity, the computational constant stress, and consequently the strain distributions quantitatively replicate the theoretical predetermination. Additionally, a great agreement is also observed in the stress field distribution in the surrounded matrix. Since all stress components change smoothly inside the diffuse interface, as expected, the strong jumps of the inhomogeneous variables in the sharp interface description are not reproduced in the simulation.

In the worst case, the seventh scenario with the highest diffuse interface width, the relative deviation of the orthogonal normal stress components from the analytical value is presented in Figure 5.17. Different tendencies in the appropriate components are observed. Since the magnitude of the stress component σ_{xx} is smaller than the analytical value by approximately 4%, the magnitude of the component σ_{yy} is approximately 2% larger than its theoretical counterpart. This can be explained by the elongated resulting shape of the inhomogeneity, and therefore by the deviation in the numerical semi-axes of the elliptical precipitate. Hence, the dimensionless axis ratio t increases and the corresponding trend of the decreasing σ_{xx} and increasing σ_{yy} is also given in eq. (5.13). The relative deviation of the plane orthogonal stress σ_{zz} as well as the shear stress component, both at ppm level, are insignificant.

Note that the resulting elastic energy in the inhomogeneity for the seventh scenario and with the characteristic length scale of $W\kappa = 0.75$ deviates by approximately 10% from the analytical value. These extreme values of $W\kappa = 0.25, 0.5, 0.75$ were only used for the validation of the models and in order to identify the presence of the interfacial excess energy. But it should be men-

5. Validation of the presented phase-field elasticity models

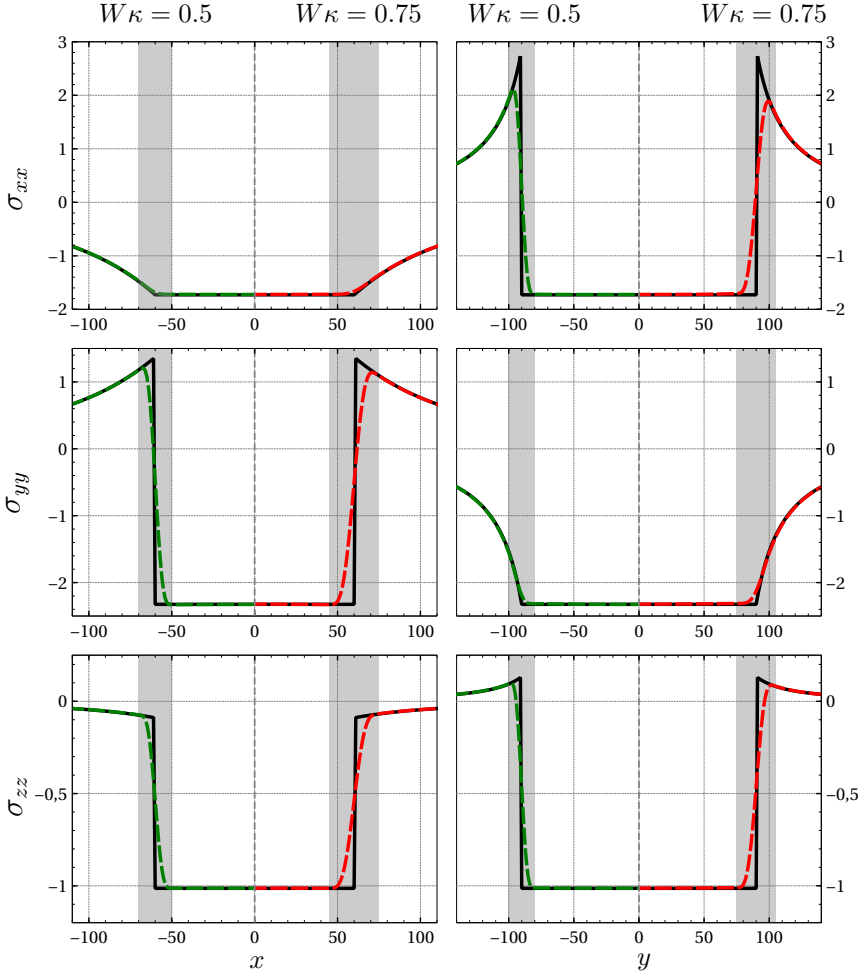


Figure 5.15.: Orthogonal normal stresses, along the x -axes on the left and y -axes on the right, for the third test scenario, Table 5.1, σ_{xx} at the top, σ_{yy} in the middle and σ_{zz} at the bottom. Black, green and red lines correspond to the analytical and to numerical solutions with the characteristic lengths of $W\kappa = 0.5$ and $W\kappa = 0.75$, respectively. Grey areas sign the corresponding diffuse interface.

tioned that in the simulations of real material and manufacturing processes, the interface width should be used one order smaller than the interfacial curvature because of the influence on the kinetic effects. This drawback could also be

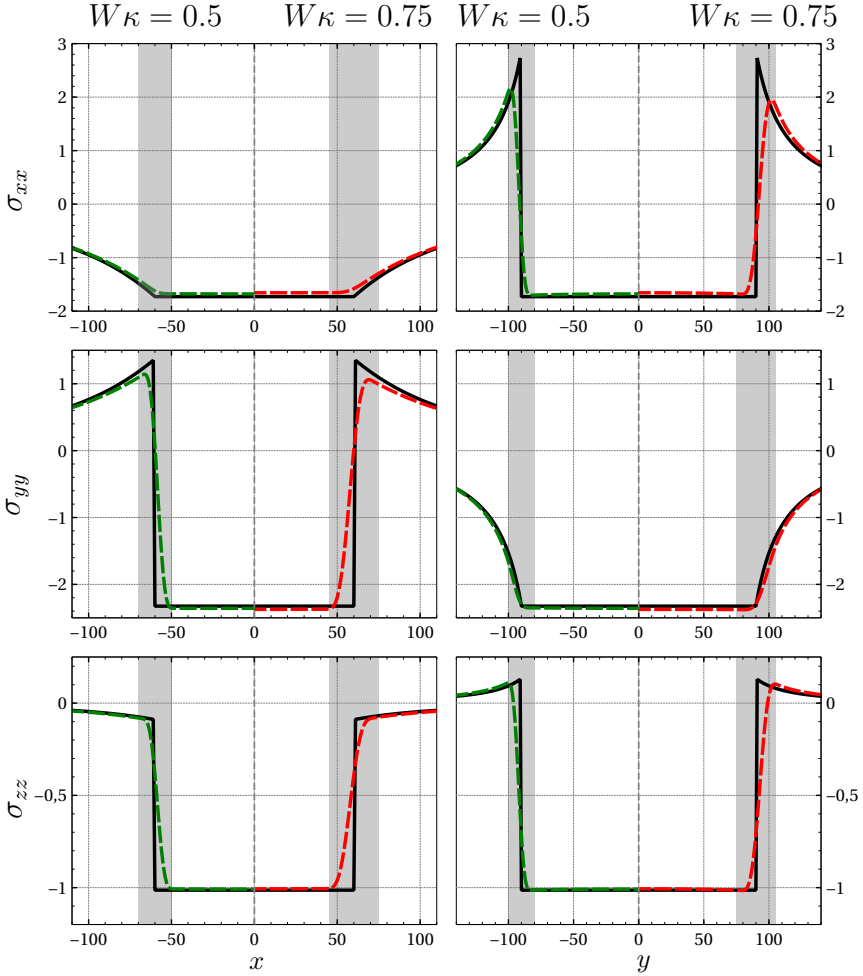


Figure 5.16.: Orthogonal normal stresses, along the x -axes on the left and y -axes on the right, for the seventh test scenario, Table 5.1, σ_{xx} at the top, σ_{yy} in the middle and σ_{zz} at the bottom. Black, green and red lines correspond to the analytical and to numerical solutions with the characteristic lengths of $W\kappa = 0.5$ and $W\kappa = 0.75$, respectively. Grey areas sign the corresponding diffuse interface.

removed, but it requires an asymptotic analysis, which should be a topic for a future work.

5. Validation of the presented phase-field elasticity models

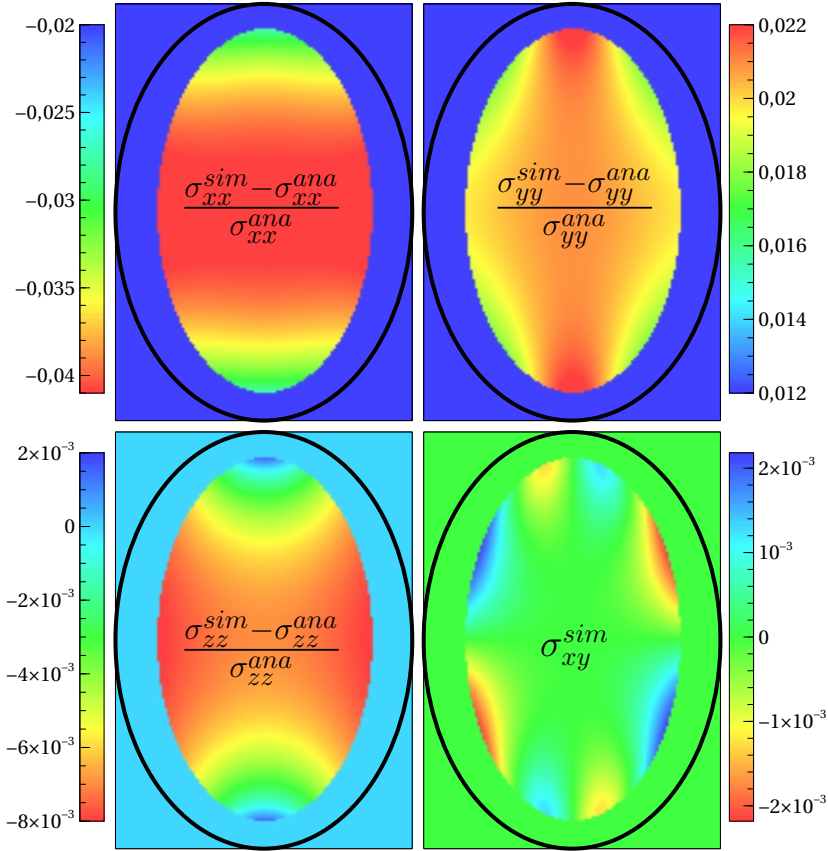


Figure 5.17.: Relative deviation from the analytical value of the orthogonal normal stresses and the shear stress in the inhomogeneity for the seventh scenario and for the characteristic length $W\kappa = 0.75$.

5.6. Conclusion

In summary, the following statements could be made about the simulation results due to the renewed model. In all testing scenarios and in all corresponding simulations, the finally equilibrated precipitate shape matches excellent for the most test cases. The highest, but insignificant form deviation from the theoretical shape is observed in the simulation scenarios, in which the previous model totally fails, see Figure 5.9 and Figure 5.12. Even for these critical scenarios, the resulting, constantly equilibrated chemical potential agrees with the appropriate

5.6. Conclusion

analytical values, see Table 5.2. A relative error, smaller than 1%, is negligible in all simulations. Finally, the distribution of the elastic fields insignificantly changes from scenario to scenario in all simulations. Furthermore, the distribution of the stress components in the inhomogeneity as well as in the matrix replicate the analytical predictions in the bulk phases. The incorporation of an additional term in the driving force, which was missed in the model by Schneider et al., significantly improves the quality of the phase-field model with elastic driving force.

6. Conclusion of the thesis

The thesis consists of two different parts, which differ in the fundamental assumption of the approach. Since the phase-field model of the grain evolution, in the first part of this thesis, is qualitative and was formulated ad hoc, in similarity to the equilibrated processes, the newly derived elasticity phase-field model in the second part strictly fulfilled the assumptions of the equilibrium thermodynamics and the requirement to the application of the variational approach, in order to derive the evolution equations.

In spite of the fact that the phase-field model of welding is contextually formulated, promising simulation results are presented. The grain growth, the grain nucleation in the weld as well as the grain coarsening in the heat-affected zone and in the solidified weld were all qualitatively resolved. The grain growth into the melt was modelled with isotropic surface tension parameters and with the chemical driving force, due to the difference in the free energies of the solid and liquid phases. The mobility of the grain-liquid interface was determined in such a way that the kinetic undercooling of the moving grain boundary consisted of approximately 10K. In order to simulate the grain coarsening, the capillary force was chosen exclusively as the driving force of the solid-solid phase transformation, due to the surface energy minimisation. The temperature dependence of the mobility for the solid-solid phase transformations was chosen with respect to the basic Arrhenius approach. The model for the grain genesis in the weld was formulated in the algorithmic manner, but related to the fundamental quantities in the homogeneous and heterogeneous nucleation models as the standard textbook theories. Thus, different grain structures were achieved by the variation of the moving temperature field and by the modification of the parameters in the nucleation model. The simulation results corresponded to the imaginations based on the existing textbook theories and showed a qualitative match with the real experiments.

In the second part of this thesis, both the derivation of a quantitative elasticity phase-field model as well as its validation both are the main topics of this thesis. Since there exist different models, all of them are thermodynamically inconsistent, as was shown in our recent work [30], and by realising the reason for the defects, we presented a new approach, but also with some remaining drawbacks. In this thesis, the formal, mathematical and thermodynamical defects of the model were removed. A novel formalism is based on the mechanical

6. Conclusion of the thesis

jump conditions, which are satisfied at a coherent interface of two solid phases, and was firstly written in a general tensor notation. After the formulation of the phase-corresponding elastic energies, depending on the mechanical homogeneous variables, the interpolated elastic energy in the diffuse interface was reformulated to depend solely on the system variables. By this modification, all required quantities, such as the Cauchy stress tensor and the elastic driving force, both were derived with respect to the variational approach and were explicitly written. The main results of the model in the tensor notation were rewritten for the Voigt notation, whereby the different definitions of the Voigt stress and Voigt strain vectors were observed. The relevant computational simplifications in the determination of all required quantities during the simulation were presented for elastic isotropic materials. It should also be mentioned that the expressions of the interpolated elastic energy and of the Cauchy stress both are equivalent in the model by Schneider et al. and in this model. But the elegant mathematical and obvious formulation of the derived terms as well as the more efficient computational performance of the novel approach are beneficial, in contrast to the bulky formulation in [30]. The simplicity of the presented model allowed to straightforwardly expand the derived approach for a multiphase-field model.

Finally, the model by Schneider et al. and the newly derived model were used in the simulations for the elliptical Eshelby inclusion. By exploiting the equivalent inclusion method, different simulation scenarios were defined for the validation of the models. Since the model without the variational derivative, with respect to the phase field gradient, totally fails in some test cases, the thermodynamically and mechanically consistent phase-field model, derived in this work, showed excellent agreement with the analytical prescriptions in all analysed properties and in all simulations.

7. Outlook

As the thesis consists of two parts, phase-field modelling of welding and of the elasticity-dependent phase transformations, both models could be coupled, in future works, in order to simulate the residual stresses in the weld sample and to explain how the distribution of the eigenstresses depends on the welding processing parameters, due to the thermal expansion and by volume changing phase transformations, and how it influences the nucleation process. Obviously, both models also have the potential to be expanded separately from each other.

7.1. Phase-field model of welding

Thus, in future works, this phase-field model of welding should also be applied to three-dimensional simulations. Because of large simulation domains ($\sim 10^9$ cells), the virtual experiments will be performed on super computers. As is also the case in this thesis, the material, physical, and process parameters will be used in the simulations, but the nucleation model could be adopted on real material processes. Thus, for example, the critical nucleation radius and the nucleation amplitude are dependent on the local temperature values, but could be chosen more accurately. Furthermore, the constant probability of the nucleation event, which relates to the nucleation rate in the classical text book nucleation theories, should be chosen temperature dependent, too. Moreover, the local cooling rate, which is calculable by using the temperature gradient and the welding velocity, is a decisive quantity for the nucleation. In summary, the nucleation parameter, the critical nucleation radius and the nucleation rate should depend explicitly on the local temperature value, on the liquid phase fraction and also on the local cooling rate.

The incorporation of the induced melt flow in two-dimensional as well in three-dimensional simulations could also be applied in further works. Moreover, in order to realise more realistic scenarios, the usage of anisotropic interfacial energy will influence both the grain growth of preferred grains and also the nucleation process in the weld bath. The anisotropic interfacial energy can also depend on temperature.

7. Outlook

If the virtual experiments recapitulate the real grain structures in the weldments, a comparison of the simulation results and the results of real experiments allows to assess the model and the relevance of the incorporated physical effects in the mathematical description. Furthermore, the matching in both real and virtual experiments approves the human understanding of the physical process during the manufacturing actions. On the other hand, by enforcing a series of simulations with varying parameters, and by comparing the results to the real experiments, the unknown parameters or parameters, which are difficult to access, could be estimated on the basis of simulation results. Obviously, the usage of computer-assisted experiments opens broad possibilities in the design of new materials.

7.2. Phase-field model of elasticity-dependent phase transformations

The presented phase-field model of elasticity-induced phase transformations has an awesome potential for the applications and for the extensions, but should firstly be shared with the scientific community. Therefore, the presented results are planned to be published. Based on this quantitative model, different theoretical or experimental setups could be reproduced in the simulations with two or more phases, already on super computers. Only some possible studies are mentioned.

One of the interesting theoretical and numerical topics for the future study was observed during the preparation of the test cases for the validation of the models in sec. 5. In the simulation scenario, in which the Young modulus of the inhomogeneity is one tenth of the Young modulus in the matrix, the shape of the precipitate is unstable, and the following shape evolution occurs, see Figure 7.1.

Other shape instabilities could also be analysed by using the quantitative elasticity phase-field model. One example is the spheroidization of perturbed rods [92], see Figure 7.2 and the corresponding Rayleigh¹ criterion, which could be analysed in dependence of the external load or of the residual stress in the rod.

Furthermore, since the presented phase-field model in sec. 5 consists of a chemical model and a model for small deformations, the total Helmholtz free energy was modelled additively by these two constituents,

$$f(c, \mathbf{E}, \phi, \nabla\phi) = f_{el}(\mathbf{E}, \phi, \nabla\phi) + f_{el}(c, \phi).$$

¹John William Strutt, 3. Baron Rayleigh, English physicist, Nobel laureate in Physics, 1904. Craters on Mars and the Moon are named in his honour.

7.2. Phase-field model of elasticity-dependent phase transformations

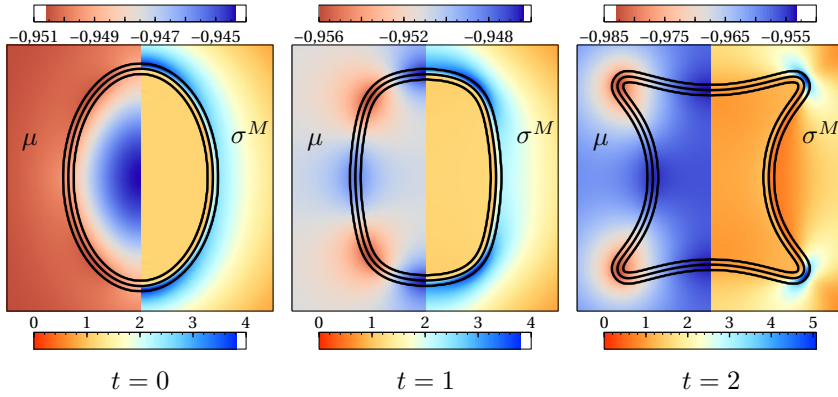


Figure 7.1.: Shape evolution of the unstable precipitate with the Young modulus ten times smaller than the Young modulus in the matrix. Solid lines correspond to the phase-field isolines $\phi = 0.01, 0.5, 0.99$. The density plots on the left side and on the right side of every image represent the chemical potential and the von Mises stress distribution, respectively.

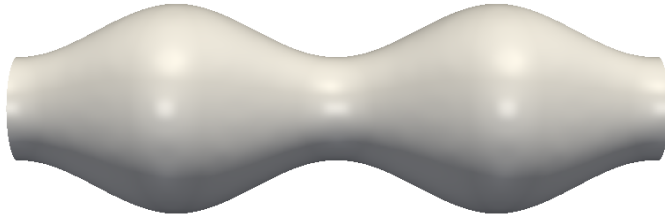


Figure 7.2.: A rod perturbed with harmonic disturbance.

In future work, both models could be combined by the implicit manner. For example, on the one hand, the eigenstrain and/or the stiffness tensor of a solid phase could depend on the composition and/or temperature; on the other hand, the diffusivity constant in the mass diffusion equation could depend on local stress distribution. Nevertheless, the application of this approach requires a foregoing analysis, because the homogeneous chemical and mechanical quantities

7. Outlook

are dependent on each other

$$\mu = \frac{\delta f^\alpha(c, \mathbf{E})}{\delta c}$$
$$\boldsymbol{\Sigma}_n = \mathcal{N}(\nabla\phi) : \frac{\delta f^\alpha(c, \mathbf{E})}{\delta \mathbf{E}}$$

and consequently, the inversion of two previous equations to

$$c^\alpha(\boldsymbol{\Sigma}_n, \mu) = ?$$
$$\mathbf{E}_n^\alpha(\boldsymbol{\Sigma}_n, \mu) = ?,$$

for a formulation of a thermodynamically consistent free energy interpolation and for the respective variational derivatives, could be non-trivial.

Moreover, the directional phase transition for eutectoid phase transformations in dependence of external load, misfit or the residual stresses, is a further topic of investigation, which could be studied by the exploitation of the quantitative elasticity phase-field model. Last, but not least, the quantitative elasticity phase-field model forms a base for extensions with elastoplastic and/or viscoelastic effects.

Appendix

A. Quantitative interpolation functions

The different approaches for the interpolation functions for a two-phase system, with the help of the phase-dependent free energies, are interpolated throughout the diffuse interface. The typical examples are

$$\begin{aligned} h_\alpha^0(\phi_\alpha) &= \phi_\alpha, & \forall \alpha \in [1, N], \\ h_\alpha^1(\phi_\alpha) &= \phi_\alpha^2(3 - 2\phi_\alpha), & \forall \alpha \in [1, N], \\ h_\alpha^2(\phi_\alpha) &= \phi_\alpha^3(10 - 15\phi_\alpha + 6\phi_\alpha^2), & \forall \alpha \in [1, N]. \end{aligned}$$

The disadvantage of the interpolation function h_α^0 is the discontinuity of the derivative, with respect to the phase-field variable on $\phi_\alpha = 0$ or $\phi_\alpha = 1$. Since the appropriate derivatives for the functions h_α^1 and h_α^2 are continuous, they do not sum up to one for a general multiphase case

$$\sum_{\alpha=1}^{N>2} h_\alpha^1(\phi_\alpha) \neq 1 \quad \text{and} \quad \sum_{\alpha=1}^{N>2} h_\alpha^2(\phi_\alpha) \neq 1.$$

In [47], this is also the motivating starting point of the modification of the previous functions to

$$\begin{aligned} \tilde{h}_\alpha^1(\phi) &= \phi_\alpha^2(3 - 2\phi_\alpha) + c_\alpha^1(\phi) \\ \tilde{h}_\alpha^2(\phi) &= \phi_\alpha^3(10 - 15\phi_\alpha + 6\phi_\alpha^2) + c_\alpha^2(\phi) \end{aligned}$$

using additive terms $c_\alpha^{1,2}(\phi)$, which will correct the summation. Alternative functions are presented in [85] as

$$h_\alpha^3(\phi) = \frac{\phi_\alpha^2}{\sum_{\beta=1}^N \phi_\beta^2}.$$

In the discussion with the fellows M. Selzer and D. Schneider, and motivated by the form of the function h_α^3 , an alternative approach is suggested, which will remove the summation drawback.

For a strong monotonic function $\bar{g}_\alpha(\phi_\alpha)$, which only depends on one phase-field parameter and which has the following properties: $\bar{g}_\alpha(\phi_\alpha = 0) = 0$ and

A. Quantitative interpolation functions

$g'_\alpha(\phi_\alpha = 0) = 0$, $\bar{g}_\alpha(\phi_\alpha = 1) < M$ and $\bar{g}'_\alpha(\phi_\alpha = 1) < L$, with any positive constants M and L , the summation is noted as

$$\bar{G}(\phi) = \sum_{\beta=1}^N \bar{g}_\beta(\phi_\beta).$$

The definition of the interpolation function $h_\alpha(\phi)$, which is induced by the corresponding function \bar{g}_α , writes as

$$h_\alpha(\phi) = \frac{\bar{g}_\alpha(\phi_\alpha)}{\bar{G}(\phi)}.$$

All required properties, which are usually provided, are satisfied. The summation to one follows by the construction with $h_\alpha(\phi_\alpha = 0) = 0$ and $h_\alpha(\phi_\alpha = 1) = 1$. Furthermore, the monotonic shape of $h_\alpha(\phi)$ follows by the usage of

$$\frac{\partial}{\partial \phi_\alpha} \sum_{\beta=1}^N h_\alpha(\phi) = \frac{\partial}{\partial \phi_\alpha} 1 = 0 \rightarrow \frac{\partial h_\alpha(\phi)}{\partial \phi_\alpha} = \bar{g}'_\alpha(\phi_\alpha) \sum_{\beta \neq \alpha}^N \frac{\bar{g}_\beta}{\bar{G}^2} \geq 0.$$

Even though the function and its derivative were assumed to be bounded on $\phi_\alpha = 1$, the respective derivative of the appropriate function $h'_\alpha(\phi_\alpha = 1) = 0$, vanishes,

$$\lim_{\phi_\alpha \rightarrow 1} h'_\alpha(\phi_\alpha) < L \lim_{\phi_\alpha \rightarrow 1} \sum_{\beta \neq \alpha} \frac{\bar{g}_\beta}{\bar{G}^2} = \frac{L}{M^2} \lim_{\phi_\alpha \rightarrow 1} \sum_{\beta \neq \alpha} \bar{g}_\beta = \frac{L}{M^2} \underbrace{\sum_{\beta \neq \alpha} \lim_{\phi_\beta \rightarrow 0} \bar{g}_\beta}_{=0} = 0.$$

In the next step, the interpolated free energy in the diffuse interface generally writes as

$$f(\phi, \mathbf{s}) = \sum_{\alpha=1}^N f^\alpha(\mathbf{s}) h_\alpha(\phi) = \frac{1}{\bar{G}(\phi)} \sum_{\alpha=1}^N f^\alpha(\mathbf{s}) \bar{g}_\alpha(\phi_\alpha),$$

and the variational derivative, with respect to the phase-field function ϕ_α , is consequently given as

$$\frac{\partial f(\phi, \mathbf{s})}{\partial \phi_\alpha} = \frac{\bar{g}'_\alpha(\phi_\alpha)}{\bar{G}(\phi)} \left(f^\alpha(\mathbf{s}) - f(\phi, \mathbf{s}) \right).$$

B. Required tensors for the Eshelby inclusion

In chapter 5, the used Eshelby tensor \mathbf{S} , for an elliptical inclusion, as well as the auxiliary tensor $\mathbf{H}(x, y)$ are explicitly given to maintain the self-consistency in this thesis, and are borrowed from [86], but are written in terms of the semi-axes ratio, $t = b/a$, with the Poisson ratio ν and with the shear modulus G .

$$\mathbf{S}(t, \nu) = \begin{pmatrix} \frac{2t(1+t) + \frac{1}{1-\nu}}{2(1+t)^2} & \frac{t-2t(1+t)\nu}{2(1+t)^2(-1+\nu)} & \frac{t\nu}{1+t-\nu-t\nu} & 0 \\ \frac{t-2(1+t)\nu}{2(1+t)^2(-1+\nu)} & \frac{2(1+t) + \frac{1}{1-\nu}}{2(1+t)^2} & \frac{\nu}{1+t-\nu-t\nu} & 0 \\ 0 & 0 & 0 & 0 \\ 0 & 0 & 0 & 1 + \frac{t}{(1+t)^2(-1+\nu)} \end{pmatrix}.$$

To derive the proportionality tensor $\mathbf{H}(x, y)$, auxiliary quantities are needed. For completeness, we write all the expressions. In accordance with the work of X. Jin et. al [86], for the points outside the ellipse ($\frac{x^2}{a^2} + \frac{y^2}{b^2} \geq 1$), there exists such a λ that fulfils

$$\frac{x^2}{a^2 + \lambda} + \frac{y^2}{b^2 + \lambda} = 1, \quad (\text{B.1})$$

with $\lambda = \frac{1}{2} \left((x^2 - a^2) + (y^2 - b^2) + \sqrt{((x^2 - a^2) - (y^2 - b^2))^2 + 4x^2y^2} \right)$. Further auxiliary quantities, ρ_a and ρ_b , are defined as follows

$$\rho_a = \frac{a}{\sqrt{a^2 + \lambda}}, \quad \rho_b = \frac{b}{\sqrt{b^2 + \lambda}}, \quad (\text{B.2})$$

and the components of the normal vector, at the imaginary ellipse given through the eq. (B.1), are given by

$$n_x = \frac{m_x}{\sqrt{m_x^2 + m_y^2}}, \quad n_y = \frac{m_y}{\sqrt{m_x^2 + m_y^2}}, \quad (\text{B.3})$$

with

$$m_x = \frac{x}{a^2 + \lambda}, \quad m_y = \frac{y}{b^2 + \lambda}. \quad (\text{B.4})$$

B. Required tensors for the Eshelby inclusion

With the predefined variables in eqs. (B.2), and with the components of the normal vector in eq. (B.3), the symmetric proportionality tensor $\mathbf{H}(x, y)$ in eq. (5.14) is then given as

$$\mathbf{H}(x, y) = \frac{G\rho_a\rho_b}{1 - \nu^{mat}} \begin{pmatrix} H_{11}(x, y) & H_{12}(x, y) & H_{13}(x, y) & H_{14}(x, y) \\ H_{12}(x, y) & H_{22}(x, y) & H_{23}(x, y) & H_{24}(x, y) \\ H_{13}(x, y) & H_{23}(x, y) & 0 & H_{34}(x, y) \\ H_{14}(x, y) & H_{24}(x, y) & H_{34}(x, y) & H_{44}(x, y) \end{pmatrix}.$$

With $A(x, y) = \rho_b + t\rho_a$ and $L(x, y) = \rho_a^2 n_y^2 + \rho_b^2 n_x^2$, and in the simplified manner, the matrix elements write as

$$\begin{aligned} H_{11} &= \frac{t\rho_a}{A} \left(1 + \rho_a^2 \left(1 + \frac{\rho_b}{A} \right) \right) - n_x^2 \left(2 \left(1 - (2 - \rho_a^2) n_y^2 \right) + \rho_a^2 + L(3 - 4n_x^2) \right), \\ H_{22} &= \frac{\rho_b}{A} \left(1 + \rho_b^2 \left(1 + \frac{t\rho_a}{A} \right) \right) - n_y^2 \left(2 \left(1 - (2 - \rho_b^2) n_x^2 \right) + \rho_b^2 + L(3 - 4n_y^2) \right), \\ H_{44} &= H_{12} = \frac{\rho_a}{A} \left(t + \frac{\rho_a \rho_b^2}{A} \right) - 4n_x^2 n_y^2 - L(1 - 4n_x^2 n_y^2), \\ H_{14} &= n_x n_y \left(1 - 2\rho_a^2 n_y^2 + 4n_x^2 (L - 1) - L \right), \\ H_{24} &= n_x n_y \left(1 - 2\rho_b^2 n_x^2 + 4n_y^2 (L - 1) - L \right), \\ H_{13} &= 2\nu \left(\frac{t\rho_a}{A} - n_x^2 \right), \quad H_{23} = 2\nu \left(\frac{\rho_b}{A} - n_y^2 \right), \quad H_{34} = -2\nu n_x n_y. \end{aligned}$$

C. Computational efficiency of the presented models

Here I want to demonstrate the computational efficiency of the newly presented model. Doing so, a simple simulation scenario is used, and solely the Cauchy stress calculation is performed, as the only equivalent quantity in both models. The diffuse interface is initially present in the simulation domain and fills approximately half of the total simulation domain, see Figure C.1. Since the right interface is perpendicular to the x -axes, and consequently the phase field gradient and also the normal vector consists only of non-vanishing x -component, the left interface is inclined and the normal vector consists of all non-zero components. Figure C.1 shows a screenshot of the visualisation with the tool `xsimview` in `PACE3D`.

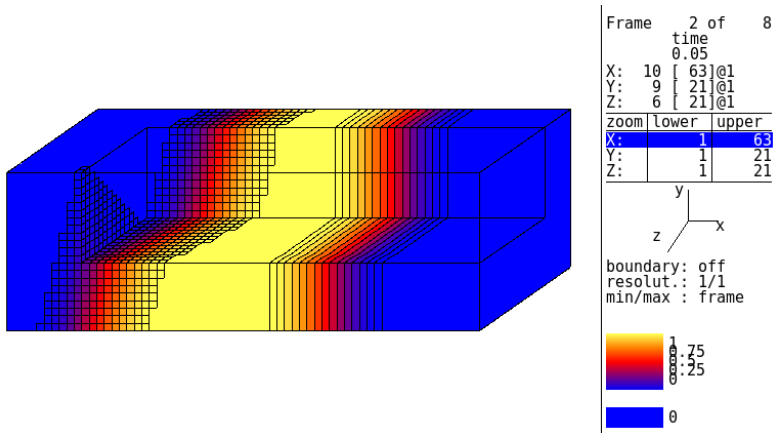


Figure C.1.: Simulation setup for the comparison of the calculation times for both presented models, model by Schneider et al. and a newly presented approach. The screenshot shows the visualisation of the tool `xsimview` in `PACE3D`.

The different colours sign the different phases and the smooth overgrow, which is also marked with the grid lines represent diffuse interface between bulk phases.

C. Computational efficiency of the presented models

The size of the simulation domain as well as the time for the corresponding frames and other useful informations are also presented in this powerful imagination program.

Boundary conditions

As mentioned, only the stress calculation, without any phase-field and/or mass-diffusion evolution, is performed in the simulations. On the right and left boundaries the external boundary load, with constant pressure of

$$\begin{aligned}\text{BOUNDARY.CONST.STRESS.LEFT} &= (2.0, 0.0, 0.0), \\ \text{BOUNDARY.CONST.STRESS.RIGHT} &= (2.0, 0.0, 0.0)\end{aligned}$$

is applied. Further, I apply strain boundary condition on the simulation boundary planes, which are parallel to the tensile direction

$$\begin{aligned}\text{BOUNDARY.CONST.STRAIN.TOP} &= (0.0, -0.004, 0.0), \\ \text{BOUNDARY.CONST.STRAIN.BOTTOM} &= (0.0, -0.004, 0.0), \\ \text{BOUNDARY.CONST.STRAIN.FRONT} &= (0.0, 0.0, -0.004), \\ \text{BOUNDARY.CONST.STRAIN.BACK} &= (0.0, 0.0, -0.004).\end{aligned}$$

Optimisation keys

There are also the following optional optimisation possibilities of the computational stress calculation. Thus, for example, the option with the key name

`SOLIDMECHANICS.EIGENSTRAIN=1`

allows to activate (1) or to deactivate (0) the incorporation of the eigenstrains into the calculation, if the eigenstrains are either present in the simulation scenario or not, respectively. Furthermore, the stress calculation for the elastic isotropic and anisotropic materials is different. This option is controlled with the key

`SOLIDMECHANICS.STIFFNESS.ISOTROPIC=1`.

In the following, different simulations are performed with the material parameters given in the next paragraph

Materials parameters

Since the stiffness tensors are in accordance with the elastic isotropic phases, by deactivating the correspondig key, all matrix elements are used in the computational integration. The outer phase is named β , and its dimensionless Young modulus is $E^\beta = 2000$. The inner phase is named α and its Young modulus varies. Sometimes, it equates to $E^\alpha = E^\beta$ or it is two times higher, $E^\alpha = 2.0 \times E^\beta$. The Poisson ratio

$$\nu^\alpha = \nu^\beta = 0.25$$

is the same for both phases in all test cases. Thus, the different scenarios are also signed by the ratio between both elastic modules, $f = E^\alpha/E^\beta$.

In the case where the eigenstrain option is used, I use the residual strain in α and β phases of the following form

```
SOLIDMECHANICS.EIGENSTRAIN= (ALPHA) (0.002,0.0,0.0,0.0,0.0,0.0),
SOLIDMECHANICS.EIGENSTRAIN= (BETA) (0.0,0.0,0.0,0.0,0.0,0.0).
```

Since the computational performance, and not the final result, is of interest in this study, all simulation parameters and the same numerical scheme is used for the evaluation of the wave equation

$$\rho \ddot{\mathbf{u}} = \nabla \cdot \boldsymbol{\Sigma}. \quad (\text{C.1})$$

The computation of the stress tensor components on the right hand side of the wave equation differs in both models. Thus, the calculation procedure of the Cauchy stress tensor due to the model in sec. 4.3 (old) and due to the newly derived model in sec. 4.4 (new) is applied.

The following different scenarios in Table C.1 are considered.

scenario	1	2	3	4	5	6	7	8
isotrop	1	0	1	0	1	0	1	0
eigenstrain	0	0	1	1	0	0	1	1
ratio f	1	1	1	1	2	2	2	2

Table C.1.: Different simulation scenarios with activated and deactivated optimisation options and with same or different elastic constants in the appropriate phases.

In every simulation, the numerical integration of the wave equation (C.1) appears on one processor and includes 10000 iterations and writing out of 12 frames. The total simulation times for different scenarios are presented in tab, C.2

C. Computational efficiency of the presented models

	1	2	3	4	5	5	6	7
old	164.75	2282	2615	2616	2274	2342	2613	2606
new	128.3	570.5	156.83	604.6	147.50	569.26	176.76	600.7

Table C.2.: Simulation time in seconds of the numerical integration of the wave equation, eq. (C.1) on one processor, with 10000 iterations and 12 frames.

In all considered simulations scenarios, the new stress calculation is faster and also more efficient than the stress calculation for the old model. Since the duration of processing for the first computational scenario, with twin phases can be compared, to other simulation scenarios with different phases, the new stress calculation takes approximately 4 times faster for elastic anisotropic materials and approximately 15 times faster for elastic isotropic materials. Thus, the decrease of the calculation time for elastic isotropic materials by a factor of 4 is also beneficial. Furthermore, an ideal match between the displacement field components for the isotropic and anisotropic test cases is achieved applying the new model.

Bibliography

- [1] H. J. Fahrenwaldt, V. Schuler, and J-Twrdek. *Praxiswissen Schweißtechnik*. Springer Fachmedien, Wiesbaden.
- [2] C. L. Tsai and C. M. Tso. Heat flow in fusion welding. *ASM Handbook, Welding, Brazing, and Soldering*, Vol. 6:7–18, 1993.
- [3] G. Schulze. *Die Metallurgie des Schweißens*. Springer-Verlag, Berlin Heidelberg, 4. edition, 2010.
- [4] H. D. Solomon. Fundamentals of weld solidification. *ASM Handbook, Welding, Brazing, and Soldering*, Vol. 6:p 45–54, 1993.
- [5] D. L. Cocke and A. Clearfield. *Design of New Materials*. Springer US, 1 edition, 1987.
- [6] H. Murakami, T. Ohmura, and T. Nishimura. Recent global trends in structural materials research. *Science and Technology of Advanced Materials*, 14, 2013.
- [7] G. Thomson. *The Inspiration of Science*. Žnanie, Moscow, 1970.
- [8] G. Thomson. The two aspects of science. *Science*, 132:996–1000, 1960.
- [9] K. G. F. Janssens, D. Raabe, E. Kozeschnik, M. A. Miodownik, and B. Nestler. *Computational Materials Engineering*. Academic Press, Burlington, 2007.
- [10] L. D. Landau and E. M. Lifschitz. *Lehrbuch der theoretischen Physik IX. Statistische Physik II: Theorie des kondensierten Zustands*. Europa-Lehrmittel, 1992.
- [11] R. Kobayashi. Modeling and numerical simulations of dendritic crystal growth. *Physica D*, 63:410, 1993.
- [12] A. Karma and W. J. Rappel. Quantitative phase-field modeling of dendritic growth in two and three dimensions. *Phys. Rev. E*, 57:4323, 1998.
- [13] M. Plapp and A. Karma. Eutectic colony formation: A phase-field study. *Phys. Rev. E*, 66:061608, 2002.

Bibliography

- [14] P. Steinmetz, M. Kellner, J. Hötzer, A. Dennstedt, and B. Nestler. Phase-field study of the pattern formation in al–ag–cu under the influence of the melt concentration. *Comp. Mat. Science*, 121:6 – 13, 2016.
- [15] T. Takaki M. Ohno and Y. Shibuta. Variational formulation and numerical accuracy of a quantitative phase-field model for binary alloy solidification with two-sided diffusion. *Phys. Rev. E*, 93:012802, 2016.
- [16] K. Ankit. *Phase-field modeling of microstructural pattern formation in alloys and geological veins*. PhD thesis, Karlsruhe Institute of Technology, IAM-CMS, 2015.
- [17] M. Selzer. *Mechanische und Strömungsmechanische Topologieoptimierung mit der Phasenfeldmethode*. PhD thesis, Karlsruhe Institute of Technology, IAM-CMS, 2014.
- [18] H. Garcke and K. F. LAM. Well-posedness of a Cahn–Hilliard system modelling tumour growth with chemotaxis and active transport. *Eur. J. Appl. Math.*, pages 1–33, 2016.
- [19] H. Emmerich and R. Travasso. Phase-field simulations: Materials science meets biology and medicine. *Phil. Mag.*, 91:1–2, 2011.
- [20] B. Nestler, H. Garcke, and B. Stinner. Multicomponent alloy solidification: Phase-field modeling and simulations. *Phys. Rev. E*, 71:041609, 2005.
- [21] H. Schultz. *Electron Beam Welding*. Woodhead Publishing Series in Welding and Other Joining Technologies. Elsevier Science, 1994.
- [22] Jr. R. W. Messler. *Principles of Welding*. Wiley-VCH Verlag GmbH & Co. KGaA, 2004.
- [23] C. R. Heiple and P. Burgardt. Fluid flow phenomena during welding. *ASM Handbook*, Welding, Brazing, and Soldering, Vol. 6:19–24, 1993.
- [24] J. Goldak, M. Bibby, J. Moore, R. House, and B. Patel. Computer modeling of heat flow in welds. *Metall. Trans. B*, 17(3):587–600, 1986.
- [25] LQ Chen. Phase-field models for microstructure evolution. *Annu. Rev. Mater. Res.*, 32(1):113–140, 2002.
- [26] I. Steinbach and M. Apel. Multi phase field model for solid state transformation with elastic strain. *Physica D*, 217:153–160, 2006.
- [27] R. Spatschek, C. Müller-Gugenberger, E. Brener, and B. Nestler. Phase field modeling of fracture and stress-induced phase transitions. *Phys. Rev. E*, 75(6):1–14, jun 2007.

- [28] C. Mennerich, F. Wendler, M. Jainta, and B. Nestler. A phase-field model for the magnetic shape memory effect. *Arch. Mech.*, 63:549–571, 2011.
- [29] A. Durga, P. Wollants, and N. Moelans. Evaluation of interfacial excess contributions in different phase-field models for elastically inhomogeneous systems. *Model. Simul. Mater. Sci. Eng.*, 21:55018, 2013.
- [30] D. Schneider, O. Tschukin, A. Choudhury, M. Selzer, T. Böhlke, and B. Nestler. Phase-field elasticity model based on mechanical jump conditions. *Comput. Mech.*, 55:887–901, 2015.
- [31] N. Provatas and K. Elder. *Phase-Field Methods in Materials Science and Engineering*. WILEY-VCH Verlag GmbH & Co. KGaA, 2010.
- [32] I. Steinbach. Phase-field models in materials science. *Model. Simul. Mater. Sci. Eng.*, 17:073001, 2009.
- [33] M. Brin and G. Stuck. *Introduction to Dynamical Systems*. Cambridge University Press, 2015.
- [34] S. Boyd and L. Vandenberghe. *Convex Optimization*. Cambridge University Press, 2004.
- [35] R. Rannacher. *Numerische Mathematik*. Lecture notes, Heidelberg University, 2006-2016.
- [36] A. M. Lyapunov. *The general problem of the stability of motion*. 1892.
- [37] J. W. Cahn and J. E. Hilliard. Free energy of a nonuniform system. I. interfacial free energy. *J. Chem. Phys.*, 28:258, 1958.
- [38] A. A. Wheeler, W. J. Boettinger, and G. B. McFadden. Phase-field model for isothermal phase transitions in binary alloys. *Phys. Rev. A*, 45:7424, 1992.
- [39] A. Karma. Phase-field model of eutectic growth. *Phys. Rev. E*, 49:2245, 1994.
- [40] H. Garcke, B. Nestler, and B. Stinner. A diffuse interface model for alloys with multiple components and phases. *SIAM J. Appl. Math.*, 64:775, 2004.
- [41] M. Plapp. Unified derivation of phase-field models for alloy solidification from a grand-potential functional. *Phys. Rev. E*, 84:031601, Sep 2011.
- [42] A. Choudhury and B. Nestler. Grand-potential formulation for multicomponent phase transformations combined with thin-interface asymptotics of the double-obstacle potential. *Phys. Rev. E*, 85:021602, Feb 2012.

Bibliography

- [43] S. G. Kim, W. T. Kim, and T. Suzuki. Phase-field model for binary alloys. *Phys. Rev. E*, 60:7186, 1999.
- [44] M. Nicoli, M. Plapp, and H. Henry. Tensorial mobilities for accurate solution of transport problems in models with diffuse interfaces. *Phys. Rev. E*, 84:046707, 2011.
- [45] J. Ettrich, A. Choudhury, O. Tschukin, E. Schoof, A. August, and B. Nestler. Modelling of transient heat conduction with diffuse interface. *Model. Simul. Mater. Sci. Eng.*, 22:085006, 2014.
- [46] B. Nestler. *Phasenfeldmodellierung mehrphasiger Erstarrung*. Dissertation, RWTH Aachen, 2000.
- [47] A. N. Choudhury. *Quantitative phase-field model for phase transformations in multi-component alloys*. Dissertation, KIT Karlsruhe, 2012.
- [48] I. Loginova, G. Amberg, and J. Ågren. Phase-field simulations of non-isothermal binary alloy solidification. *Acta. Mater.*, 49:573, 2001.
- [49] O. Tschukin, A. Choudhury, and B. Nestler. Comparative investigation of phase-field models based on grand potential and free energy formulations. unpublished.
- [50] S. G. Kim, D. I. Kim, W. T. Kim, and Y. B. Park. Computer simulations of two-dimensional and three-dimensional ideal grain growth. *Phys. Rev. E*, 74:061605, Dec 2006.
- [51] B. Nestler, M. Reichardt, and M. Selzer. *Massive multi-phase-field simulations: methods to compute large grain system*, pages 325–338. Wiley-VCH Verlag GmbH & Co. KGaA, 2009.
- [52] G. I. Tóth, T. Pusztai, and L. Gránásy. Consistent multiphase-field theory for interface driven multidomain dynamics. *Phys. Rev. B*, 92:184105, Nov 2015.
- [53] H. J. Fahrenwaldt, V. Schuler, and J. Twrdek. *Praxiswissen Schweißtechnik*. Springer Fachmedien Wiesbaden, 5 edition, 2014.
- [54] K. J. Matthes and W. Schneider. *Schweißtechnik - Schweißen von metallischen Konstruktionswerkstoffen*. Carl Hanser Verlag, 5. edition, 2012.
- [55] J. R. Davis W. A. Baeslack III and C. E. Cross. Selection and weldability of conventional titanium alloys. *ASM Handbook*, Welding, Brazing, and Soldering, Vol. 6:507–523, 1993.
- [56] F. J. Grist, W. Farrell, and G. S. Lawrence. Power sources for welding. *ASM Handbook*, Welding, Brazing, and Soldering, Vol. 6:36–44, 1993.

- [57] A. Farzadi, M. Do-Quang, S. Serajzadeh, A. H. Kokabi, and G. Amberg. Phase-field simulation of weld solidification microstructure in an al-cu alloy. *Model. Simul. Mater. Sci. Eng.*, 16(6):065005, 2008.
- [58] M Hajhashemi, M Shamanian, and B Niroumand. Optimization and utilization of semisolid casting process for semisolid welding of al-6061 alloy. *J. Adv. Mater. Process.*, 1(3):19–26, 2013.
- [59] H. E. Cline and T. R. Anthony. Heat treating and melting material with a scanning laser or electron beam. *J. Appl. Phys.*, 1977.
- [60] J. Goldak, A. Chakravarti, and M. Bibby. A new finite element model for welding heat sources. *Metall. Trans. B*, 15(2):299–305, 1984.
- [61] J. Guo, P. Le Masson, S. Rouquette, T. Loulou, and E. Artioukhine. Estimation of a source term in a two-dimensional heat transfer problem: application to an electron beam welding, theoretical and experimental validations. *Inverse Probl Sci Eng.*, 15(7):743–763, 2007.
- [62] S. Rouquette, J. Guo, and P. Le Masson. Estimation of the parameters of a Gaussian heat source by the Levenberg–Marquardt method: Application to the electron beam welding. *Int. J. Therm. Sci.*, 46(2):128 – 138, 2007.
- [63] C. L. Chang. *Berechnung der Schmelzbadgeometrie beim Laserstrahlschweißen mit Mehrfokustechnik*. PhD thesis, Stuttgart, 2000.
- [64] V. Povolin. Approximation des temperaturfelded einer schweißprozess-simulation. Student project, Hochschule für Technik und Wirtschaft Karlsruhe, 2012.
- [65] A. Vondrous. *Grain growth behavior and efficient large scale simulations of recrystallization with the phase-field method*. PhD thesis, Karlsruhe Insitute of Technology, IAM-CMS, 2014.
- [66] B. Stinner. *Derivation and Analysis of a Phase Field Model for Alloy Solidification*. Dissertation, Iniversität Regensburg, 2005.
- [67] J. Hötzer, O. Tschukin, M. Ben Said, M. Berghoff, M. Jainta, G. Barthelemy, N. Smorchkov, D. Schneider, M. Selzer, and B. Nestler. Calibration of a multi-phase field model with quantitative angle measurement. *J. Mat. Sci.*, 51(4):1788–1797, 2016.
- [68] M. Apel, B. Böttger, J. Rudnizki, P. Schaffnit, and I. Steinbach. Grain growth simulations including particle pinning using the multiphase-field concept. *ISIJ International*, 49(7):1024–1029, 2009.

Bibliography

- [69] W. Stiller. *Arrhenius Equation and Non-Equilibrium Kinetics: 100 Years Arrhenius Equation*. Mir, Moscow, 2000.
- [70] J. P. Simmons, Y. Wen, C. Shen, and Y. Z. Wang. Microstructural development involving nucleation and growth phenomena simulated with the phase field method. *Mater. Sci. Eng., A*, 365(1–2):136 – 143, 2004.
- [71] A. Karma and W. J. Rappel. Phase-field model of dendritic sidebranching with thermal noise. *Phys. Rev. E*, 60:3614–3625, 1999.
- [72] L. Gránásy, T. Pusztai, and J. A. Warren. Modelling polycrystalline solidification using phase field theory. *J. Phys. Condens. Matter.*, 16(41):R1205, 2004.
- [73] T. Pusztai, G. Tegze, G. I. Tóth, L. Környei, G. Bansel, Z. Fan, and L. Gránásy. Phase-field approach to polycrystalline solidification including heterogeneous and homogeneous nucleation. *J. Phys. Condens. Matter.*, 20(40):404205, 2008.
- [74] M. Daubermann. Simulationsstudien zur Mikrostrukturausbildung beim Schweißprozess eines ferritischen Stahls. Bachelor -Thesis, Karlsruhe Institute of Technology, 2014.
- [75] B. Nestler, O. Tschukin, M. Jainta, M. Daubermann, M. Selzer, V. Widak, J. Hoffmann, and M. Rieth. Virtuelle Material- und Prozessentwicklung am Beispiel der Konstrukturausbildung in Schweißnähten. *Forschungsreport für den Maschinenbau in Baden-Württemberg*, 2014.
- [76] H. Garcke, B. Nestler, and B. Stoth. A multiphase field concept: Numerical simulations of moving phase boundaries and multiple junctions. *SIAM J Appl Math*, 60:295–315, 1999.
- [77] M. J. Cieslak. Cracking phenomena associated with welding. *ASM Handbook, Welding, Brazing, and Soldering*, Vol. 6:88 – 96, 1993.
- [78] P. R. Vishnu. Solid-state transformations in weldments. *ASM Handbook, Welding, Brazing, and Soldering*, Vol. 6:70 – 87, 1993.
- [79] W. Voigt. Über die Beziehung zwischen den beiden Elastizitätskonstanten isotroper Körper. *Ann. Phys.*, 274(12):573–587, 1889.
- [80] A. Reuss. Berechnung der Fließgrenze von Mischkristallen auf Grund der Plastizitätsbedingung für Einkristalle. *Z. Angew. Math. Mech.*, 9:49–58, 1929.
- [81] A. G. Khachaturyan. *Theory of Structural Transformation in Solids*. John Wiley & Sons Inc, 1983.

- [82] W. C. Johnson and J. I. D. Alexander. Interfacial conditions for thermomechanical equilibrium in two-phase crystals. *J. Appl. Phys.*, 59:2735–2746, 1986.
- [83] F. I. Fedorow. *Theory of Elastic Waves in Crystals*. Nauka, Moscow, 1965.
- [84] M. A. Slawinski. *Waves and Rays in Elastic Continua*. World Scientific Publishing Company, 2 edition, 2007.
- [85] N. Moelans. A quantitative and thermodynamically consistent phase-field interpolation function for multi-phase systems. *Acta Mater.*, 59(3):1077 – 1086, 2011.
- [86] X. Jin, Z. Wang, Q. Zhou, L. M. Keer, and Q. Wang. On the solution of an elliptical inhomogeneity in plane elasticity by the equivalent inclusion method. *Journal of Elasticity*, 114:1–18, 2014.
- [87] J. Eiken, B. Böttger, and I. Steinbach. Multiphase-field approach for multicomponent alloys with extrapolation scheme for numerical application. *Phys. Rev. E*, 73:066122, Jun 2006.
- [88] J. Hötzer, M. Jainta, P. Steinmetz, B. Nestler, A. Dennstedt, A. Genau, M. Bauer, H. Köstler, and U. Råde. Large scale phase-field simulations of directional ternary eutectic solidification. *Acta Mater.*, 93:194 – 204, 2015.
- [89] G. Caginalp and W. Xie. Phase-field and sharp-interface alloy models. *Phys. Rev. E*, 48:1897, 1993.
- [90] J. D. Eshelby. The elastic field outside an ellipsoidal inclusion. *Proc. Roy. Soc. A: Math. Phys. Eng. Sci.*, 252(1271):561–569, 1959.
- [91] O. Tschukin, D. Schneider, and B. Nestler. An elasto-chemical phase-field model for isotropic solids. submitted to *Eur. J. Mech. A-Solid*.
- [92] F. Wang, O. Tschukin, M. Selzer, and B. Nestler. Breakup of liquid jets due to capillarity. unpublished.